AN ABSTRACT OF THE THESIS OF

Ruiping Wang for the degree of Doctor of Philosophy in Physics presented on May 3, 1991.

Title: Perturbed Angular Correlation Spectroscopy of Defects in Ceria.

Redacted for privacy

Abstract approved: _____.

John A. Gardner

Dilute indium dopants in cerium oxides have been studied by ^{111}In/Cd Perturbed Angular Correlation (PAC) spectroscopy. We control oxygen concentration in the cerium oxides through doping or high-temperature vacuum annealing. We have found four different defect complexes. At low temperatures, evidence is found of interaction with an electronic hole trapped by ^{111}Cd after the radioactive decay of the ^{111}In parent, the "aftereffects" interaction.

In undoped ceria, we found that indium always forms a defect complex with a tightly bound oxygen vacancy (A site). The A site has an axially symmetric electric field gradient (efg) and V_{zz}(lat) is 0.87 (10^{16}Volts/cm^2). The efg symmetry axis can reorient its direction under thermal activation. The activation energy for this reorientation is 0.60(2) eV. When we increase the oxygen vacancy concentration by annealing the ceria sample at high temperatures or doping ceria with more than 0.4% Y, we find another two defect complexes (B and C sites). The B site is the

complex of the A site plus another oxygen vacancy distant from the indium probe and the C site is a complex of the A site plus another oxygen vacancy on the opposite side of the indium atom from the first vacancy. The B site is slightly asymmetric and its V_{zz}(lat) at room temperature is 0.98 (10^{16}Volts/cm^2). The C site is axially symmetric and its V_{zz}(lat) is 3.76 (10^{16}Volts/cm^2). The B and C sites are not observed in as much as 1% In-doped ceria. When we dope ceria with more than 300ppm Nb, the A site is replaced by an unperturbed site and another defect complex (D site). The D site is asymmetric with asymmetry parameter being approximately 0.5 and V_{zz}(lat) being 2.43 (10^{16}Volts/cm^2). The D site disappears between room temperature and 176K. The unperturbed site is affected by the "aftereffects". Even in Nb-doped ceria, we can observe the A, B, C sites by annealing the sample at temperatures 1000℃ or above and we can resume the D site and the unperturbed site by flowing oxygen over the sample above 300℃. This indicates oxygen can diffuse into ceria at temperatures above 300℃.

Perturbed Angular Correlation Spectroscopy of Defects in Ceria

by

Ruiping Wang

A THESIS

submitted to

Oregon State University

in partial fulfillment of
the requirements for the
degree of

Doctor of Philosophy

Completed May 3, 1991

Commencement June 1991

APPROVED:

Redacted for privacy

Professor of Physics in charge of major

Redacted for privacy

Chairman of the Department of Physics

Redacted for privacy

Dean of Graduate School

Date thesis is presented May 3, 1991

Typed by Ruiping Wang for Ruiping Wang

Acknowledgement

Special thanks to my major Professor John A. Gardner, who introduced me to this interesting research field and helped me through all these years of research academically as well as personally. I am grateful to Professor William E. Evenson, who helped me in understanding PAC theory and discussing physics of this work. Thanks to Dr. James A. Sommers, who prepared all the sample solutions and made this work possible and meaningful.

Many thanks to Dr. Han-Tzong Su, who helped me very much in the early stage of this work, and to Dr. Henri J. F. Jansen for his stimulating and helpful discussions.

Special thanks to Mr. Randy Lundquist for making the PAC fitting program so nice and so user-friendly on the IBM PC, and to my friend Ms. Lisa Dundon for her help with English.

I've greatly enjoyed the friendship of all the men and women with whom I've shared research activities: Dr. Shaw-Shya Kao, Mr. Weimin Han, Ms. Lan L. Peng, Mr. Heinz Fuchs, Mr. Georg Weidlich, Mr. Rainer Schwenker.

Last, but not least, special thanks to my father for his unfailing love and encouragement; to my husband Jibing for his understanding and patience through out this work; to my lovely daughter Alicia for bringing me so much joy and happiness.

The financial supports from the Physics Department and U.S. Department of Energy under contract number DE-FG06-85ER45191 are gratefully acknowledged.

Table of Contents

1. Introduction 1

1.1. Cerium oxide 2

1.2. Previous work on the ceria system 4

1.2.1. Phase diagram of ceria 4

1.2.2. Proposed defect mechanism for ceria system 7

1.3. Perturbed angular correlation (PAC) spectroscopy 9

2. Theory of perturbed angular correlations 14

2.1. The generalized directional angular correlation $W(\mathbf{k}_1,\mathbf{k}_2,t)$ 14

2.2. The static electric quadrupole perturbation 22

2.3. The stochastic fluctuating field model 27

3. Experimental arrangements 33

3.1. PAC spectrometer 33

3.2. Spectrometer calibration 42

3.3. Sample preparation 44

3.4. Data reduction 45

4. Experimental results 53

4.1. Preliminary work on ceria 53

4.2. Undoped ceria results 59

4.3. Y-doped and pumped ceria results 66

4.4. Nb-doped ceria results 73

4.5. Other results on ceria 81

5. Analysis of the experimental results 85

5.1. Undoped ceria 86

5.2. Pumped and Y-doped ceria 97

5.3. Nb-doped ceria 108

6. Summary and conclusions 114

References 118

Appendices 122

A. Perturbation function for the I-J coupling interaction 122

B. The on-off model 124

List of Figures

Figure		Page
1.1	Structure diagram of ceria	3
1.2	Phase diagram of ceria	6
1.3	^{111}In /^{111}Cd decay schematic diagram	12
2.1	The schematic diagram of cascade $I_i \rightarrow I \rightarrow I_f$	15
2.2	(a) Eigenvalues and (b) PAC frequencies of the quadruple Hamiltonian for I = 5/2 as functions of asymmetry parameter η	25
2.3	XYZ model: $-G_2(t)$ as a function of time t and fluctuation rate w.	31
2.4	XYZ model: (a) frequencies and (b) damping rates as a function of efg fluctuation rate w.	32
3.1	The functional block diagram of the PAC spectrometer	34
3.2	Gamma rays detected by TSCA	35
3.3	(a) The graphite heating element and (b) sectional view of the PAC furnace	41
3.4	Block diagram view of the PAC data reduction process	49
4.1	Spectra of undoped ceria synthesized in PAC furnace	55
4.2	Room temperature X-ray diffraction pattern of undoped ceria	56
4.3	SEM pictures of undoped ceria synthesized (a) at 1000°C (b) at 1600°C	58
4.4	Spectra of undoped ceria at elevated temperatures	60
4.5	Undoped ceria at 150°C (a) A_2G_2 (b) FFT	62
4.6	Spectra of 0.2%Y-doped ceria at elevated temperatures	67
4.7	Spectra of 0.8%Y-doped ceria at elevated temperatures	68
4.8	Room temperature spectra and FFT of Y-doped ceria ($Ce_{1-x}Y_x$)	70
4.9	Spectra of pumped (1000°C) ceria at elevated temperatures	72

4.10 FFT of ceria (a, b), 900℃ pumped ceria (c, d), 1000℃ pumped ceria (e, f) and 1200℃ pumped ceria (g, h) 74

4.11 Room temperature spectra of Nb-doped ceria ($Ce_{1-y}Nb_y$) 76

4.12 Spectra of Nb-doped ceria ($Ce_{1-y}Nb_y$) at about 200℃ 77

4.13 Spectra of 0.05%Nb-doped ceria at elevated temperatures 78

4.14 Spectra of 0.05%Nb-doped ceria pumped at elevated temperatures 79

4.15 Spectra of undoped(a,b), 1%In-doped (c,d) and 0.8%Y-doped(e,f) ceria 82

4.16 Spectra of 0.05%Ta-doped (a,b) and 0.05%Nb-doped (c,d) ceria 83

4.17 Spectra of undoped (a,b), pumped undoped (c,d) and 500 ppm Nb-doped (e,f) ceria at 77K 84

5.1 χ^2 of the undoped ceria for Fit I, II, and III 89

5.2 χ^2 of the undoped ceria for Fit III 89

5.3 The PAC frequencies of undoped ceria for Fit I, II, and III 90

5.4 The PAC frequencies of undoped ceria for Fit III 90

5.5 The A site fraction of undoped ceria for Fit I, II, and III 91

5.6 The A site fraction of undoped ceria for Fit III 91

5.7 The X site fraction of undoped ceria for Fit I, II, and III 92

5.8 The X site fraction of undoped ceria for Fit III 92

5.9 The A site XYZ lambda of undoped ceria for Fit I, II, and III 93

5.10 The A site XYZ lambda of undoped ceria for Fit III 93

5.11 The A site reorientation rate w of undoped ceria for Fit I, II, and III 94

5.12 The A site reorientation rate w of undoped ceria for Fit III 94

5.13 The X site damping lambda of undoped ceria for Fit I, II, and III 95

5.14 The X site damping lambda of undoped ceria for Fit III 95

5.15 The A site reorientation rate w of undoped ceria for different reorientation ((a) 3, (b) 4, (c) 6) directions 96

5.16 χ^2 of the pumped and Y-doped ceria 99

5.17 χ^2 of the pumped and Y-doped ceria at room temperature with or without line broadening 99

5.18 The frequencies of the B site at elevated temperatures 100

5.19 The frequency ω_1 of the C site at elevated temperatures 100

5.20 The asymmetry parameter η of the B site 102

5.21 The line broadening of the C site at room temperature 102

5.22 The A site fraction of pumped ceria 103

5.23 The A site fraction of Y-doped ceria 103

5.24 The C site fraction of pumped ceria 104

5.25 The C site fraction of Y-doped ceria 104

5.26 The X site fraction of pumped ceria 105

5.27 The X site fraction of Y-doped ceria 105

5.28 The XYZ damping lambda of the B site 106

5.29 The reorientation rate w of the B site for 3 (a), 4 (b), and 6 (c) reorientation directions 107

5.30 χ^2 of the fits for Nb-doped ceria 109

5.31 The frequencies of the D site at elevated temperatures 109

5.32 The asymmetry parameter η of the D site 110

5.33 The fraction of the D site at elevated temperatures 110

5.34 The fraction of the cubic site at elevated temperatures 111

5.35 The fraction of the X site at elevated temperatures 111

5.36 The damping rate λ_a of the "on-off" model for Nb-doped ceria 112

5.37 The "off" rate r of the "on-off" model for Nb-doped ceria 112

5.38 The λ_a and r for Nb-doped ceria at 300°C or below 113

List of Tables

Table		Page
1.1	Summary of relevant nuclear characteristics of ^{111}In to ^{111}Cd transition	11
4.1	Chemical analysis of batch one solution	54
4.2	Comparison of point ion calculation and experimental $V_{zz}(lat)$	64
4.3	Chemical analysis of batch two solution	65
6.1	Summary of the A, B, C, and D sites	117

Perturbed Angular Correlation Spectroscopy of Defects in Ceria

1. Introduction

Ceramics include a wide range of materials. They have been defined by the National Academy of Sciences[1] as "inorganic, nonmetallic, materials processed or consolidated at high temperatures". Advanced or high technology ceramics are distinguished from more traditional ceramics by both the specialized properties they possess and the sophisticated processing they require. Unlike traditional ceramic materials, based primarily on silicates, advanced ceramic materials include oxides, carbides, hydroxides, nitrides, carbonates, and others. They can be electrical insulators, semiconductors, conductors, or even superconductors under certain conditions. These materials possess specialized properties, including high heat, wear, and corrosion resistance, as well as specialized electrical and optical properties, which allow these new ceramics to perform well in a number of high value-added applications.

In recent years, ceramic oxides, such as ZrO_2, ThO_2, and CeO_2 have drawn substantial attention both in applications and basic research. They can be used as solid electrolytes in fuel cells, oxygen sensors etc. Much research has been done on these oxides, especially on the ZrO_2 system because of its important applications.

1.1 Cerium oxide

There are two commonly known valence levels or forms of cerium[2]: trivalent (cerous), as in Ce_2O_3, and tetravalent (ceric), as in CeO_2. In nature, cerium occurs in several rare minerals, mostly salts, such as cerite, a basic merasilicate, or monazite (cerous phosphate). Cerium oxide's share in the earth's crust is estimated to be approximately from 5×10^{-5} to 10^{-3}. The principal commercial source of cerium oxide is monazite. Cerium is the most abundant rare earth metal. In small lots, 99.9% cerium costs about \$2/g.[3]

Although in nature cerium occurs in its trivalent form, cerium dioxide (ceria) (CeO_2) is more stable than cerous oxide (Ce_2O_3), particularly in the presence of free oxygen. The tetravalent ceric oxide is less stable than the oxides of aluminium, zirconium, beryllium, and magnesium. Ceria decomposes at high temperatures relatively easily. The dissociation of ceria occurs to an appreciable degree at 1600°C.

Ceria crystallizes in the cubic system with a fluorite type lattice (Fig. 1.1), whereas cerous oxide crystallizes in the hexagonal system.

CeO_2 has been described in terms of a face-centered-cubic unit cell containing four units of CeO_2. The center of eight O atoms situated at the corners of a surrounding cube which is centered by a cerium atom; and each O atom has about it a tetrahedron of Ce atoms. The lattice constant is 5.411 Å (at 26°C). The symmetry is cubic with the atoms of its four molecules per unit cell in the following positions of O_h^5 ($Fm3m$)[4]:

Ce: (0,0,0); F.C

O: $\pm$(1/4,1/4,1/4); F.C.

Ceria is a heavy substance; its specific weight is 7.3, similar to the other rare earths of the group which crystallize in the cubic form. The melting point of ceria is among the highest of all refractory oxides at 2750℃, surpassing that of beryllia and of zirconia. Cerous oxide melts at 1690℃. The boiling temperature of ceria has not been established, and is

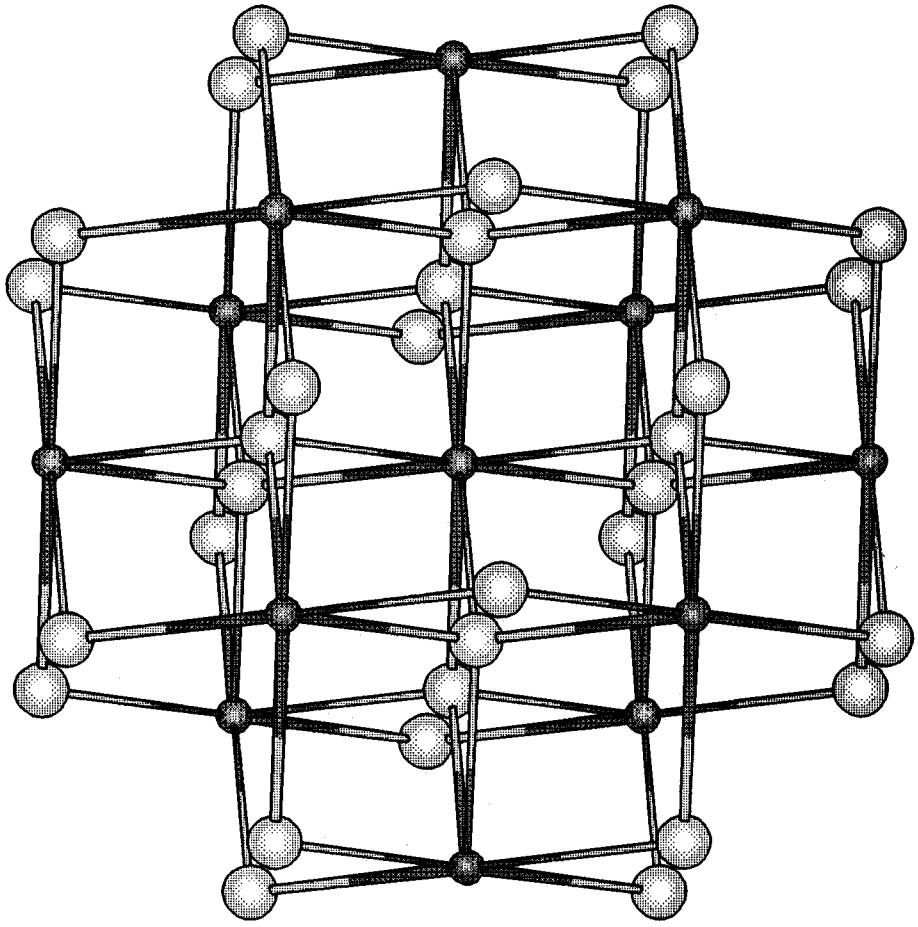

Fig. 1.1 Atomic structure of ceria. The larger atom is oxygen and the smaller one is cerium.

difficult to attain. The coefficient of thermal expansion of sintered ceria in the range 0-800℃ was found to be 8.6×10^{-6}/℃.

The electrical conductivity of ceria is comparatively high. It is strongly dependent on the temperature and on the duration of the prefiring. This "heat treatment" causes a partial dissociation of ceria, and a formation of "anomalous mixed solutions" with oxygen deficiency in the lattice. In general, sintered ceria is a much better conductor of electricity than sintered zirconia and sintered thoria. In a hydrogen atmosphere, still a higher conductivity will result.

There has been increasing interest in the use of cerium dioxide doped with divalent or trivalent cations as a solid electrolyte for application in fuel cells. The high ionic conductivity and low activation energy for ionic conduction makes doped CeO_2 attractive as a solid electrolyte, particularly at temperatures below 800°C[5]. In fuel cell design, operation at lower temperatures allows for flexibility in electrode selection, reduced maintenance costs, and a reduction in the heat-insulating parts needed to maintain the higher temperatures. There is also interest in the automotive industry for developing lower temperature oxygen sensors to control the air-to-fuel ratio in automobile exhausts[6]. The two oxides that are most often used as solid electrolytes, doped ZrO_2 and doped ThO_2, are less suitable at lower temperatures because of low electrical conductivity and electrode polarization.

1.2 Previous work on the ceria system

1.2.1 Phase diagram of ceria

Aside from the intrinsic scientific interest in the phase relationships

of the $CeO_{2-\delta} - O_2$ system there is an immense practical interest due to the many uses to which this material is put in both a pure and a doped state. Few systems have received more attention with respect to their phase relationships and the nature of the defects caused by the loss of oxygen from the parent fluorite, CeO_2.

Bevan[7] and Brauer[8], in the earliest studies, used X-ray diffraction to study the phase relationships of the CeO_2-Ce_2O_3 system. A number of ordered phases were found at low temperatures. Later Brauer measured oxygen dissociation pressure for the temperature range from 600 to 1050°C using a dynamic method with given hydrogen-water vapor mixtures. Phase relationships and heats of formation were deduced from these measurements. Bevan and Kordis[9] determined oxygen pressures in equilibrium with cerium oxides by equilibration with CO / CO_2 or H_2 / H_2O mixtures at temperatures from 636 to 1169°C. Partial and integral free energies, enthalpies and entropies were calculated and used to construct the phase diagram at these temperatures. Ray and Nowick[10] studied intermediate phases by X-ray and neutron diffraction. A number of thermodynamic studies[11,12] and an electron microscopy study[13] have also been used to deduce phase relationships.

Reduced ceria retains its cubic fluorite structure intact over an extended composition range at elevated temperatures above 680°C. At lower temperatures a series of sharply defined intermediate phases whose compositions are given by the general formula R_nO_{2n-2} were found, where n takes on a number of integral values. The observed phases have the following n-values and Greek-letter designations:

n=6(σ), 7(ι), 9(ς), 10(ε), 11(δ), and 12(β).

α phase is fluorite cubic with lattice constant 5.411Å. α' phase is similar to α phase, a fluorite cubic, but with slightly larger lattice constant (~5.44Å). The basic phase diagram is shown in Fig. 1.2. The oxygen-deficient region that we are interested in is very close to stoichiometry (approximately x>1.99).

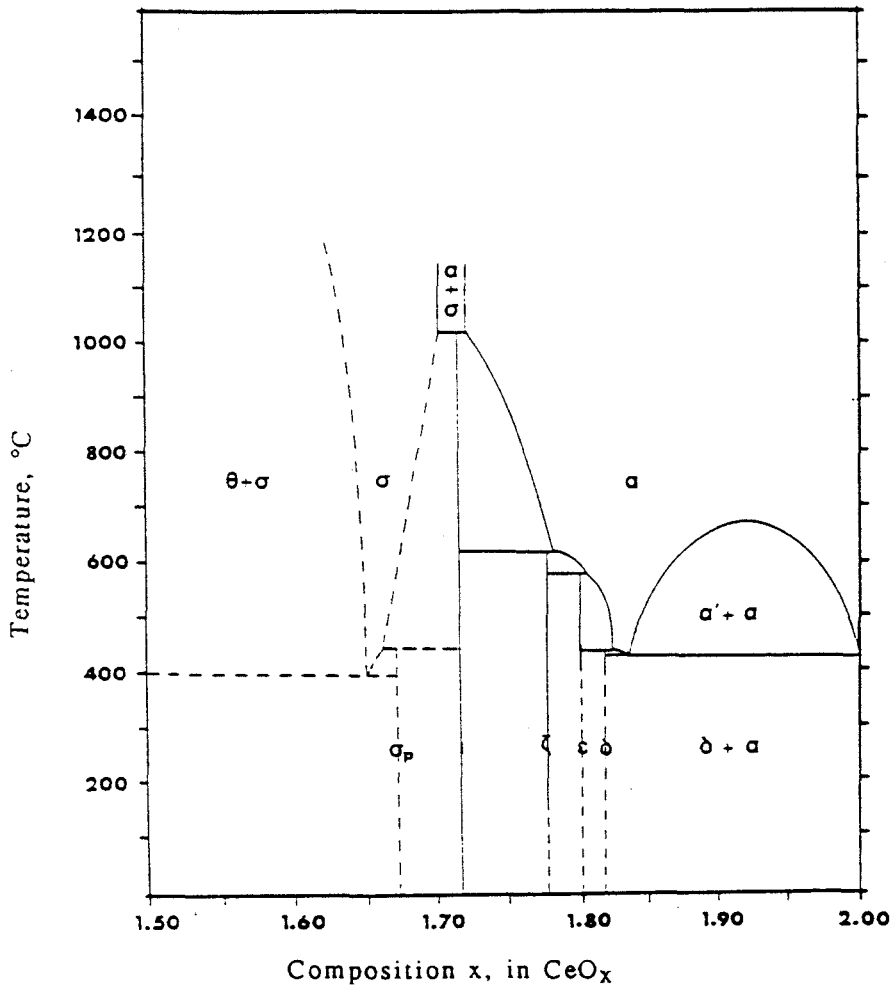

Fig. 1.2 Phase diagram of ceria (CeO_2).

1.2.2 Proposed defect mechanism for ceria system

The fact that the fluorite structure remains intact, even after the incorporation of up to the order of 14% oxygen vacancies, presents a unique opportunity to study the defect properties of this solid for small as well as large concentrations of defects. Stoichiometric CeO_2 is stable in air, and no thermodynamically stable higher oxide exists at higher oxygen pressure. Thus one has an extended range of experimental conditions for which defect concentrations remain small and for which one may properly apply the idealized defect theory of Schottky and Wagner. In addition, the existence of a large single phase region at elevated temperatures offers the opportunity to observe, at a given temperature, the transition from ideal defect behavior to the region characterized by defect interactions.

Although nonstoichiometric CeO_2 appears to be ideally suited for defect structure determinations by electrical and thermodynamic means, no defect model consistent with all the available evidence has been established. Oxygen deficiency can be caused by disorder either on the cation sublattice (i.e., by cerium interstitials) or on the anion sublattice (i.e., by oxygen vacancies). A number of investigators have studied the oxygen partial pressure dependence exhibited by the electrical conductivity for pressed powder samples of ceria.

From the mass-action law, one can find that the electrical conductivity σ depends on the oxygen partial pressure p such that,

$$\sigma = C_1(T)p^{-1/n}.$$

Here, n=4 if all oxygen vacancies are singly ionized, and n=6 if all oxygen vacancies are doubly ionized. Rudolph[14] observed a $p_{O_2}^{-1/5.7}$

dependence at 970°C and concluded that ceria was an n-type semiconductor due to its increasing conductivity with decreasing P_{O_2}. Greener et al.[15] obtained approximately a $P_{O_2}^{-1/5}$ dependence for σ over the P_{O_2} range 0.006-1.0 atm above 1100°C and suggested that the defects were therefore either quadruply ionized cerium interstitials or fully ionized oxygen vacancy pairs. Blumenthal and Laubach[16] measured the electrical conductivity from 800°C to 1500°C over an extended range of P_{O_2} and showed that their results were consistent with a vacancy model exhibiting multiple states of ionization. In another paper, Blumenthal et al.[17] concluded instead that a defect model based on cerium interstitials in multiple states of ionization was a more appropriate description, based on the results of somewhat more extensive measurements. Later Blumenthal et al.[18,19,20] claimed their data were consistent with a defect model involving doubly ionized oxygen vacancies arising from both impurities and nonstoichiometry. Tuller and Nowick[21] studied electrical properties of reduced ceria, CeO_{2-x}, single crystals and proposed hopping conduction and the small polaron mechanism. Gerhardt-Anderson and Nowick[22] studied the dopant ionic radius dependence of the conductivity for M_2O_3-doped ceria, where M represents trivalent rare earth ions.

Other types of measurements which depend more directly on the type of ionic defect present in CeO_{2-x} point invariably to an oxygen-vacancy model. Steele and Floyd[23] measured the self-diffusion of oxygen in both ceria and ceria-yttria solutions and concluded that oxygen vacancies were clearly the predominant defect. Ban and Nowick[24] found no significant difference in the relative changes of the macroscopic length and the lattice parameter of a single crystal of ceria upon reduction, a

result consistent only with a vacancy model.

1.3 Perturbed angular correlation (PAC) spectroscopy

An excited nucleus can decay to its ground state by emitting γ-rays or other energy quanta. If we consider two successively emitted γ-rays, the angle between these two γ-rays has a certain angular correlation. When an excited nucleus is subjected to an external electric or magnetic field, this field will interact with the nuclear spin and quadrupole moment of this nucleus and change the angular correlation of the emitted γ-rays. This is called perturbed angular correlation. By studying the perturbed angular correlation and its dependence on different conditions, e.g. temperature or pressure, one can derive information about the nuclear environment, type of interaction, crystal symmetry, etc., and one can further deduce the physical properties of solid state materials.

The PAC technique used here is time differential perturbed angular correlation (TDPAC). This is used in the case where the half-life of the intermediate state of the γ–γ cascade is much longer than the time resolution of the PAC spectrometer. For example, we used ^{111}Cd as the nuclear probe, whose intermediate state half-life is 85ns, and the time resolution of our PAC spectrometer is about 2ns. Therefore this choice of nuclear probe enables us to use TDPAC to study the perturbed angular correlation during the lifetime of the intermediate state of the probe nucleus.

The PAC technique is a local probe. The γ–γ perturbed angular correlation spectroscopy has been used to study defect-impurity

association in metals[25,26,27,28], internal oxidation in metals[29], impurity effects in semiconductors[30], phase identification in compounds[31,32], etc.

PAC measurements have been done by our research group and others on the zirconia (ZrO_2) system[33,34], a material of great practical importance. The microscopic properties of phase transitions and defect dynamics have been studied. Pure zirconia exhibits three well-defined polymorphs: the monoclinic, tetragonal, and cubic phases. To obtain the simple cubic phase, one has either to raise the temperature to above 2370℃, which is impossible in this lab, or dope at least 17 mole% of trivalent elements, e.g. Y. When one dopes this much Y to stablize the structure, the resulted crystal is then complicated by the large number of Y impurities. The defect mechanism thus become very complicated. So it is very important for us to understand a "pure" cubic fluorite structured oxide in order to study the more complicated system. We found an ideal system for this purpose, ceria (CeO_2).

Aside from its practical applications, ceria is a very good system for fundamental as well as defect studies. It has the simple fluorite cubic structure, and it keeps this single phase for a wide temperature and stoichiometry range (Fig. 1.2).

To study the properties of solid state materials by the PAC technique, the probe nuclei are introduced in very dilute solution into the material of interest (concentration of order 10^{-9}). The nuclear probe that we used in this study is ^{111}Cd, which decays from ^{111}In.

The 2.83 days half-life ^{111}In decays by electron-capture to an excited state of its daughter isotope ^{111}Cd, which subsequently decays to its ground state by emitting two γ-rays with energies of 171 and 245 keV.

The relevant nuclear characteristics of the electron-capture decay of ^{111}In to ^{111}Cd are summarized in Table 1.1, and Fig. 1.3 gives the decay scheme of the ^{111}In to ^{111}Cd transition.

Table 1.1 Summary[35] of relevant nuclear characteristics of ^{111}In to ^{111}Cd transition

Parent half-life(^{111}In)	2.83d
Energies of cascade γ-rays	
γ_1	171.28(8)keV
γ_2	245.42(7)keV
Nuclear-spin sequence	$7/2^+ \rightarrow 5/2^+ \rightarrow 1/2^+$
Angular-correlation coefficients	
A_2	-0.180(2)
A_4	≈ 0
Intermediate nuclear state:	
Half-life	85.0(7)ns
Electric quadruple moment[36]	+0.83(13)barn
Magnetic dipole moment	$-0.7656(25)\mu_N$

One of the challenging aspects of PAC spectroscopy is the so-called aftereffects (AE). By aftereffects one usually designates all the electronic rearrangement processes which follow a nuclear decay. After the electron-capture process, the electronic hole in the K-shell of ^{111}Cd decays through x-ray emission and Auger processes. The Auger processes result in a highly ionized probe atom. The recovery time of these excited ionic states

ionic states critically depends on the availability of free electrons in the surrounding environment of the probe atom. The recovery time is less than 10^{-12} sec for probes embedded in metals, which is too short to give any detectable effect[37]. But in semiconductors and insulators, the electronic holes in the outermost shell could persist long enough to introduce an additional perturbation on the angular correlation spectrum. A semiquantitative description of the case where the strength of the perturbation due to aftereffects is much stronger than that of the surrounding lattice has been used to interpret spectra[38,39]. But when the perturbations are comparable, the angular correlation pattern becomes very complicated and has no satisfactory theory to describe it.

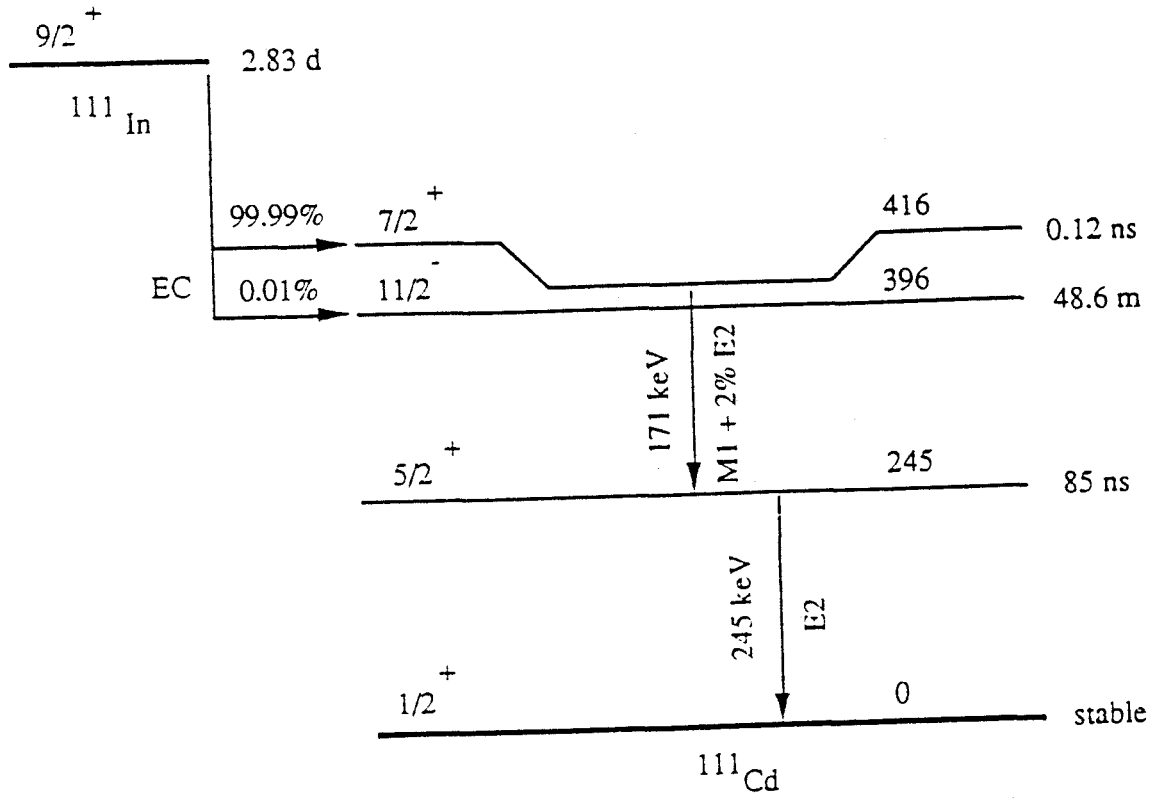

Fig. 1.3 ^{111}In /^{111}Cd decay schematic diagram.[40]

Among several commonly used hyperfine techniques (Mössbauer Spectroscopy, NMR, ESR etc.), PAC spectroscopy has unique advantages. It gives the same signal efficiency for all temperatures. The radioactivity of the sample usually is just a few μCi. One can use this technique to study both static and dynamic hyperfine interactions. But one needs to be aware that when embedding nuclear tracers in the material, the tracer itself could become an impurity center. In this case, what the tracer "sees" is not just the material of interest, but the system of both the material and the tracer. This would be a problem in a study of "perfect" lattice structure. It becomes an opportunity in a study of the local environment of this impurity center. One must always keep this possible tracer-material interaction in mind when one refers to this technique.

2. Theory of perturbed angular correlations

Here we only discuss the hyperfine interaction caused by electric quadrupole interactions since CeO_2 is a nonmagnetic material. The formalism for static electric quadrupole interactions closely follows that given by Frauenfelder and Steffen.[37]

2.1. The generalized directional angular correlation $W(\mathbf{k}_1,\mathbf{k}_2,t)$

The probability of emission of a particle or quantum by a radioactive nucleus depends in general on the angle between the nuclear spin axis and the direction of emission. If the nuclei decay through successive emission of two radiations R_1 and R_2, then the observation of R_1 in a fixed direction $\mathbf{k}_1$ selects an ensemble of nuclei that has a nonisotropic distribution of spin orientations. The succeeding radiation R_2 then shows a definite angular correlation with respect to the first radiation R_1.

$W(\mathbf{k}_1,\mathbf{k}_2,t)\,d\Omega_1 d\Omega_2$ is defined as the probability of a nuclear decay through the cascade $I_i \rightarrow I \rightarrow I_f$ by emitting two successive radiations R_1 and R_2 in the directions $\mathbf{k}_1$ and $\mathbf{k}_2$ into the solid angles $d\Omega_1$ and $d\Omega_2$. $W(\mathbf{k}_1,\mathbf{k}_2,t)$ is the directional angular correlation function for the case in which no polarization is observed. The "t" in the perturbed angular correlation function is the time separation of these two successive radiations.

Using Dirac's notation, a density operator $\hat{\rho}$ is defined as

$$\hat{\rho}=\sum_m |m\rangle g_m \langle m|, \qquad (2\text{-}1)$$

where g_m is the weight of state $|m>$. The probability of finding an ensemble in the state $|n>$ is $p(n)=<n|\hat{\rho}|n>$. Now consider the cascade $I_i \rightarrow I \rightarrow I_f$ by two successive transitions in the direction of $\mathbf{k}_1$ and $\mathbf{k}_2$ into the solid angles $d\Omega_1$ and $d\Omega_2$. Assume the time separation of these two successive transitions is t.

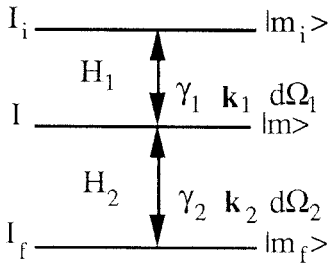

Fig. 2.1 The schematic diagram of cascade $I_i \rightarrow I \rightarrow I_f$.

Before the first transition, the density operator is $\hat{\rho}=\sum_{m_i'} |m_i'>g_{m_i'}<m_i'|$. Assume that $2I_i+1$ states $|m_i'>$ exist and that all have equal weight and are equally populated (magnetic sublevels at elevated temperatures). The states $|m_i'>$ then can be selected such that the density matrix is diagonal:

$$<m_i''|\hat{\rho}|m_i>=(2I_i+1)^{-1}\delta_{m_i''m_i}. \qquad (2\text{-}2)$$

After the first transition induced by H_1, the state of the system changes from $|m_i'>$ to $H_1|m_i'>$ in first-order pertubation theory. Now the density operator is

$$\hat{\rho}(\mathbf{k}_1,0)=\sum_{m_i'} H_1|m_i'\rangle g_{m_i'}\langle m_i'|H_1^+ \qquad (2\text{-}3)$$

and the density operator can be further arranged to

$$\hat{\rho}(\mathbf{k}_1,0)=\sum_{m_i' m_i'' m_i} H_1|m_i''\rangle\langle m_i''|m_i'\rangle g_{m_i'}\langle m_i'|m_i\rangle\langle m_i|H_1^+$$

$$=\sum_{m_i'' m_i} H_1|m_i\rangle(2I_i+1)^{-1}\delta_{m_i'' m_i}\langle m_i|H_1^+$$

$$=\sum_{m_i} H_1|m_i\rangle\langle m_i|H_1^+ \qquad (2\text{-}4)$$

The eigenstate of the intermediate state immediately after the first transition is $|m_a\rangle$. During the lifetime t of the intermediate state, the system may be perturbed by an extranuclear field. This perturbation, which we describe in the state I with the Hamiltonian K, is assumed to act from the time the first radiation is emitted (t=0) until the time t at which the second radiation is emitted. During this time interval the state $|m_a\rangle$ change to a different state $|m_b\rangle$ under the influence of the extranuclear perturbation. This change can be represented by unitary operator $\Lambda(t)$ that describes the evolution of the state vectors $|m_b\rangle$. The state vector can be expressed as

$$\Lambda(t)|m_a\rangle=\sum_{m_b}|m_b\rangle\langle m_b|\Lambda(t)|m_a\rangle. \qquad (2\text{-}5)$$

The time-evolution operator $\Lambda(t)$ satisfies the Schrödinger equation

$$\frac{\partial}{\partial t}\Lambda(t) = -\frac{i}{\hbar}K\Lambda(t). \qquad (2\text{-}6)$$

If K does not depend on the time t during the lifetime of the intermediate state (static perturbation), then the solution of this equation is simply

$$\Lambda(t)=\exp(-\frac{i}{\hbar}Kt). \qquad (2\text{-}7)$$

For a time-dependent perturbation, the solution can be written symbolically as

$$\Lambda(t)=T\exp(-\frac{i}{\hbar}\int_0^t K(t')dt'), \qquad (2\text{-}8)$$

where T is the Feymman time-ordering operator, and the integral must be evaluated according to Feynman's rules for ordered operators.

The density operator $\hat{\rho}(\mathbf{k}_1,0)$ after time t can be expressed as

$$\hat{\rho}(\mathbf{k}_1,t)=\Lambda(t)\hat{\rho}(\mathbf{k}_1,0)\Lambda^+(t)=\sum_{m_i}\Lambda(t)H_1|m_i><m_i|H_1^+\Lambda^+(t). \qquad (2\text{-}9)$$

From the definition of the density operator, we could also express the density operator $\hat{\rho}(\mathbf{k}_1,t)$ as

$$\hat{\rho}(\mathbf{k}_1,t)=\sum_m |m>g_m<m|. \qquad (2\text{-}10)$$

After the second transition, induced by H_2, the state of the system changes from $|m>$ to $|m_f>=H_2|m>$. Now the density operator is

$$\hat{\rho}(\mathbf{k}_1,t,\mathbf{k}_2,0)=\sum_m H_2|m>g_m<m|H_2^+. \qquad (2\text{-}11)$$

$$\text{So,}\quad \hat{\rho}(\mathbf{k}_1,t,\mathbf{k}_2,0)=\sum_m H_2\hat{\rho}(\mathbf{k}_1,t)H_2^+. \qquad (2\text{-}12)$$

Inserting (2-9) we obtain

$$\hat{\rho}(\mathbf{k}_1,t,\mathbf{k}_2,0)=\sum_{m_i} H_2\Lambda(t)H_1|m_i><m_i|H_1^+\Lambda^+(t)H_2^+. \qquad (2\text{-}13)$$

Then the probability of emission of successive radiations R_1 and R_2 in directions $\mathbf{k}_1$ and $\mathbf{k}_2$ is the sum over final states $|m_f>$.

$$W(\mathbf{k}_1,\mathbf{k}_2,t)=\sum_{m_f}<m_f|\hat{\rho}(\mathbf{k}_1,t,\mathbf{k}_2,0)|m_f>$$

$$=\sum_{m_f}\sum_{m_i}<m_f|H_2\Lambda H_1|m_i><m_i|H_1^+\Lambda^+H_2^+|m_f>$$

$$=\sum_{m_f}\sum_{m_i}\sum_{m_a}\sum_{m_{a'}}\sum_{m_b}\sum_{m_{b'}}<m_f|H_2|m_b><m_b|\Lambda|m_a><m_a|H_1|m_i>$$

$$\times<m_i|H_1^+|m_{a'}><m_{a'}|\Lambda^+|m_{b'}><m_{b'}|H_2^+|m_f>. \qquad (2\text{-}14)$$

Here $m_{a'}$ and m_a are the eigenstates of the system immediately after the first radiation, $m_{b'}$ and m_b are the eigenstates of the system right before the second radiation, m_i is the initial state of the system, and m_f is the final state of the system.

From (2-9)

$$<m_b|\hat{\rho}(\mathbf{k}_1,t)|m_{b'}>=\sum_{m_i}\sum_{m_a}\sum_{m_{a'}}<m_b|\Lambda(t)|m_a><m_a|H_1|m_i><m_i|H_1^+|m_{a'}><m_{a'}|\Lambda^+(t)|m_{b'}>,$$

(2-15)

and if we define

$$<m_{b'}|\hat{\rho}(\mathbf{k}_2,0)|m_b>=\sum_{m_f}<m_f|H_2|m_b><m_{b'}|H_2^+|m_f>, \qquad (2\text{-}16)$$

then

$$W(\mathbf{k}_1,\mathbf{k}_2,t)=\mathrm{Tr}\{\hat{\rho}(\mathbf{k}_1,t)\hat{\rho}(\mathbf{k}_2,0)\}. \qquad (2\text{-}17)$$

If we only consider the directional correlation, which is the case throughout this work, after some lengthy calculations the directional correlation function become

$$W(\mathbf{k}_1,\mathbf{k}_2,t)=\sum_{k_1k_2}\sum_{N_1N_2}[(2k_1+1)(2k_2+1)]^{-\frac{1}{2}}A_{k_1}(1)A_{k_2}(2)G_{k_1k_2}^{N_1N_2}(t)$$

$$\times Y^{*}_{k_1N_1}(\theta_1,\varphi_1)Y_{k_2N_2}(\theta_2,\varphi_2), \qquad (2\text{-}18)$$

where $A_{k_1}(1)$ and $A_{k_2}(2)$ are numbers which depend only on the spins of the nuclear states involved in the transition and the multipolarities of the emitted radiations. $Y^{*}_{k_1N_1}(\theta_1,\varphi_1)$ and $Y_{k_2N_2}(\theta_2,\varphi_2)$ are the spherical harmonics, and the constant factor 4π has been dropped since it is irrelevant to the angular correlation. The summation indices k_1 and k_2 are not related to the vectors $\mathbf{k}_1$ and $\mathbf{k}_2$. We have defined a perturbation factor or function as:

$$G_{k_1k_2}^{N_1N_2}(t)=\sum_{m_am_{a'}}\sum_{m_bm_{b'}}(-1)^{2I+m_a+m_b}[(2k_1+1)(2k_2+1)]^{\frac{1}{2}}\begin{pmatrix} I & I & k_1 \\ m_{a'} & -m_a & N_1 \end{pmatrix}$$

$$\times\begin{pmatrix} I & I & k_2 \\ m_{b'} & -m_b & N_2 \end{pmatrix}\langle m_b|\Lambda(t)|m_a\rangle\langle m_{a'}|\Lambda^{+}(t)|m_{b'}\rangle, \qquad (2\text{-}19)$$

where $\begin{pmatrix} I & I & k_1 \\ m_{a'} & -m_a & N_1 \end{pmatrix}$ and $\begin{pmatrix} I & I & k_2 \\ m_{b'} & -m_b & N_2 \end{pmatrix}$ are the Wigner 3-j symbols.

This perturbation factor contains all the information about the interaction between the probe nucleus and the extranuclear perturbations. It is this factor from which we derive the physical properties of solids.

As shown above, in the case of static perturbations

$$\Lambda(t)=\exp(-\frac{i}{\hbar}Kt). \qquad (2\text{-}20)$$

For practical reasons the angular correlation experiments usually are carried out on nuclei in polycrystalline samples, which is also the case for this study. We assume a polycrystalline sample consists of a large number of randomly oriented microcrystals. Let $D(\Omega)$ be the rotation matrix that transforms the interaction Hamiltonian $K(z)$ from the lab coordinate frame z through a set of prescribed Euler angles $\Omega=(\phi,\theta,\gamma)$ to the principal axes system z' of a microcrystal. The observed angular correlation is obtained by averaging over the random directions of the symmetry axes of the microcrystals. Let U be the unitary operator that diagonalizes $K(z')$. Then

$$UD(\Omega)\Lambda(t)D^{-1}(\Omega)U^{-1}=e^{-\frac{iEt}{\hbar}}, \tag{2-21}$$

where E is a diagonal operator whose diagonal elements are the eigenvalues of K. Then the time evolution operator becomes

$$\Lambda(t)=D^{-1}(\Omega)U^{-1}e^{-\frac{iEt}{\hbar}}UD(\Omega), \tag{2-22}$$

and the matrix elements of $\Lambda(t)$ can be rewritten as

$$\langle m_b|\Lambda(t)|m_a\rangle=\sum_{m_1m_2n}\langle n|m_1\rangle^{*}\langle n|m_2\rangle\exp(-\frac{iE_nt}{\hbar})D^{I}_{m_1m_b}{}^{*}(\Omega)D^{I}_{m_2m_a}(\Omega), \tag{2-23}$$

where m_1 and m_2 are the basis in principal axes system z'.

Inserting this expression into (2-19), after certain simplifications and averaging the angular correlation function over orientations Ω of the rotation matrix, i.e. averaging over all possible microcrystal orientations of a random polycrystalline sample, we get

$$W(\theta,t)=\sum_{k=0,even}^{k_{max}}A_{kk}G_{kk}(t)P_k(\cos\theta) \tag{2-24}$$

Here θ is the angle between the two cascade radiations and $P_k(\cos\theta)$ are the Legendre polynomials. For the ^{111}Cd probe, $k_{max}=4$, and

$$G_{kk}(t)=\overline{G_{k_1k_2}^{N_1N_2}(t)}^{\Omega} = \sum_{\substack{m_1m_2\\ m_1'm_2'}} \sum_{nn'} (-1)^{2I+m_1+m_2} \begin{pmatrix} I & I & k \\ m_1' & -m_1 & p \end{pmatrix} \begin{pmatrix} I & I & k \\ m_2' & -m_2 & p \end{pmatrix}$$

$$\times e^{-i\frac{(E_n-E_{n'})t}{\hbar}} \langle n|m_1\rangle^* \langle n'|m_1'\rangle \langle n|m_2\rangle \langle n'|m_2'\rangle^*, \quad (2\text{-}25).$$

where the summation indices n and n' go over the eigenstates of the interaction Hamiltonian K. Further, this function can be written in the form

$$G_{kk}(t)=\sum_n S_{nn}^{kk} + \sum_{n\neq n'} S_{nn'}^{kk} \cos\left(\frac{(E_n-E_{n'})t}{\hbar}\right). \quad (2\text{-}26)$$

The coefficients S are defined as

$$S_{nn'}^{kk} = \sum_{\substack{m_1m_2\\ m_1'm_2'}} (-1)^{2I+m_1+m_2} \begin{pmatrix} I & I & k \\ m_1' & -m_1 & p \end{pmatrix} \begin{pmatrix} I & I & k \\ m_2' & -m_2 & p \end{pmatrix} \langle n|m_1\rangle^* \langle n'|m_1'\rangle \langle n|m_2\rangle \langle n'|m_2'\rangle^*$$

(2-27)

An important feature of the perturbation function (2-26) for the polycrystalline sample is the time-independent term $\sum_n S_{nn}^{kk}$. Because of this term, the angular correlation of a polycrystalline sample is never completely destroyed under the influence of static perturbing fields. For this reason, this term has historically been called the "hard-core".

When there is no extranuclear interaction, in which case $G_{kk}(t)=1$, then

$$W(\theta,t)=W(\theta)=\sum_{k=0,even}^{k_{max}} A_{kk}P_k(\cos\theta) \quad (2\text{-}28)$$

This is the directional angular correlation for free nuclei.

2.2 The static electric quadrupole perturbation

The Hamiltonian for the static electric quadrupole interaction of a nucleus with its environment is

$$H_{QI}=\frac{4\pi}{5}\sum_{\mu=-2}^{2}(-1)^{\mu}q_{\mu}^{(2)}V_{-\mu}^{(2)} \quad (2\text{-}29)$$

where $q_{\mu}^{(2)}, V_{-\mu}^{(2)}$ are the second rank tensor operators of the nuclear moment and the field (classical electric field gradient, efg), respectively. In principal axes

$$V_0^{(2)}=\sqrt{\frac{5}{16\pi}}V_{zz} \quad (2\text{-}30)$$

$$V_{\pm1}^{(2)}=0 \quad (2\text{-}31)$$

$$V_{\pm2}^{(2)}=\sqrt{\frac{5}{96\pi}}\eta V_{zz}. \quad (2\text{-}32)$$

The asymmetry parameter η is defined as

$$\eta=\frac{V_{xx}-V_{yy}}{V_{zz}}. \quad (2\text{-}33)$$

Conventionally, the principal axis system is chosen such that $|V_{xx}|\le|V_{yy}|\le|V_{zz}|$. Therefore, this restricts η to $0\le\eta\le1$, because the Poisson

equation reduces to Laplace's equation, $V_{xx}+V_{yy}+V_{zz}=0$, for external charges. Thus the efg tensor can be sufficiently characterized by the magnitude of its largest component, V_{zz}, and the asymmetry parameter, η.

In the principal axis system, only the diagonal and second off-diagonal terms of the quadrupole Hamiltonian matrix are not equal to zero. Expressing the efg components in Cartesian derivatives, the non-vanishing matrix elements of the quadrupole Hamiltonian are

$$\langle Im\pm2|H_{QI}|Im\rangle=\hbar\omega_Q\frac{\eta}{2}[(I\pm m+1)(I\pm m+1)(I\mp m+1)(I\mp m)]^{\frac{1}{2}}, \qquad (2\text{-}34)$$

$$\langle Im|H_{QI}|Im\rangle=\hbar\omega_Q[3m^2-I(I+1)], \qquad (2\text{-}35)$$

where the quadrupole frequency, ω_Q, is defined as:

$$\omega_Q=\frac{eQV_{zz}}{4I(2I-1)\hbar}. \qquad (2\text{-}36)$$

We use ^{111}Cd (I=5/2) as the nuclear probe throughout this work. The Hamiltonian matrix then becomes

$$H_{QI}=\hbar\omega_Q\begin{pmatrix} 10 & 0 & \eta\sqrt{10} & 0 & 0 & 0 \\ 0 & -2 & 0 & 3\eta\sqrt{2} & 0 & 0 \\ \eta\sqrt{10} & 0 & -8 & 0 & 3\eta\sqrt{2} & 0 \\ 0 & 3\eta\sqrt{2} & 0 & -8 & 0 & \eta\sqrt{10} \\ 0 & 0 & 3\eta\sqrt{2} & 0 & -2 & 0 \\ 0 & 0 & 0 & \eta\sqrt{10} & 0 & 10 \end{pmatrix}. \qquad (2\text{-}37)$$

The secular equation of the quadrupole Hamiltonian has the form

$$E^3+28E(\eta^2+3)-160(1-\eta^2)=0. \qquad (2\text{-}38)$$

The eigenvalues of this Hamiltonian are

$$E_{\pm\frac{5}{2}}=2\alpha\hbar\omega_Q\cos(\tfrac{1}{3}\cos^{-1}\beta) \quad , \tag{2-39}$$

$$E_{\pm\frac{3}{2}}=-2\alpha\hbar\omega_Q\cos(\tfrac{1}{3}(\pi+\cos^{-1}\beta)) \quad , \tag{2-40}$$

$$E_{\pm\frac{1}{2}}=-2\alpha\hbar\omega_Q\cos(\tfrac{1}{3}(\pi-\cos^{-1}\beta)) \quad , \tag{2-41}$$

where

$$\alpha=\sqrt{\frac{28}{3}(\eta^2+3)} \quad \text{and} \quad \beta=\frac{80(1-\eta^2)}{\alpha^3} \quad . \tag{2-42}$$

We define PAC frequencies as

$$\omega_1=|E_{3/2}-E_{1/2}|/\hbar=2\sqrt{3}\alpha\omega_Q\sin(\tfrac{1}{3}\cos^{-1}\beta) \quad , \tag{2-43}$$

$$\omega_2=|E_{5/2}-E_{3/2}|/\hbar=2\sqrt{3}\alpha\omega_Q\sin(\tfrac{1}{3}(\pi-\cos^{-1}\beta)) \quad , \tag{2-44}$$

$$\omega_3=|E_{5/2}-E_{1/2}|/\hbar=2\sqrt{3}\alpha\omega_Q\sin(\tfrac{1}{3}(\pi+\cos^{-1}\beta)) \quad , \tag{2-45}$$

with the sum rule $\omega_3=\omega_1+\omega_2$. Graphs of the eigenvalues of H_{QI} and PAC frequencies of the electric quadrupole interaction as a function of η for I=5/2 are given in Fig. 2.2.

The perturbation factor for polycrystalline samples becomes

$$G_{kk}(t)=S_{k0}+\sum_{n=1}^{3}S_{kn}\cos(\omega_n(\eta)t) \quad , \tag{2-46}$$

where the coefficient S_{kn} is defined as

$$S_{kn}=\sum_{mm'}S_{mm'}^{kk} \quad , \tag{2-47}$$

here introducing a new index $n=|m^2-m'^2|/2$ (for half-integer I) or $n=|m^2-m'^2|$ (for integer I), with $S_{mm'}^{kk}$ given by (2-27).

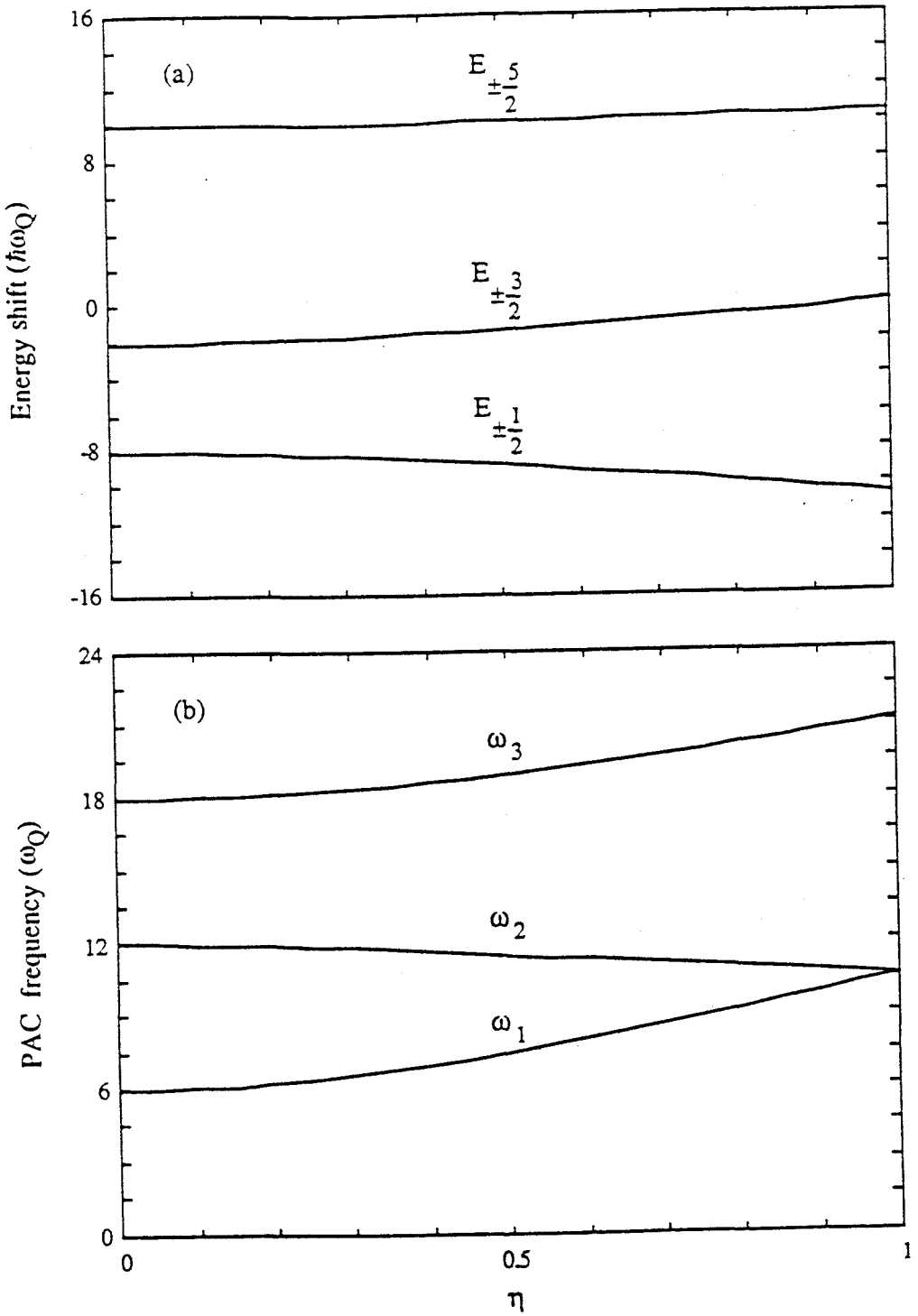

Fig.2.2 (a) Eigenvalues and (b) PAC frequencies of the quadruple Hamiltonian for I = 5/2 as functions of asymmetry parameter η.

Using ^{111}Cd as the nuclear probe, I=5/2 and $A_{44} < 1\% A_{22}$, so the angular correlation function becomes

$$W(\theta,t) \approx 1 + A_{22} G_{22}(t) P_2(\cos\theta), \tag{2-48}$$

$$G_{22}(t) = S_{20} + \sum_{n=1}^{3} S_{2n} \cos(\omega_n(\eta) t), \tag{2-49}$$

$$S_{20} = \frac{1}{2} \sum_{m=1/2}^{5/2} S(m,m), \tag{2-50}$$

$$S_{21} = S(1/2,3/2), \tag{2-51}$$

$$S_{22} = S(3/2,5/2), \tag{2-52}$$

$$S_{23} = S(1/2,5/2), \tag{2-53}$$

with[41]

$$S(m,m') = \frac{1}{35} a_m^2 a_{m'}^2 \left[\frac{1}{3} (5 b_m b_{m'} - c_m c_{m'} - 4)^2 + (b_m c_{m'} - b_{m'} c_m)^2 \right.$$

$$\left. + 4(c_m - c_{m'})^2 + (\sqrt{5} b_m + 3 c_{m'})^2 + (\sqrt{5} b_{m'} + 3 c_m)^2 \right], \tag{2-54}$$

where

$$a_m = (1 + b_m^2 + c_m^2)^{-1/2}, \tag{2-55}$$

$$b_m = \sqrt{10}\eta / \left(\frac{E_m}{\hbar\omega_Q} - 10 \right), \tag{2-56}$$

$$c_m = \sqrt{18}\eta / \left(\frac{E_m}{\hbar\omega_Q} + 2 \right), \tag{2-57}$$

Here E_m are the eigenvalues of the interaction Hamiltonian K. In our fitting program, we used the following expression for the S_{2n}:

$$S_{21} = 0.270096 + \omega_2/\omega_1 \times (-0.00229553 + 0.0264964 \times \omega_2/\omega_1), \tag{2-58}$$

$$S_{22} = 0.347921 + \omega_2/\omega_1 \times (-0.077535 + 0.0233209 \times \omega_2/\omega_1), \tag{2-59}$$

$$S_{23} = 0.149965 + \omega_2/\omega_1 \times (-0.009585 + 0.00659264 \times \omega_2/\omega_1), \tag{2-60}$$

$$S_{20} = 1 - S_{21} - S_{22} - S_{23}, \tag{2-61}$$

These values are found from polynomial approximation to the exact expressions given by (2-50 to 2-57).

2.3 The stochastic fluctuating field model

If the interaction Hamiltonian K depends on the time elapsed between the two successive radiations, the perturbation is time-dependent. There have been several attempts to deal with time-dependent interactions in perturbed angular correlations[42,43].

Abragam and Pound[44] calculated the perturbation function $G_{kk}(t)$ for the time-dependent interaction due to random Brownian motion of ions in liquids under the assumption that the fluctuation rate of the efg, $1/\tau_c$, is much faster than the transition rate , $<\omega_Q^2>^{+1/2}$, between the sublevels of the intermediate state I. This assumption is reasonable for nonviscous liquids such as water or dilute aqueous solutions, because in this case, $\tau_c \approx 10^{-11}$s, which is considerably shorter than the lifetime of the intermediate state of typical PAC probes (for ^{111}Cd $\tau \approx 8\times10^{-8}$s). They finally give a very simple form of the perturbation function, $G_{kk}(t) = e^{-\lambda_k t}$.

The problem of finding an analytical expression for the angular perturbation function $G_{kk}(t)$ for solids with time-dependent electric field gradients is rather complicated. Blume[45] proposed a stochastic theory of PAC which was developed by Winkler and Gerdau[46] for model calculations. This stochastic fluctuating field model considers a system which is subject to an interaction jumping at random in time between a

finite number of possible efg states. Then $H(t)=\sum_j f_j(t)K_j$, where K_j is the Hamiltonian of the jth static efg state, and $f_j(t)$ is defined in such a way that at a given moment τ only one of them -- e.g. $f_a(\tau)$ -- has the value 1, whereas $f_{j\neq a}(\tau)=0$.

For the investigation of this problem it is convenient and customary to introduce the Liouville formalism, expressing the problem in terms of superoperators[47]. If $\hat{\rho}(\mathbf{k}_1,0)$ is the density operator which describes the nuclear system immediately after the emission of the first radiation in the direction $\mathbf{k}_1$, one can describe the time-evolution of the system by a super-operator $\hat{\Omega}(t)$. Its application to the initial density operator $\hat{\rho}(\mathbf{k}_1,0)$ yields the density operator at the moment t, when the second radiation is emitted in the direction $\mathbf{k}_2$:

$$\hat{\rho}(\mathbf{k}_1,t)=\hat{\Omega}(t)\hat{\rho}(\mathbf{k}_1,0) \qquad (2\text{-}62)$$

The directional correlation function (2-17) of the nuclear γ-γ cascade is then simply given by the expression

$$W(\mathbf{k}_1,\mathbf{k}_2,t)=\mathrm{Tr}\{\hat{\rho}(\mathbf{k}_2,0)\hat{\Omega}(t)\hat{\rho}(\mathbf{k}_1,0)\}, \qquad (2\text{-}63)$$

where the two density operators have the form discussed in **2.1**.

If the system under consideration is governed by a Hamiltonian, H, which does not depend explicitly on time, the evolution superoperator can be easily found by the Schrödinger-von Neumann equation:

$$\frac{d}{dt}\hat{\Omega}(t)=-\frac{i}{\hbar}H^{\times}\hat{\Omega}(t), \qquad (2\text{-}64)$$

$H^{\times}$ is the so-called Liouville operator, which is adjoined to the Hamiltonian H of the system in such a way that $H^{\times}$ acting on any operator A is equivalent to the commutator of H and A, i.e.

$$H^{\times}A=[H,A]. \tag{2-65}$$

If we assume that in the course of time the nuclear environment changes its state so that the probability $P_{a\rightarrow b}(\tau_1,\tau_2)$ of finding the system at a moment τ_2 in the state b when it was in the state a at $\tau_1 \leq \tau_2$

(1) is independent of the "history", i.e. of the system's states before τ_2 and

(2) depends only on the time interval $t=\tau_2-\tau_1$,

then we have

$$\frac{d}{dt}\hat{\Omega}(t)=(-\frac{i}{\hbar}H_{St}^{\times}+\hat{R})\hat{\Omega}(t), \tag{2-66}$$

or

$$\hat{\Omega}(t)=e^{(-\frac{i}{\hbar}H_{St}^{\times}+\hat{R})t}, \tag{2-67}$$

where $-\frac{i}{\hbar}H_{St}^{\times}+\hat{R}$ is the Blume matrix, $H_{St}^{\times}$ is the direct product of the static Liouville operators $H^{\times}$ for each of the efg states through which the system fluctuates, and $\hat{R}$ is a matrix of transition probabilities for the transitions between the various efg states.

Specializing to electric quadrupole interactions and I=5/2 and allowing fluctuations among three states with axially symmetric efgs, with axes of symmetry along x, y, z, respectively, then $G_{22}(t)$ is a weighted

average of the time-dependent operator $e^{(-\frac{i}{\hbar}H_{st}^{\times}+\hat{R})t}$. Because the Blume matrix is complex, non-Hermitian in general, its eigenvalues are complex, and instead of simple Bohr frequencies we obtain a sum of complex exponentials:

$$G_{22}(t)=\sum_{q} G_{22}(q)e^{-\lambda_q t+i\omega_q t} \qquad (2\text{-}68)$$

The summation runs over the complex eigenvalues of the Blume matrix, $-\lambda_q+i\omega_q$.

When the fluctuation rate, w, is small, the effect of $\hat{R}$ is small and we obtain the Bohr frequencies for all the static states among which the system fluctuates. When w is large, on the other hand, if all the static states in $H_{st}^{\times}$ average to zero efg, then we just get exponential decay, i.e. damping due to the fluctuations.

William Evenson[48] called the particular model discussed above XYZ model and calculated $G_{22}(t)$ numerically for a wide range of parameters. The results are shown in Fig. 2.3. Fig. 2.4 shows the static frequencies (ω_1, ω_2, ω_3) (a) and the damping rate (b) as a function of the jumping rate, w. We can see that in the small w and large w limits, the damping λ_i (i=0,1,2,3) keep a constant ratio over a very large range of w/ω_Q, except for the very narrow region where λ reaches its maximum.

We take the following values for the two limiting cases:

for small w (XYZ(low))

$$\lambda_1/\lambda_0=1.09 \qquad \lambda_2/\lambda_0=1.22 \qquad \lambda_3/\lambda_0=1.43\ ,$$

$$G_{22}(t) = S_{20}\exp(-\lambda_0 t) + S_{21}\exp(-\lambda_1 t)\cos(\omega_1 t) + S_{22}\exp(-\lambda_2 t)\cos(\omega_2 t) + S_{23}\exp(-\lambda_3 t)\cos(\omega_3 t) \qquad (2\text{-}69)$$

where the S_{2n} are the same as the static case (2-58)-(2-61).

for large w $\lambda_1/\lambda_0=0.266$, $\lambda_2/\lambda_0=1.681$, $\lambda_3/\lambda_0=2.422$,

$$G_{22}(t) = 0.5714 \times \exp(-\lambda_0 t) + 0.3032 \times \exp(-\lambda_1 t) + 0.0968 \times \exp(-\lambda_2 t) + 0.0286 \times \exp(-\lambda_3 t). \quad (2\text{-}70)$$

We have used these two limits in fitting our data.

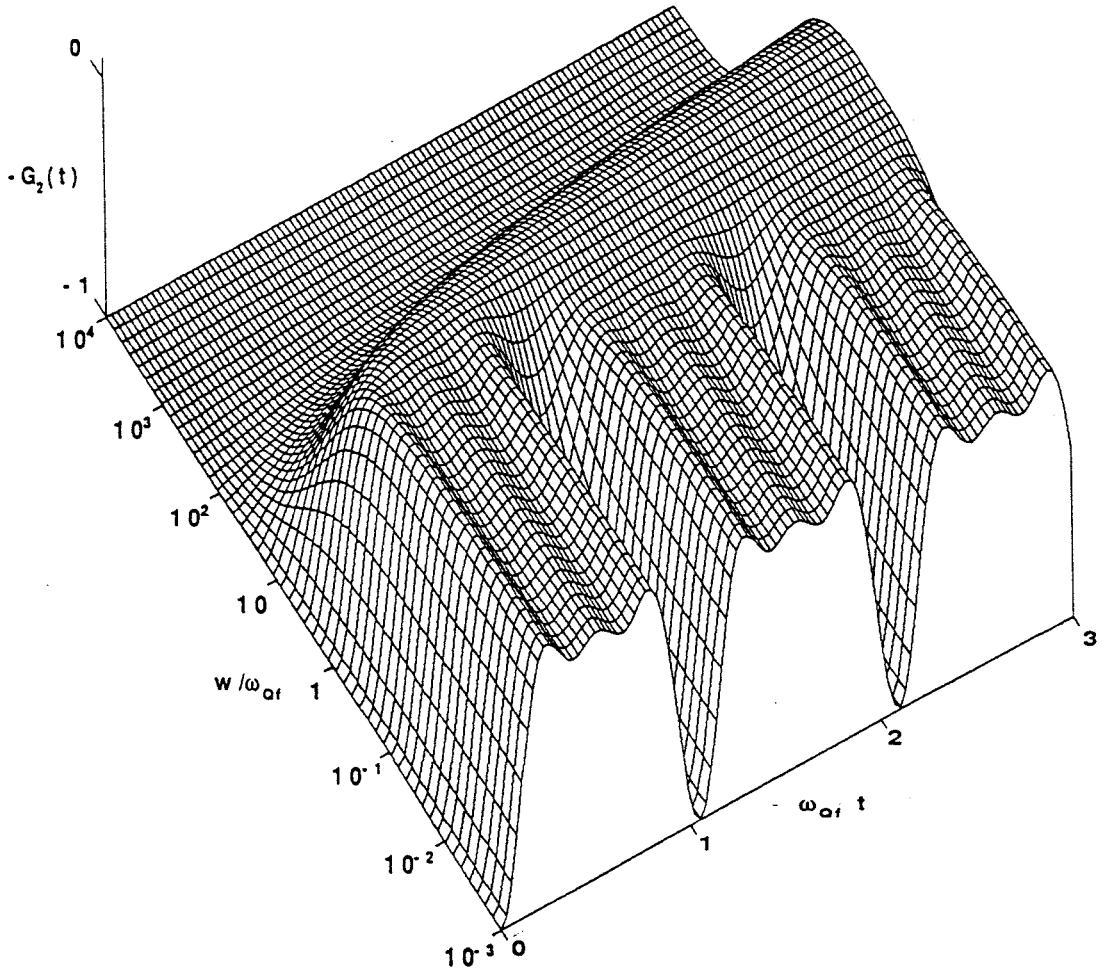

2.3 XYZ model: $-G_2(t)$ as a function of time t and fluctuation rate w.

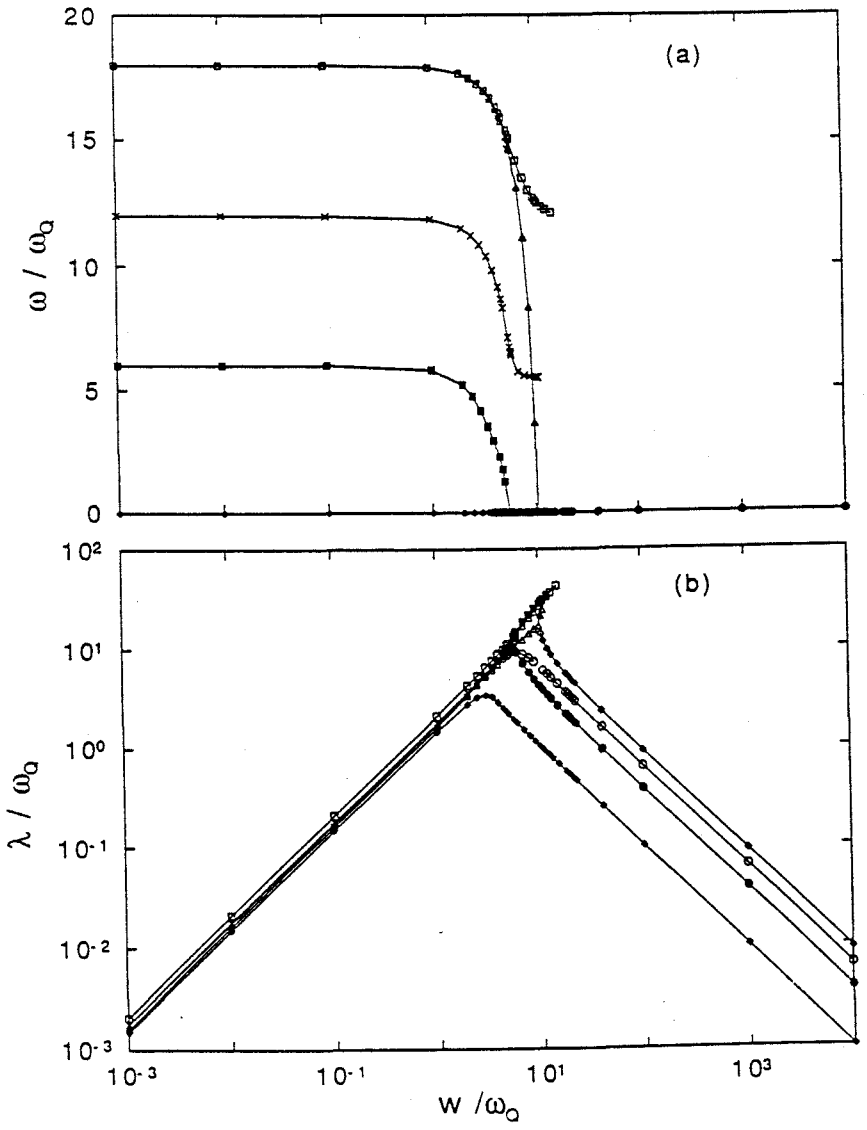

Fig. 2.4 XYZ model: (a) frequencies and (b) damping rates as a function of efg fluctuation rate w.

3. Experimental arrangements

There are several commonly used hyperfine techniques, e.g. Mössbauer Spectroscopy (MS), Nuclear Magnetic Resonance (NMR), Nuclear Quadrupole Resonance (NQR), Electron Spin Resonance (ESR) and Perturbed Angular Correlation Spectroscopy (PAC). Most of the hyperfine techniques are very well known and are widely used for research in physics, chemistry, biology, geology etc., and one can buy commercial NMR, NQR, ESR and MS spectrometers. Even though PAC was found in the early 1950's, earlier than Mössbauer Effect, one still can't buy a commercial PAC spectrometer up to now. To use the PAC technique, one has to build a spectrometer from standard electronic components. The spectrometer that we used in this work was built by Professor John A. Gardner's research group and has been revised by several generations of graduate students. At present we are still in the process of replacing the old Tandy/Radio Shack Color Computer with an IBM-PC XT and improving the measuring speed, data capacity, and automation ability of the spectrometer. The discussion below is confined to our present spectrometer status.

3.1 PAC spectrometer

The function of a γ-γ PAC spectrometer is to detect the two correlated gamma-rays emitted in the cascade by a tracer nucleus and to determine the time separation between them. This work was carried out using a conventional four-detector PAC spectrometer[49]. A Tandy/Radio

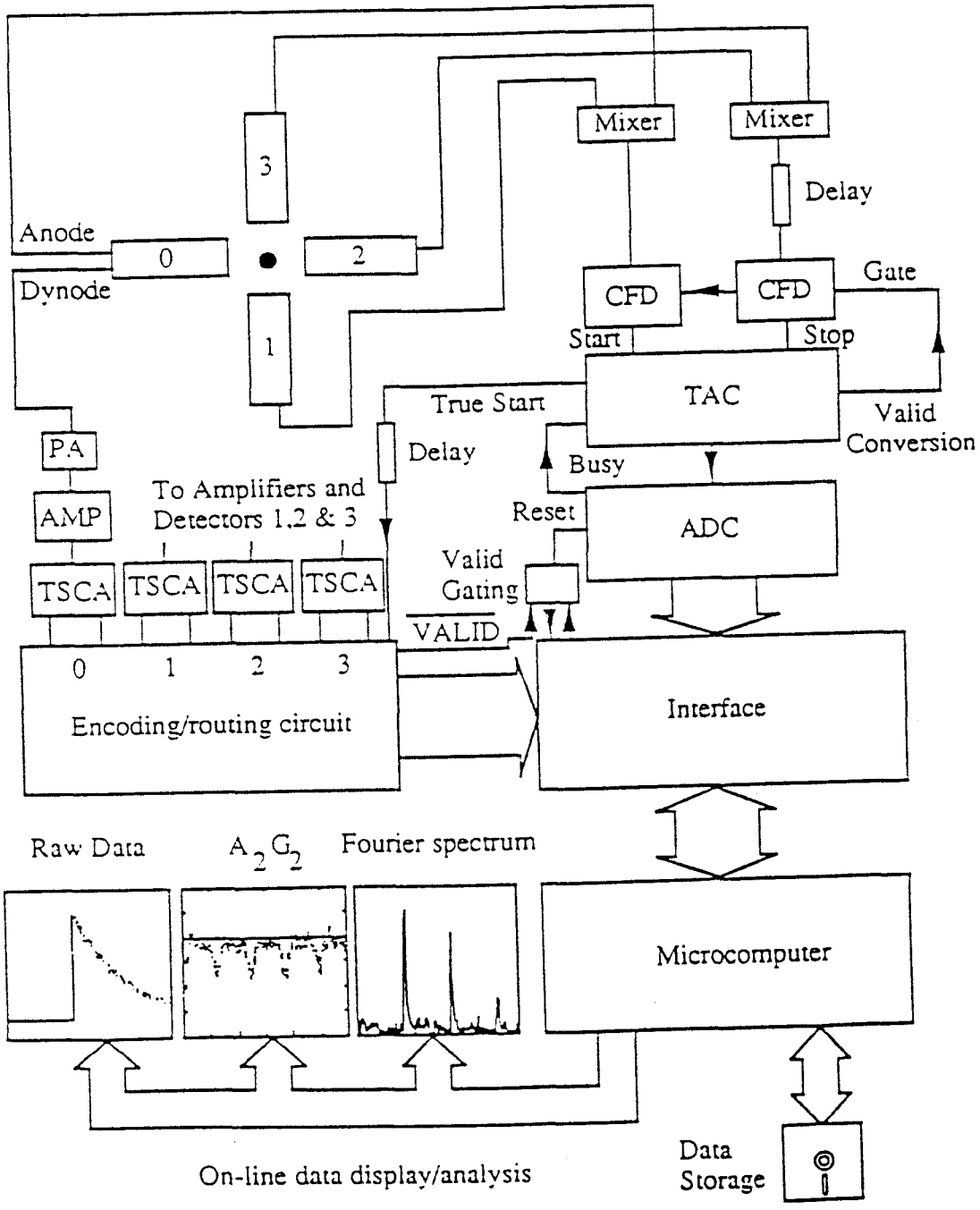

Fig. 3.1 The functional block diagram of the PAC spectrometer.

Shack Color Computer (CoCo) was used to control the spectrometer. The functional block diagram of the spectrometer is illustrated in Fig. 3.1. The four gamma-ray detectors are placed at 90 degree angle intervals in a plane with the source at the center. Each detector is driven by its own high voltage power supply and furnishes two signals for each absorbed photon: a dynode signal (energy information), and an anode signal (timing information). The timing signal provides the information about the time that the gamma-ray enters the detector and the energy signal is proportional to the energy that the gamma-ray deposits on the scintillation crystal.

The energy pulses from each detector are shaped and amplified by a preamplifier and then a linear amplifier. The resulting bipolar pulse is fed into a laboratory-built twin-single-channel-analyzer (TSCA).

Each TSCA is adjusted to detect both γ_1 and γ_2 (Fig. 3.2). The two

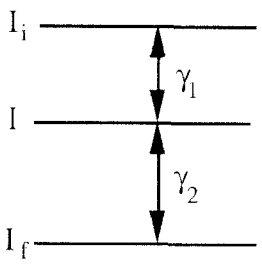

Fig. 3.2 Gamma-rays detected by TSCA.

signals from each TSCA are fed into a laboratory-built encoding/routing circuit for further determining the sequence of the correlated events. The encoding/routing circuit is designed so that the simultaneous detection of more than one "start" (the first emission γ_1) and/or "stop" (the second

emission γ_2) event is considered invalid. A conversion is accepted as a valid "normal" event only if a TSCA of detector 0 or 1 indicates a γ_1 was absorbed, and a TSCA of detector 2 or 3 indicates a γ_2 was absorbed. If a γ_2 is detected by detector 0 or 1 and γ_1 is detected by detector 2 or 3 then it is called a valid "reverse" event. The information about the sequence of the two correlated gamma-rays is called routing information.

The timing signals (from detectors 0, 1, 2, 3) are fed into constant-fraction-discriminators(CFD). The signals are shaped and discriminated by the CFD. The start signals (0 and 1) are sent through a mixer to the start input of a time-to-amplitude converter (TAC). The stop signals (2 and 3) are sent through a mixer and a delay cable to the stop input of the TAC. This delay cable is used to move the time-zero point of a prompt event to the mid range of the selected TAC range.

Once the TAC has received a start and a stop pulse, the CFDs are gated off until the conversion is completed to avoid interference caused by the incoming CFD signals. For each successful conversion, the TAC generates a unipolar pulse whose pulse height is proportional to the time separation between the start and the stop pulses. In this work the time range of the TAC is chosen to be 1μs, which is suitable for $^{111}In/^{111}Cd$ PAC measurements. The ADC is set to convert a full scale TAC pulse (10V, which corresponds to the time separation of the start and stop pulses of 1μs) into 512 channels. As soon as the ADC starts the conversion, a busy signal is generated to gate off the TAC until the ADC is free for the next job. Eventually the ADC is read by the computer through the interface board. The computer interface is built around a peripheral interface adapter (PIA) chip (Synertek, Santa Clara CA, type

SY 6522) and connected to the CoCo via a bus expansion box (Basic Technology, Ortonville, MI, model BT 1000).

Most of the spectrometer's software is written in BASIC, but the time critical parts are written in machine language. The most time-critical part is the interrupt service routine because the time spent in reading the PIA ports largely determines the dead time of the system. On entry to the interrupt service routine, the processor register, status and return address are saved on the stack. After the PIA registers are read, the ADC is reset and the next interrupt can occur while the computer is still processing the previous one. This sets an upper limit on the rate at which interrupts can be accepted. If the interrupt rate becomes too high, the stack overflows, and the computer crashes. In practice, this has not been a problem since the activity of the sample can be controlled through the sample making process.

The interrupt service routine examines the VALID bit (most significant bit of the routing information) and returns immediately from interrupt if the event is invalid. In the case of a valid interrupt, a memory location is decided from the data received from the PIA input lines. The computer's random access memory (RAM) between address &4000 and &7000 is divided into 16 sectors corresponding to the pairs of detectors that detect γ_1 and γ_2 . For example, sector 0/2 holds the spectrum of events for which γ_1 is detected in detector 0 and γ_2 in detector 2, etc. Each sector consists of 512 channels and each channel is represented by two bytes. The routing information identifies the memory sector, while the ADC conversion result designates the offset of a particular event in that sector. As soon as the channel which corresponds to the detected

events is identified the count in that channel is increased by one and the routine returns. The channel representing time zero (of a prompt event) is located near mid-range of the TAC (channel 256), so that in addition to the "normal" spectra (sectors 0/2, 0/3, 1/2, and 1/3) the "reverse" spectra (sectors 2/0, 3/0, 2/1 and 3/1) can also be accumulated.

While not processing interrupts, the computer has been programmed to perform other tasks like displaying accumulated counts vs. channel (time) for each sector on an oscilloscope, determining the accidental coincidence counts, calculating $A_2G_2(t)$, or computing the Fourier transform of the $A_2G_2(t)$ function, etc. With this configuration, it is very easy to monitor the progress of the experiment and to detect faults in the spectrometer or sample at an early stage and take proper measures to correct them.

For a typical run, about 3×10^4 to 6×10^4 counts per channel at the peaks of the spectrum are accumulated. A typical run takes about 10 to 24 hours to accumulate two statistically independent spectra ("normal" and "reverse") with good statistics. When sufficient data have been collected, the spectra and relevant information such as sample name, date, temperature and calibration information are saved to a floppy disk for later analysis on an Apple Macintosh II computer.

The gamma-ray detectors used in this work are barium fluoride (BaF_2) scintillators (Harshaw/Filtrol Partnership, Solon, OH) mounted on a XP 2020Q photomultiplier (Amperex Electronic Corp., Hicksville, NY). The base used on each detector is an Amprex S-563 unit. Each detector consists of a 1.5"×1.5"×1.5" cylindrical BaF_2 scintillator. The use of BaF_2 in $\gamma-\gamma$ TDPAC measurements of condensed matter properties has been

reported by several groups.[50,51] Detailed properties of BaF_2 scintillators can be found in ref. 52.

A photon entering the scintillator interacts with the material. The intensity of the resulting fluorescent light is proportional to the energy the photon deposited in the scintillator. The fluorescent light enters the window of the photomultiplier, hits the cathode, which is coated with photoelectric material, and frees electrons which are then accelerated and multiplied along the dynode chain.

The face and the sides of the scintillator are covered with 3 layers of proprietary ultra-violet light reflectory teflon tape and a layer of 5 mil aluminum foil to increase the light output. The crystal is mounted using General Electric Viscasil 600 000 silicone fluid as the optical coupling fluid and the whole assembly is covered with an aluminum can to stabilize and block stray light. This optical coupling fluid exhibits a near unity transmissivity for light with wavelength greater than 190 nm. The detector is further covered with magnetic shielding to reduce external magnetic fields. All four detectors are attached to aluminum frames and are free to slide along tracks at 90° angles from each other.

To use TDPAC to study the properties of solid state materials, one often wishes to control the applied conditions, e.g. temperature, pressure, and then study how the perturbed angular correlation will change with the applied condition. Therefore we need a furnace to run the sample at high temperatures. Some of the constraints which must be considered when designing the furnace are: (i) The outer surfaces of the furnace must be at room temperature so that the detectors work at the same temperature independent of the sample temperature. (ii) The furnace body should be

thin and constructed using a low Z material so as not to reduce significantly the intensity of the gamma-rays emitted by the sample. (iii) The furnace must work reliably over several weeks or more at as high temperature as we need. The furnace that we are using now can work reliably at as high as 1400°C. This furnace is built around a furnace tube closed at the bottom with an inner diameter of 3/8" and an outside diameter of 1/2". The heating element is cut from a 5/1000" (5 mil) thickness graphite foil with the help of a predrawn paper pattern.(Fig. 3.3(a)).

The heating element is wrapped around the furnace tube and covered with one layer of alumina thermal insulation and two layers of 1 mil zirconium foil. The zirconium foil serves two purposes here: heat shielding and oxygen getter to prevent the heating element from oxidizing. Two pieces of 10 mil copper foil are used as the current leads which are connected to the vacuum feed-through.

The heating unit is mounted in an aluminum housing surrounded by a water-cooled jacket.(Fig. 3.3(b)). A laboratory-built AC power supply is used to power the furnace. The open end of the furnace tube is exposed to the air, and the sample and a Pt-Pt/10%Rh thermocouple is placed in the center of the tube. The temperature is controlled by a proportional controller (Omega Engineering, Stamford CT, model 49) connected to the thermocouple. A moderate vacuum which can be achieved by a mechanical forepump is sufficient to prevent the heating element from oxidizing. A well-constructed furnace typically will last for six or even more months under normal operation up to 1200°C.

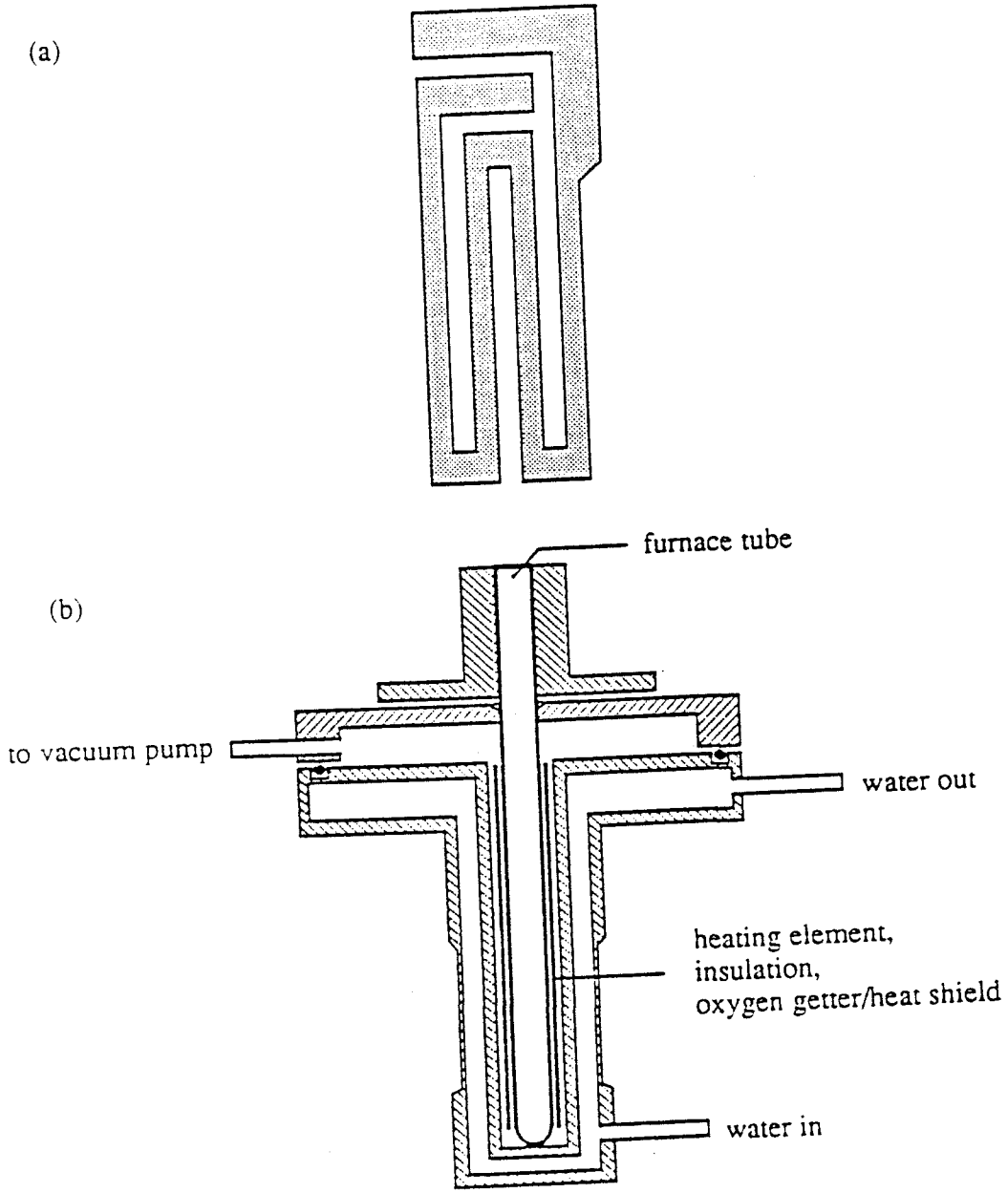

Fig. 3.3 (a) The graphite heating element and (b) sectional view of the PAC furnace.

Temperature profiles of the furnace have been measured at various temperatures up to 1400°C. The temperature differences between all sides of a sample are slightly less than 10°C at 1400°C. Even though the temperature cycle of the temperature controller is smaller than 2°C, the temperature uncertainty of the sample should be considered to be 10°C at 1400°C and less at lower temperatures.

3.2 Spectrometer calibration

The energy calibration is performed with the sample which is currently being investigated in place and a MCA connected to the output of the linear amplifier. With the MCA gated by the output signal of the TSCA, the windows of the TSCA are set such that only the 171 keV (γ_1) or 245 keV (γ_2) peak is detected when one is using $^{111}In/^{111}Cd$ as the nuclear probe.

The task of time calibration consists of three parts: (i) the time scale of the TAC must be determined; (ii) the time resolution of the spectrometer must be determined; (iii) the lengths of the cable which carry timing signals must be adjusted such that the time-zero channels for all memory sectors are the same. Before the time calibration can be performed, the energy windows of the TSCA must be adjusted very carefully to respond to the appropriate energy peaks of the PAC nuclide being used in the experiment.

A time calibrator is used to determine the absolute time scale of the TAC. The time calibrator generates Start and Stop pulses separated by integer multiples of a chosen constant period. These peaks are fed directly

into the TAC inputs, and a calibration program accumulates the periodically repeating peaks and evaluates the time calibration by doing a least squares fit. The time calibration gives the absolute time scale for the TAC, i.e. time per channel. The time calibration for all the data collected in this work is 1.89 ns/channel with an error of less than 0.4%.

The time-zero channel of each memory sector and the time resolution of the spectrometer are determined using a ^{22}Na source. This 2.6 years half-life isotope decays through β^+ emission process to its daughter isotope ^{22}Ne. The positron eventually annihilates with an electron in the surrounding material. In most cases two photons, each with energy 511 keV, are created simultaneously and emitted in opposite directions. Occasionally, the photon pair will be absorbed by two detectors and the resulting prompt spectrum accumulated in the corresponding memory sector ideally should be a delta-function. In reality, the prompt peaks have a Gaussian distribution due to the finite time resolution of the spectrometer.

By adjusting timing signal cables, the time-zero channels of all memory sectors are aligned to within a few tenths of a channel width. After prompt peaks for each detector pair have been accumulated for the same time interval, the location and full width at half maximum (FWHM) for every prompt peak are determined, and the instrumental resolution functions for both the "normal" and "reverse" spectrum are calculated. The finite time resolution of the spectrometer is taken into account by the instrumental time resolution function. The instrumental time resolution function is calculated by the relative ratio of the average counts in each of the four channels before and after the time-zero channel to the average

counts of the time-zero channel. Here the 'average' is taken for the four "normal" or "reverse" sectors respectively. Then this function is normalized to 255 in the time-zero channel.

Finally, the time calibration, the time-zero channel and the instrumental time resolution function are stored in the computer. For each experiment, this information is saved with experimental data onto a floppy disk.

3.3 Sample preparation

One basic requirement of a good PAC sample is to incorporate the desired radioactive tracer into the bulk of the studied material. A precipitation method for the ceria samples was developed in our laboratory by Dr. James A. Sommers (Teledyne Wah Chang Albany Albany, OR).

Pure and lightly doped cerium oxide samples used in this study were prepared from cerium ammonium nitrate solution ($(NH_4)_2Ce(NO_3)_6$), whose concentration is known accurately. An appropriate amount of this stock solution mixed with solutions of the dopant cations is taken and a drop or two of the radioactive ^{111}In in HCl are added. (Y and In were added to parent Ce solutions as their nitrates. Nb and Ta solutions are more complicated requiring an oxalic acid solution of niobium hydrous oxide and a sulfuric acid solution of $TaCl_5$, respectively). The resulting solution is added to a concentrated ammonium hydroxide solution with constant stirring to precipitate the cerium hydrous oxide. The precipitate is filtered, washed and dried under the heating lamp

until most of the water has been evaporated and a loose, fine powder remains. Then the powder is taken to 1550°C (for most of samples) for 6 hours.

Typically a ceria PAC sample containing ^{111}In has a mass of about 100-150mg. The concentration of ^{111}In is about 10^{-9} relative to the cation atoms and the radioactivity intensity is a few μCi.

3.4 Data reduction

After each run is completed. The experimental data and all the run information are saved onto a floppy disk. These data are read by a laboratory-developed program on the IBM XT computer. This program converts the data from CoCo format to IBM format, checks all the data channels for possible data overflow, and corrects them if any are found. Then it calculates the average background for each sector corresponding to a detector pair. For each detector pair i/j, the raw data contained in its corresponding memory sector i/j can be expressed as

$$D_{ij}(\theta,t)=\frac{1}{\tau_N}e^{-\frac{t}{\tau_N}}e_i e_j N_0 W(\theta_{ij},t)+B_{ij} \qquad (3\text{-}1)$$

and the background-corrected counting rate is

$$C_{ij}(\theta,t)=D_{ij}-B_{ij}=\frac{1}{\tau_N}e^{-\frac{t}{\tau_N}}e_i e_j N_0 W(\theta_{ij},t) \qquad (3\text{-}2).$$

Here θ_{ij} is the angular separation between the ith and jth detectors. N_0 is the number of the parent isotope at t=0 and τ_N is the mean life of the intermediate state ($5/2^+$ state of the ^{111}Cd, τ_N=85ns). e_i is the single

efficiency of ith detector B_{ij} is the average background for sector i/j. The background counts B_{ij} are taken from the averaged counts of the channels from the 90th to 190th channels before the time-zero channel of the sector i/j. $W(\theta_{ij},t)$is the angular correlation function which contains all the information about the interaction of the probe with its environment.

As discussed in **2.1**, the angular correlation function for a polycrystalline PAC experiment can be written as

$$W(\theta,t)=\sum_{k=0,even}^{k_{max}} A_{kk}G_{kk}(t)P_k(\cos\theta). \qquad (3\text{-}3)$$

For ^{111}Cd, $k_{max}=4$, $A_{44}\approx 0$, and A_{22} has conventionally been denoted as A_2, and G_{22} as G_2. Then,

$$W(\theta,t)\approx 1+A_2G_2(t)P_2(\cos\theta). \qquad (3\text{-}4)$$

We further define a spectra-ratio for the normal spectrum as[53]

$$R_n = 2\frac{(C_{02}C_{13})^{1/2}-(C_{03}C_{12})^{1/2}}{(C_{02}C_{13})^{1/2}+2(C_{03}C_{12})^{1/2}}, \qquad (3\text{-}5)$$

and for the reverse spectrum as

$$R_r = 2\frac{(C_{20}C_{31})^{1/2}-(C_{30}C_{21})^{1/2}}{(C_{20}C_{31})^{1/2}+2(C_{30}C_{21})^{1/2}}. \qquad (3\text{-}6)$$

Using equation (3-2) and (3-4), for both normal and reverse, the spectra-ratio reduces to

$$R(t) = 2\frac{A_2G_2(t)[P_2(180°)-P_2(90°)]}{3+A_2G_2(t)[P_2(180°)+2P_2(90°)]}. \qquad (3\text{-}7)$$

Since $P_2(180°)=1$ and $P_2(90°)=-0.5$,

$$R(t) = A_2G_2(t). \qquad (3\text{-}8)$$

The experimental $A_2G_2(t)$ function, thus, is defined as the spectra-ratio. The $A_2G_2(t)$ for both "normal" and "reverse" spectra were calculated and saved to their corresponding files. The byte to byte translation of the raw data was also saved and transferred along with the $A_2G_2(t)$ files to an Apple Macintosh II computer via an external $5\frac{1}{4}$ in. floppy drive and the Apple File Exchange program on the Macintosh. The raw data are used to check the alignment of the time zero channels. If misalignment is found, the spectrometer is recalibrated.

Now we also have another version of the fitting program on IBM PC, developed by Mr. Randy Lundquist. It uses the same fitting program but more user-friendly. We can group our data to different stacks which have similar sites and fit each stack at a time. We can also look the fitted parameters on line, do least squares fitting to the parameters, or save them to a file, etc.

The Fourier transform (FT) is performed on most $A_2G_2(t)$ files to serve as a preliminary determination of essential PAC information, e.g. the number of possible probe sites, the PAC frequencies for each site etc. A nonlinear least-squares fitting routine[54] based on Marquardt's algorithm is used to fit the experimental $A_2G_2(t)$ function. In the fitting routine, an appropriate theoretical expression of the $A_2G_2(t)$ function is convoluted with the system time resolution function to account for the finite instrumental time resolution of the spectrometer. For multiple site spectra, the FT of the theoretical curve is performed to compare with the FT of the

experimental $A_2G_2(t)$ function. A block diagram view of the data reduction procedure is given in Fig. 3.4

As we noted in 2.1, the anisotropy A_2 depends only on the spins of the nuclear levels and multipolarities of the radiations. But in the experimental PAC work, one often finds that the anisotropy A_2 deviates from the calculated value[55] (for ^{111}Cd , A_2=-0.180(2)).

Several sources have long been known to cause this artifact:

(i) finite size attenuation- since real samples and detectors have finite size, the measured anisotropy is an averaged quantity which is smaller than the theoretical value.

(ii) Compton scattering- in this work, the sample is placed in a PAC furnace (see Fig. 3.3(b)). The gamma-rays need to penetrate layers of materials before reaching the scintillator. Some of the gamma-rays scattered through small angles without significantly losing energy and are then detected. This increases the apparent detection angle of the detector. Thus, Compton scattering yields a very similar effect to the finite size attenuation.

(iii) time zero channel misalignment- in the present method of fitting experimental $A_2G_2(t)$, even a very small time zero misalignment would affect the experimental $A_2G_2(t)$ which cause the fitted A_2 differ from the real one, since the spectra-ratio at time zero usually is a very sensitive function of the time zero alignment. Now we are improving this by fitting the $A_2G_2(t)$ from each sector of data, instead of from four sectors of data.

(iv) sample self-absorption-this happens most often for high Z samples. In these types of samples gamma-rays traveling in the 180° direction

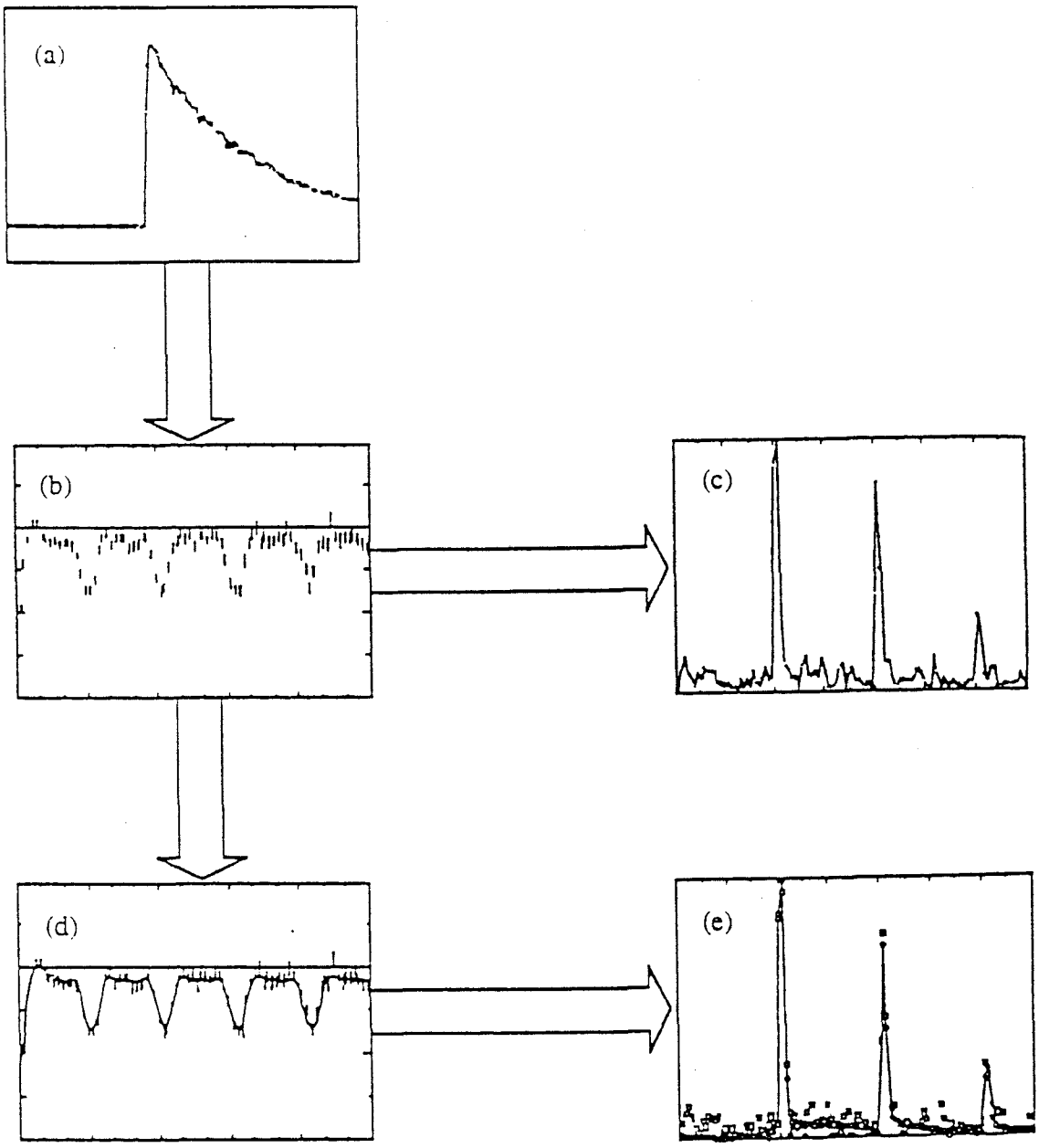

Fig. 3.4 Block diagram view of the PAC data reduction process.

are more likely to be absorbed than those in the 90° direction, especially for events that occur near the surface. In contrast to the previous three sources, sample self-absorption tends to enhance the magnitude of the anisotropy.

(v) radioactivity of the sample-when the sample is too strong, we are more likely to receive fault event as the true one because of the limited sampling rate. This effect usually gives smaller effective A_2.

Since it is almost impossible to account and correct for all the factors which result in the A_2 variation, an experimental determination of the effective A_2 of the PAC spectrometer is more practical. The effective A_2 can be measured easily if the perturbing fields on the nucleus can be removed, which occurs when the probe sits at the regular site of a perfect cubic lattice, or when the correlation time of the perturbing fields is very short, which usually occurs in molten metals and dilute aqueous solutions. Among several possible choices, the aqueous solution method is the best one for our purpose, since it avoids the difficulties of finding a perfect cubic lattice or of preparing the molten metal. A few drops of very dilute radioactive ^{111}In /HCl solution were injected into a 3mm ID one-end-closed quartz tube. This aqueous sample size is comparable with the real sample size, which is about $3\times3mm^2$ typically. The spectra-ratio is fitted to the expression

$$A_2G_2(t)=A_2^{eff}e^{-\lambda t}, \qquad (3\text{-}9)$$

the fitted A_2 is compared with measured A_2^{eff} in order to be sure of a good fit.

Two important physical quantities, the asymmetry parameter η and the magnitude of the electric field gradient V_{zz} can be derived from the fitted parameters for static electric quadrupole interaction. The asymmetry parameter η is related to the symmetry properties of the electric field gradient tensor at the probe site. The magnitude of the electric field gradient V_{zz} at the probe site can be represented as the sum of a lattice part due to the contributions of the ionic cores of nearby atoms, and an electronic part which arises from the influence of covalent bonds, conduction electrons, and unfilled electronic shells of the probe atom. Since CeO_2 is an insulator and Cd^{2+} has a closed electronic shell, the latter two should be negligible. However it has long been realized that even for a closed electronic shell probe, the electronic shell is distorted by the external electric field. The observed nuclear quadrupole interaction can be greatly enhanced by this. For a nuclear probe, the observed electric field gradient V_{zz} is related to the lattice EFG $V_{zz}(lat)$ (which is due to the ion cores in the lattice) by

$$V_{zz}=(1-\gamma_\infty)V_{zz}(lat) \qquad (3\text{-}10)$$

where γ_∞ is the Sternheimer antishielding factor which is negative for most ions. For the Cd^{2+} ion, the γ_∞ is -29.27[56]. This information allows one to compare the derived V_{zz} from PAC measurements with $V_{zz}(lat)$ from point ion calculation.

Even though in general we do not have an analytical theory for dynamic hyperfine interactions, we still can get certain information in some special cases. For example, in cases which obey the Abragam and Pound model, one can get information about the damping rate of the

nuclear correlation; in the case which obeys the stochastic XYZ model, one can find the fluctuation rate, the magnitude of the fluctuating electric field gradient, and the activation energy for the fluctuation. This information is very important for understanding the materials of interest.

4. Experimental results

In all the PAC spectra shown below, $A_2G_2(t)$ is used to represent the perturbation since A_2 is a constant which can be affected by some experimental artifacts. Usually one obtains smaller effective A_2 because of the experimental artifacts (see **3.4**). The "t" is the lifetime of the intermediate state of ^{111}Cd. The solid line represents fitted results and the error bars on each data point are the statistical errors.

4.1 Preliminary work on ceria

At the time that we started this work, we were unable to find any literature regarding the use of ^{111}Cd as a PAC probe for the study of the ceria system. Much effort was put into discovering the right experimental conditions for studying this system. We started with undoped ceria, which has the simple cubic fluorite structure. Because of its chemical similarities, ^{111}In nuclear probe most likely substitutes Ce in ceria. In the case of a perfect cubic crystalline sample, we should expect no perturbation to the γ-γ angular correlation due to the electrical quadrupole interaction, simply because the cubic environment won't produce any electric field gradient (efg) to interact with the nuclear quadrupole moment of the probe nucleus.

We used the precipitation method which is described in **3.3** to obtain amorphous ceria powder samples from cerium ammonium nitride solutions ($(NH_4)_2Ce(NO_3)_6$) prepared by Dr. James Sommers. Many samples were made from this batch which we call "batch one" for

reference. This powder sample then is poured into an alumina sample holder. It was synthesized in PAC furnace at about 900-1000℃ for over 6 hours with the furnace tube exposure to air. This gives a light yellowish powder. The color indicates a certain amount of impurities in the undoped ceria sample. A chemical analysis of the batch one solution is given in Table 4.1.

Table 4.1 Chemical analysis of batch one solution.

element	(ppm)	element	(ppm)
Al	4	Fe	1.4
La	132	Pr	57
Nd	96	Sm-Lu	<5

The typical spectra of undoped ceria samples when synthesized this way are given in Fig. 4.1. At low temperatures (<300℃), there is a fraction of the XYZ(low) site (A) and another site (X) which can be fitted to an exponential function or an extremely broadened static site. Above 300℃, the spectra can be fitted to an XYZ(high) site and a fraction of the X site.

To be sure the sample we made is indeed in the fluorite cubic structure, we made room temperature x-ray diffraction measurements on some ceria samples. They show the characteristic lines reported in the literature. Fig. 4.2 gives the x-ray diffraction pattern for undoped ceria. The aluminum peaks are due to the sample holder.

Undoped ceria PAC measurements were repeated for samples synthesized at different temperatures. Neither the XYZ site fraction nor

the X site fraction was reproducible. It has been known that ceria is an oxygen deficient system at high temperatures. Lack of oxygen would produce oxygen vacancies in the sample. We tried to flow oxygen onto the sample during synthesis and slow the cooling rate after it. By making the sample this way, we ensure the availability of oxygen and eliminate the possibility of quenching in oxygen vacancies due to a fast cooling rate. These procedures do not seem to affect the spectra. Instead we notice that the higher synthesis temperature results in a smaller fraction of the X site.

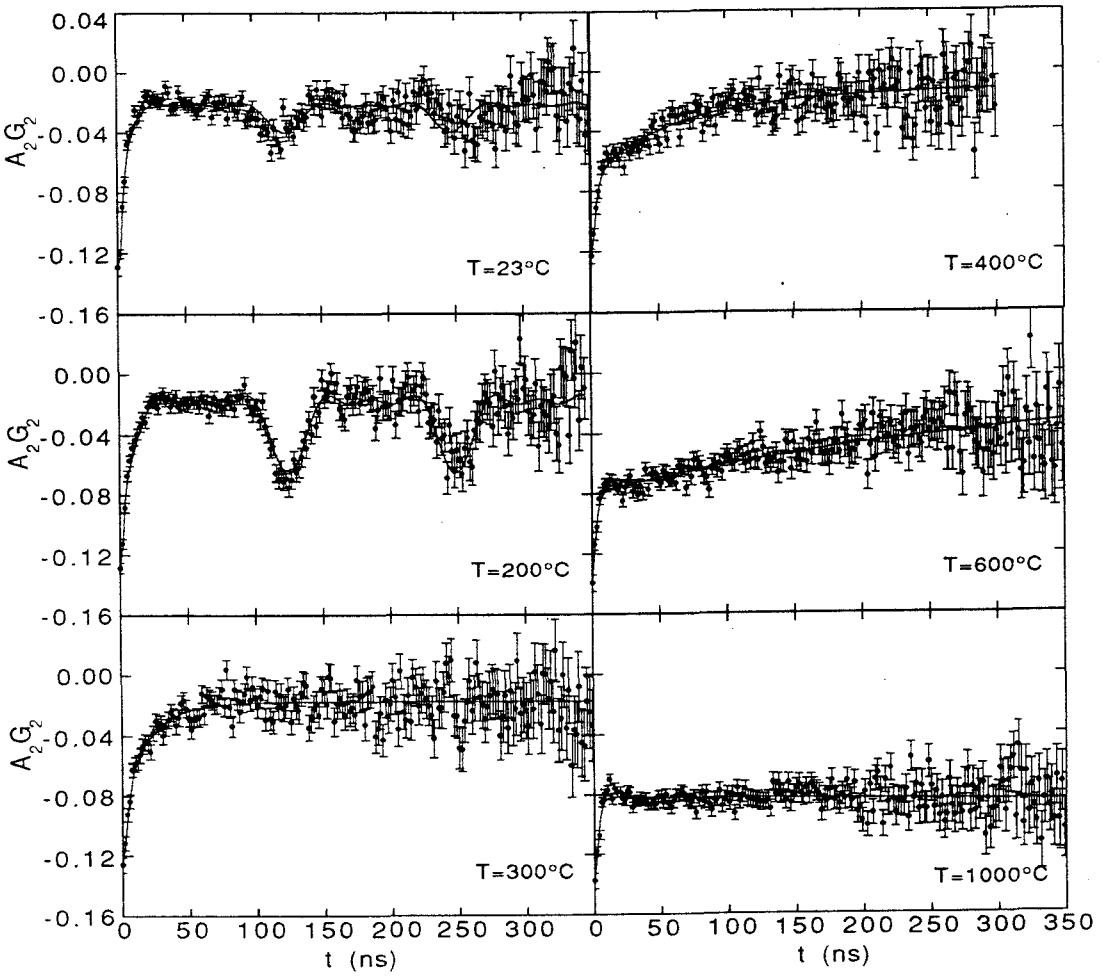

Fig. 4.1 Spectra of undoped ceria synthesized in PAC furnace.

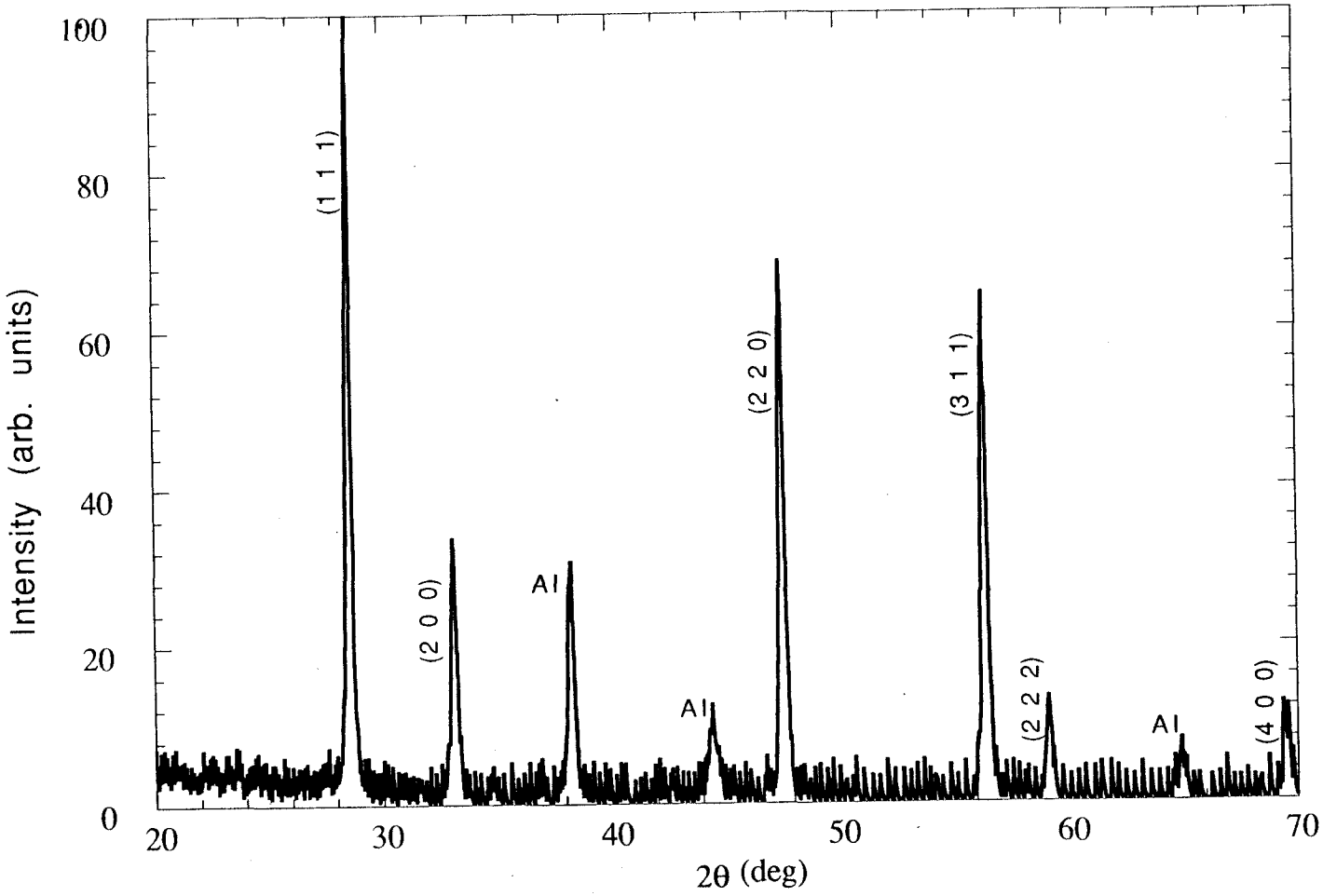

Fig. 4.2 Room temperature X-ray diffraction pattern of undoped ceria.

The crystalline grain size increases with increased synthesis temperature. If the small fraction of the X site at high temperatures comes from a grain boundary contribution, then we would expect to eliminate this site if we synthesize the sample at a higher temperature. We made a sample synthesized at 1600℃, and did not see the X site above 200℃. When the sample was made, it was poured onto an alumina capsule for synthesis, and then poured into a PAC sample holder afterward for further PAC measurements. The reason for not using a PAC sample holder to contain the powder during synthesis is to avoid the possibility of radioactive isotope diffusion into the PAC sample holder and the possibility of the alumina reacting with ceria at such high synthesis temperature. It turned out that this is a necessary consideration. If we synthesized the sample with a PAC sample holder and later took PAC measurements with the same sample holder, then we found a spectrum of both the sample holder and the sample of interest. In fact, the X site that we saw at high temperatures could come from both the crystal boundary and the nuclear probe in the sample holder because in the beginning of this work we synthesized the sample in the PAC furnace at about 900℃ and we took PAC measurements afterward without changing the sample holder.

To measure the crystal grain size, two nonradioactive samples were synthesized at 1000℃ and 1600℃ respectively. Scanning Electron Microscopy (SEM) was performed on these samples. Fig. 4.3 shows SEM images for these two samples. The average grain size is about 0.1-0.5μm and 5-10μm when synthesized at 1000℃ and 1600℃ respectively. The undoped ceria shows light beige color when synthesized at 1600℃

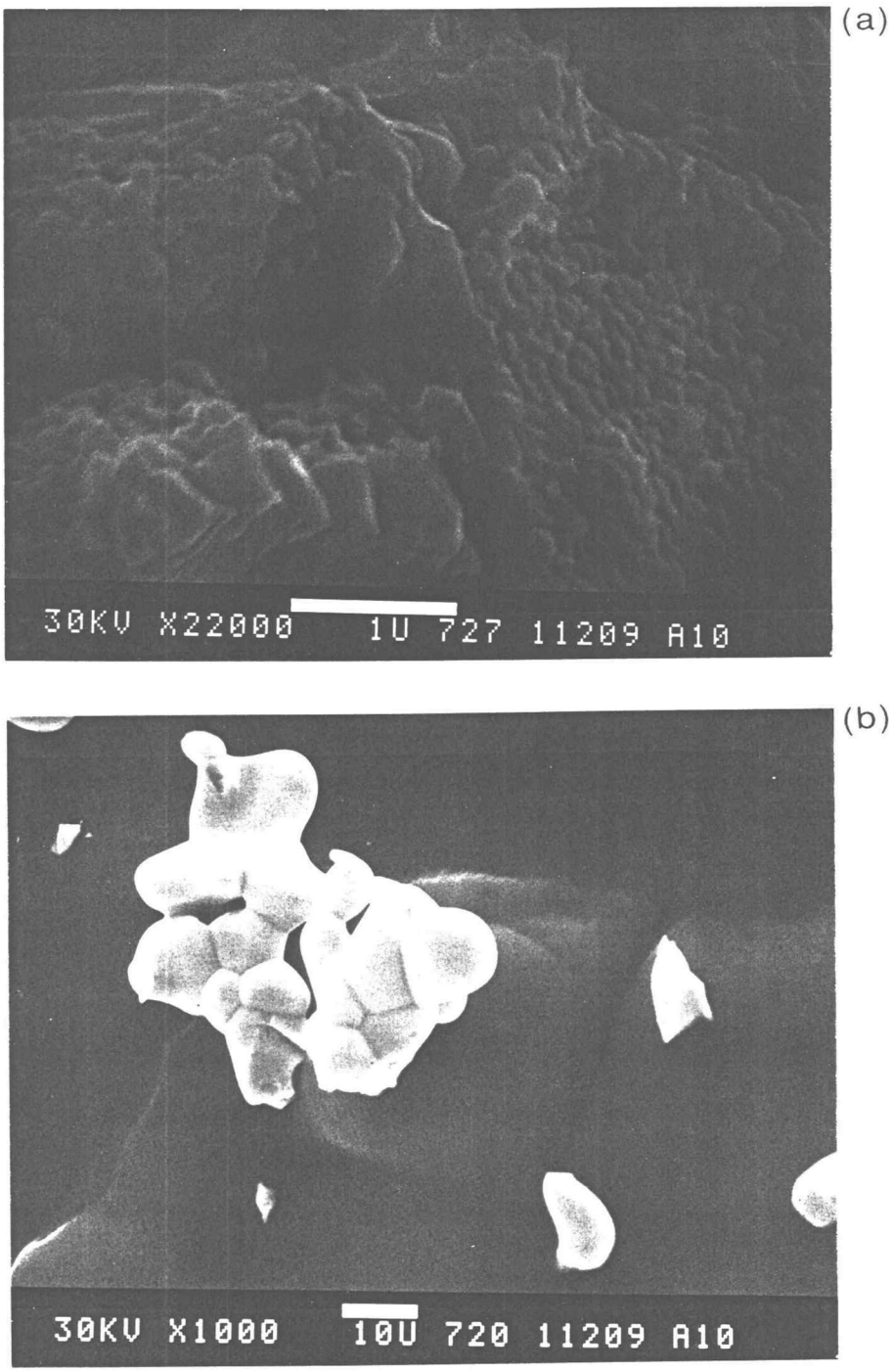

Fig. 4.3 SEM pictures of undoped ceria synthesized (a) at 1000℃ (b) at 1600℃.

For all the samples that we have used so far, an alumina capsule was used for synthesizing at 1550°C. To be sure that there is not any aluminum diffusion into the sample during synthesis, we made the following experiments. Instead of synthesizing samples in an alumina capsule, we used both alumina and zirconia capsules to synthesize the sample under the same condition. The samples were put into zirconia PAC sample holders and PAC measurements were made. We did not find any difference due to the type of container used during synthesis. We did find that some of the ^{111}In isotope diffused into the alumina or zirconia capsules during synthesis. We made similar experiments using a platinum holder for synthesis. The PAC spectra do not seem to differ from those of samples synthesized in other holders. But we learned that it is very important to use a "clean" sample holder other than the one used for synthesis to perform PAC measurements.

Our later samples are almost all synthesized at 1550°C for 6 hours. We also made experiments for samples synthesized at different temperatures. The results show that PAC samples should be synthesized at about 1200°C or above. By this synthesis procedure, we could get reproducible spectra. Above 200°C, we only have one XYZ site; no X site exists.

4.2 Undoped ceria results

We started with undoped ceria made from solution batch one. Typical spectra at elevated temperatures are shown in Fig. 4.4 (notice at

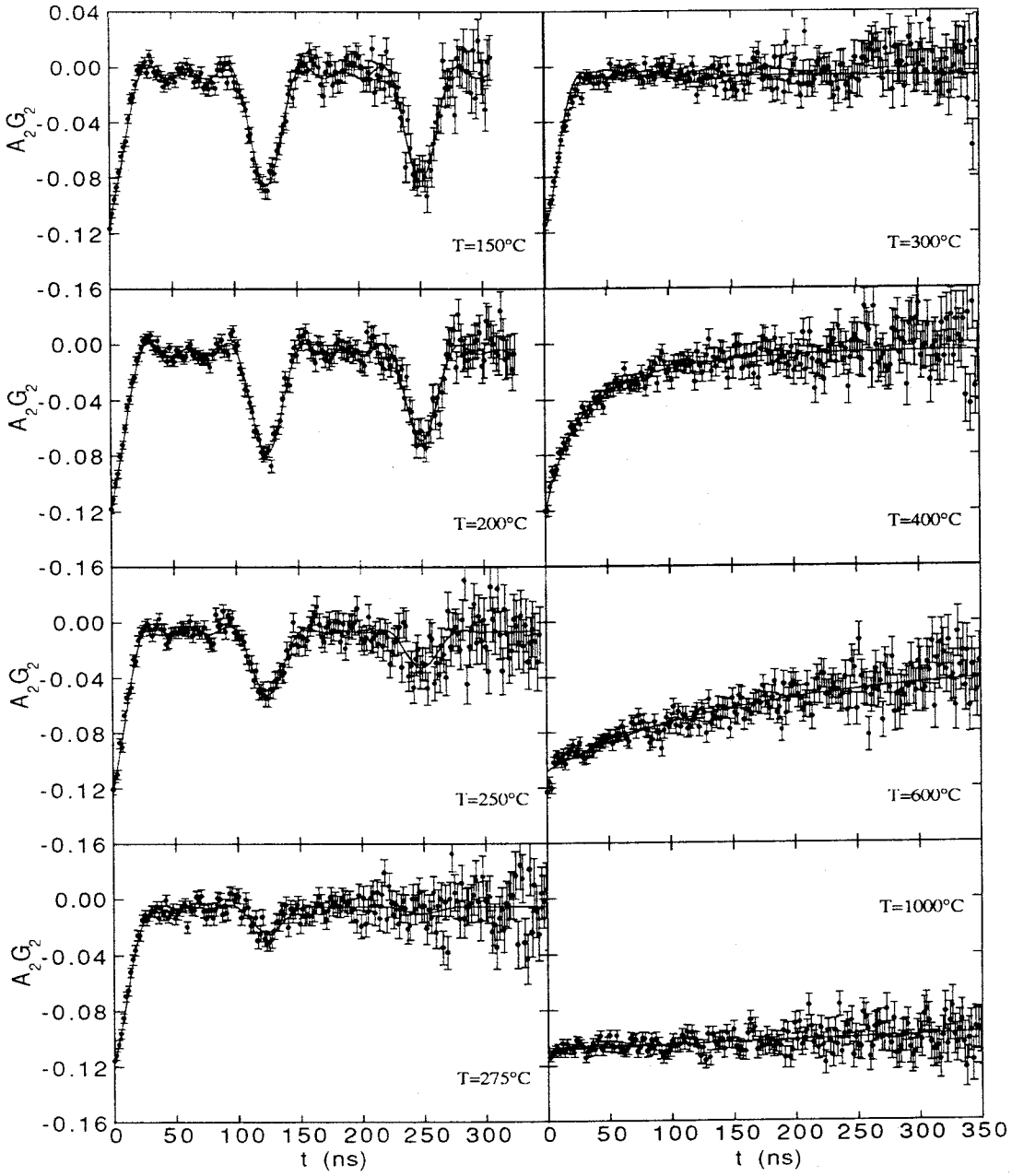

Fig. 4.4 Spectra of undoped ceria at elevated temperatures.

1000℃ the spectrum is essentially a straight line, whereas in Fig. 4.1, the spectrum includes a feature near t=0 due to the X site that is removed by better processing as discussed in **4.1**). Fig. 4.5 shows the ceria PAC spectrum at 150℃ and its Fourier transform; the insert shows the electric quadrupole interaction energy splittings and corresponding PAC frequencies.

Below 200℃, a very well defined static site was found. It has the constant axially symmetric frequencies for all temperatures below 300℃. At room temperature its site fraction counts about 40%, and its static oscillations in the PAC spectrum disappear when the temperature reaches about 300℃. The rest of the $G_2(t)$ function is not static and can be fitted to an exponential function or a very broadened static site with poorly-defined frequencies.

After confirming that the low temperature static site is not something which simply comes from experimental artifacts, we began to consider possible physical reasons for this site. It has been understood that the ceria system, especially trivalent-doped ceria, is oxygen-deficient. This means there are oxygen vacancies in this system. Let's think the picture that there is an oxygen vacancy trapped by a nuclear probe. Then this oxygen vacancy, which has equivalent charge +2 relative to the neutral lattice site, will produce an efg around the probe nucleus. When we increase the temperature, the trapped oxygen vacancy might obtain enough thermal energy to start jumping among equivalent trap sites or might even detrap. We should consider the simple case, where the oxygen vacancy is trapped at all temperatures that we measured.

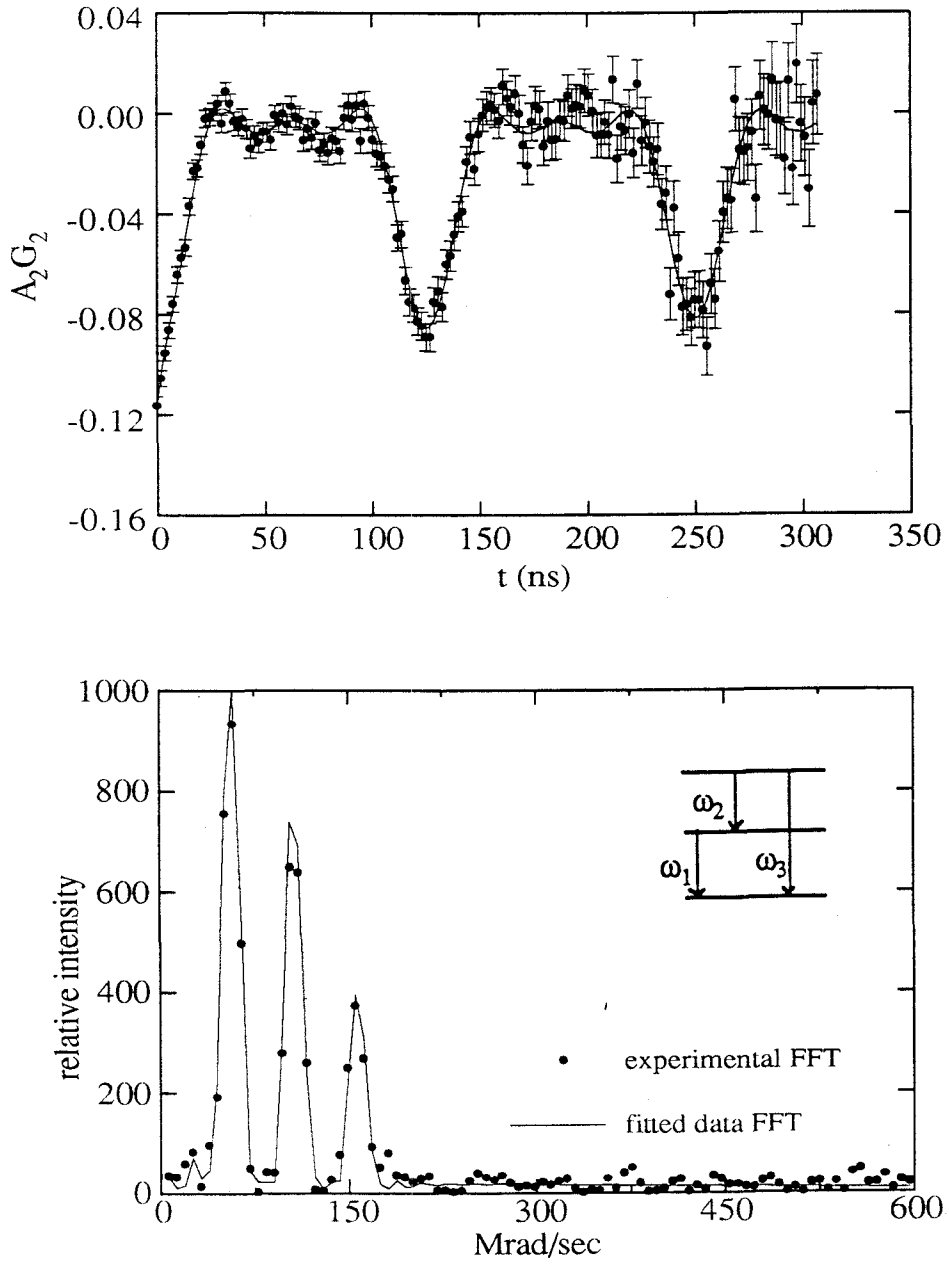

Fig. 4.5 Undoped ceria at 150°C (a) A_2G_2 (b) FFT.

This physical picture can be described by a model developed by Evenson et al.[48] which is explained in **2.3**. Using the numerical results in ref. 48, we can fit our data to two limiting cases: the low temperature limit for the XYZ(low) site (<350°C) and the high temperature limit for the XYZ(high) site (>350°C).

If the fluctuating efg we observed in undoped ceria is caused by a thermally activated oxygen vacancy hopping process, then we would expect the jumping rate $w \propto \exp(-\frac{E}{kT})$. So if we plot ln(w) vs. 1/T, we would expect a straight line whose slope is proportional to the activation energy E for oxygen vacancy hopping among equivalent trap sites. We made such a plot, and it did show a straight line. The fact that the XYZ model can fit this site is also evidence that the oxygen vacancy is very deeply trapped to even about 1000°C. The trapped oxygen vacancy only hops among equivalent trap sites, but does not detrap. If the oxygen vacancy detraps, the magnitude of the efg will change. But the XYZ model assumes a constant efg that only reorients among certain directions.

To estimate the position of this trapped oxygen vacancy, we made point ion calculations, assuming that only one oxygen vacancy with charge +2 is trapped at the first neighbor or the second neighbor oxygen lattice site. In this calculation, we used the Sternheimer antishielding factor for Cd^{+2} as -29.27. Table 4.2 gives the results of the point ion calculation and PAC experiment. These results indicate that if this low temperature static site is due to a trapped oxygen vacancy, it probably

comes from a second neighbor trap unless its relative charge state is other than +2.

Table4.2 Comparison of point ion calculation and experimental V_{zz}(lat).

V_{zz}(lat)	First Neighbor	Second Neighbor	Experimental
$\times 10^{16}$ Volt / cm^2	4.51	0.64	0.87

Though it is unlikely that 300 ppm trivalent impurities would cause about 40% of the nuclear probes to trap an oxygen vacancy near by, let's assume it is so for the moment. We explored the possibility by taking PAC measurements on pure ceria or pentavalent doped ceria. Since pure ceria has no impurity related oxygen vacancies, and we should expect simple fluorite cubic structure, then PAC spectra should give a constant straight line because there is no perturbation. If we dope enough pentavalent ions in ceria, all oxygen vacancies will eventually be compensated; we should also not see the XYZ site caused by trapped oxygen vacancies. The pentavalent doping experiments will be explained in detail in **4.4**.

We purchased some high purity ceria from Ames Lab (Ames, IA). Table 4.3 gives a chemical analysis of this high purity ceria. We call this batch solution "batch two" for later reference. The total trivalent impurities in batch two is only less than 20 ppm, much less than that in batch one. We used the same method as described previously to make samples. After a sample was synthesized at 1550°C for 6 hours, we obtained pure white powder! This is the color we should have for pure

ceria. But the undoped ceria sample from batch one was light beige color when synthesized at 1550°C, probably due to impurities.

Surprisingly, the spectra of pure ceria were essentially the same as those for undoped ceria made from batch one solution. From this experiment we drew the following conclusions:

Table 4.3 Chemical analysis of batch two solution.

element	ppm	element	ppm
Na	<2	Mg	<4
Al	<1	S	<6
Cl	<4	K	1
Ca	3	Fe	4
Nb	<1	Mo	2.3
Ba	<2	Hf	<2
W	<4	Re	<1
Os	<2	Th	<1
La	<2	Pr	<5
Nd	<2	Sm	<2
Gd	<2	Tb	<4
Ho	<2	Er	<2

The stochastic XYZ model is certainly the right model for the A site, the main site. We are also confident that the A site involves a thermally activated fluctuating efg. The X site, which appears only below 300°C and whose fraction decreases as temperature increases, is still a mystery at this stage. We could fit it to an exponential site or to a very broadened static site. Physically, we would like to sweep this site under the universal "aftereffects" rug. There will be more discussion about this X site in next chapter.

4.3 Y-doped and pumped ceria results

In practical applications, people have found that doping ceria with some trivalent oxides could increase the ionic conductivity of ceria. This phenomenon is understandable as the oxygen vacancy concentration in this system is increased by doping. Trivalent doping with Y_2O_3 is one of the common choices. For its chemical similarities, Y^{+3} would most likely substitute Ce^{+4} in ceria, this will give a charge -1 relative to the neutral lattice site. To compensate this negative charge, a doubly charged oxygen vacancy will be created for every two Y ions or a singlely charged oxygen vacancy will be created for every one Y ion doped. The ionic size of Y^{+3} is 0.89 and Ce^{+4} is 0.92[3].

To understand more about oxygen vacancy defects in ceria, we made a series of PAC experiments on Y-doped ceria. (All the undoped and doped ceria, except pure ceria, samples were made from batch one solution). Typical Y-doped ceria spectra are shown in Fig. 4.6 and Fig. 4.7, for Y-doping levels ($Ce_{1-x}Y_x$) x=0.2% and x=0.8% respectively.

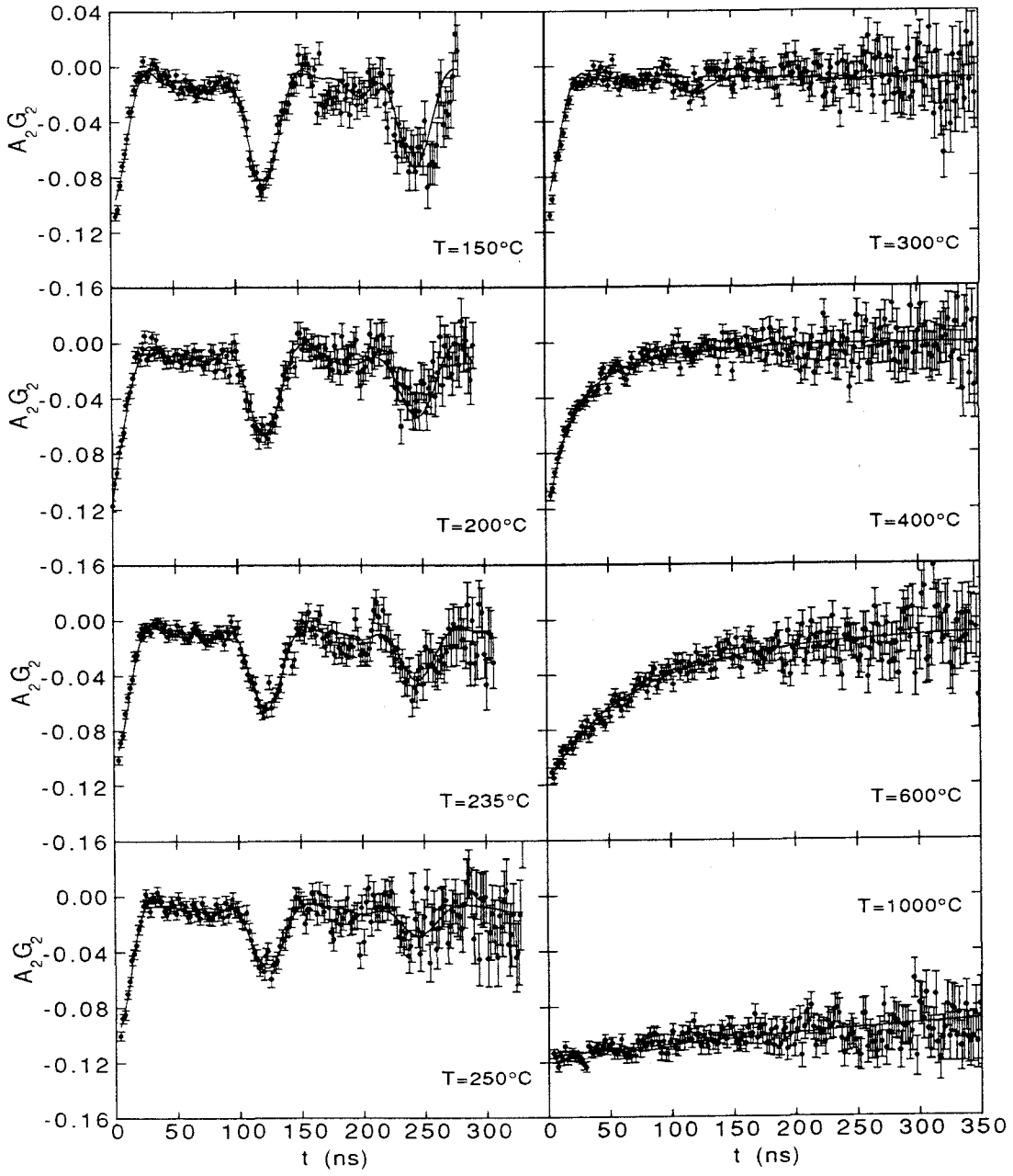

Fig. 4.6 Spectra of 0.2% Y-doped ceria at elevated temperatures.

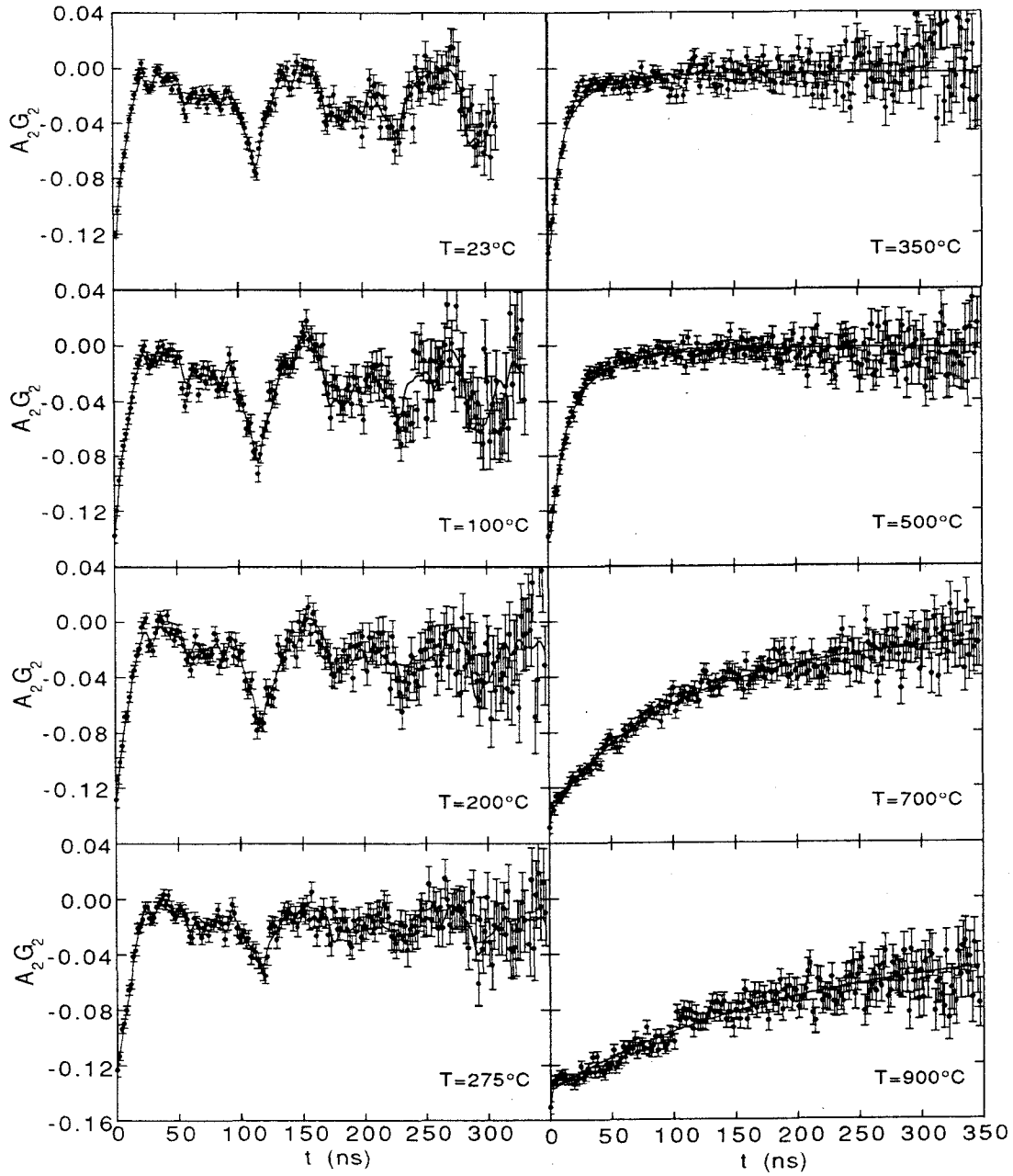

Fig. 4.7 Spectra of 0.8%Y-doped ceria at elevated temperatures.

For x=0.2% Y-doped ceria, the spectra look very much like undoped ceria. But when we fit the spectra with an XYZ site and an X site, the frequencies of the low temperature XYZ site fit to a higher value than undoped ceria, and the fit is not very good. From the Fourier transform of the PAC spectra, it looks like there might be another site next to the A site we saw before. But it is hard to say for sure and to determine the frequencies and site fraction at this point. For x=0.8% Y-doped ceria, we find another two sites (B and C). The B site is an asymmetric site, whose frequency is close to that of the A site. The C site is another axially symmetric site, whose frequency is about four times larger than that of the A site. Until we discovered the B site in 0.8%Y doped ceria, we realized the problems we have in fitting the 0.2%Y doped ceria is caused by the presence of a small fraction of the B site. Fig. 4.8 shows the room temperature PAC spectra and their FFT of Y-doped ceria at different doping levels. All Y doped ceria samples look light beige color, similar to that of undoped ceria.

Besides trivalent doping, there is another way to introduce oxygen vacancies. We could pump on the sample at high temperatures. We can understand the physics of this from the mass action law and the charge neutrality condition. Assume we have doubly charged oxygen vacancies

$$2O_O \Leftrightarrow O_2 + 2V_O^{\cdot\cdot} + 4[e^-] \qquad (4\text{-}1)$$

$$2n_V = n_e \qquad \text{(charge neutrality condition)} \qquad (4\text{-}2)$$

Applying the mass action law to eq.(4-1) results in

$$[n_e]^4 [n_V]^2 p_{O_2} = K(T), \qquad (4\text{-}3)$$

where $[n_V]$ and $[n_e]$ are the densities of oxygen vacancies and electrons respectively. Using the charge neutrality condition (4-2), we find

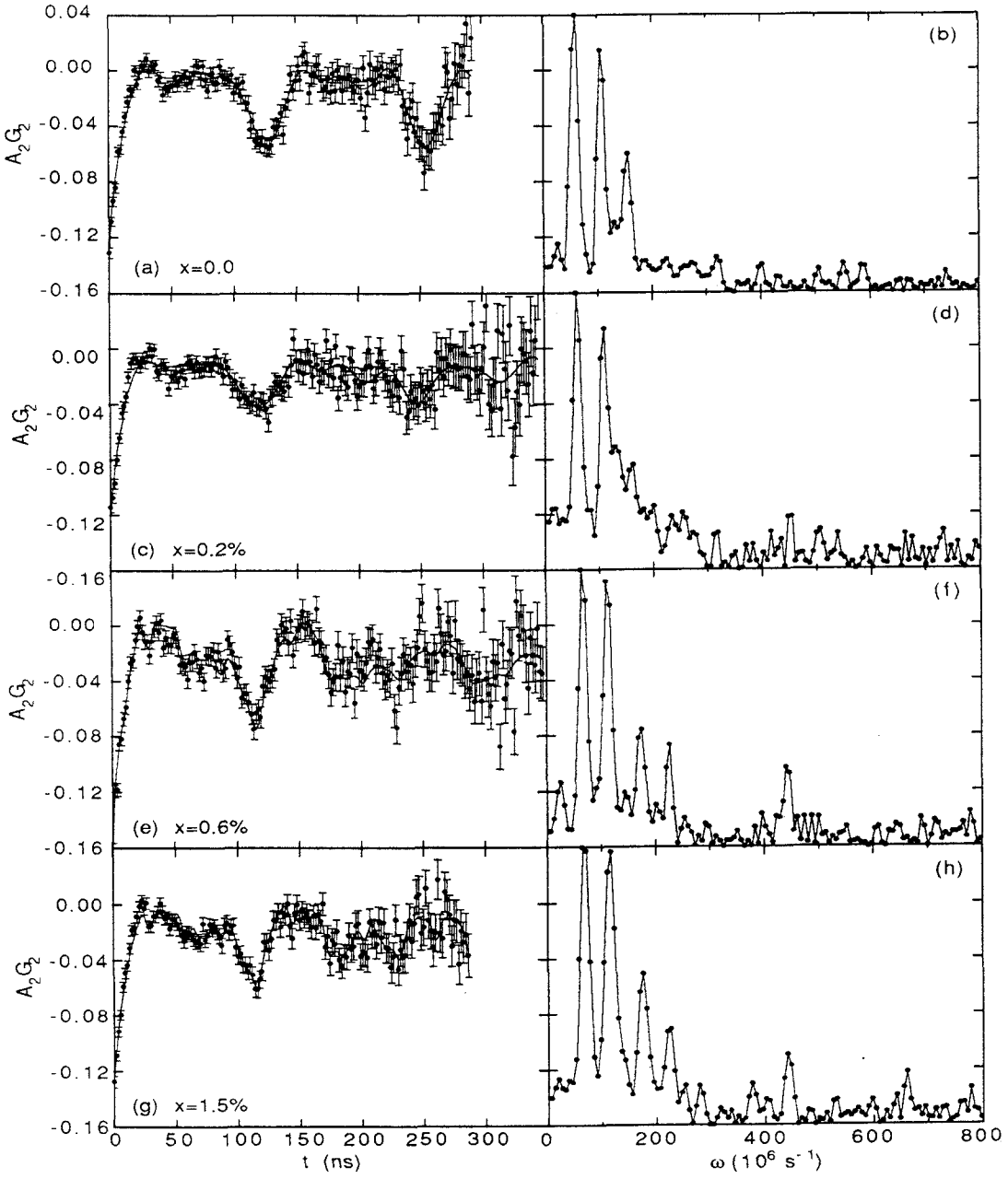

Fig. 4.8 Room temperature spectra and FFT of Y-doped ceria ($Ce_{1-x}Y_x$).

$$[n_V] \propto K(T) p_{O_2}^{-1/6} \qquad (4\text{-}4)$$

The above discussion tells us that the smaller the partial oxygen pressure is, the more oxygen vacancies there will be. So, by controlling the pumping temperature and vacuum, we could, in principle, control the oxygen vacancy concentration.

We have observed the B and C sites when we introduce more oxygen vacancies by doping ceria with Y. If these two sites are related with oxygen vacancies, we should expect to see them also in pumped ceria.

We started with a sample pumped at 1000°C for 4 hours at pressure 30 mtorr. The sample and other pumped samples were made by the following procedures: after synthesis in the usual manner, the sample was poured into a quartz tube and then placed in the PAC furnace. We raised the furnace temperature and pumped on the sample. After pumping, we sealed the quartz tube while the sample was held at temperature, in this case, 1000° C. We then cooled the sample slowly and took PAC measurements. Fig. 4.9 shows spectra from this sample at elevated temperatures. We found the same sites (A, B, C, X) in the 1000°C pumped ceria sample as we do in Y-doped ceria samples except the relative fraction of each site is different.

Several samples were made to repeat this experiment, and we got similar results. Then we made PAC measurements on samples pumped at 1100°C and 1200°C at a pressure of about 30 mtorr for over 30 min. We obtained spectra similar to those for the 1000°C pumped sample. We also made PAC measurements on a sample pumped at 900°C for about 30 min, and we found a smaller fraction of the C site. The C site does not exist in

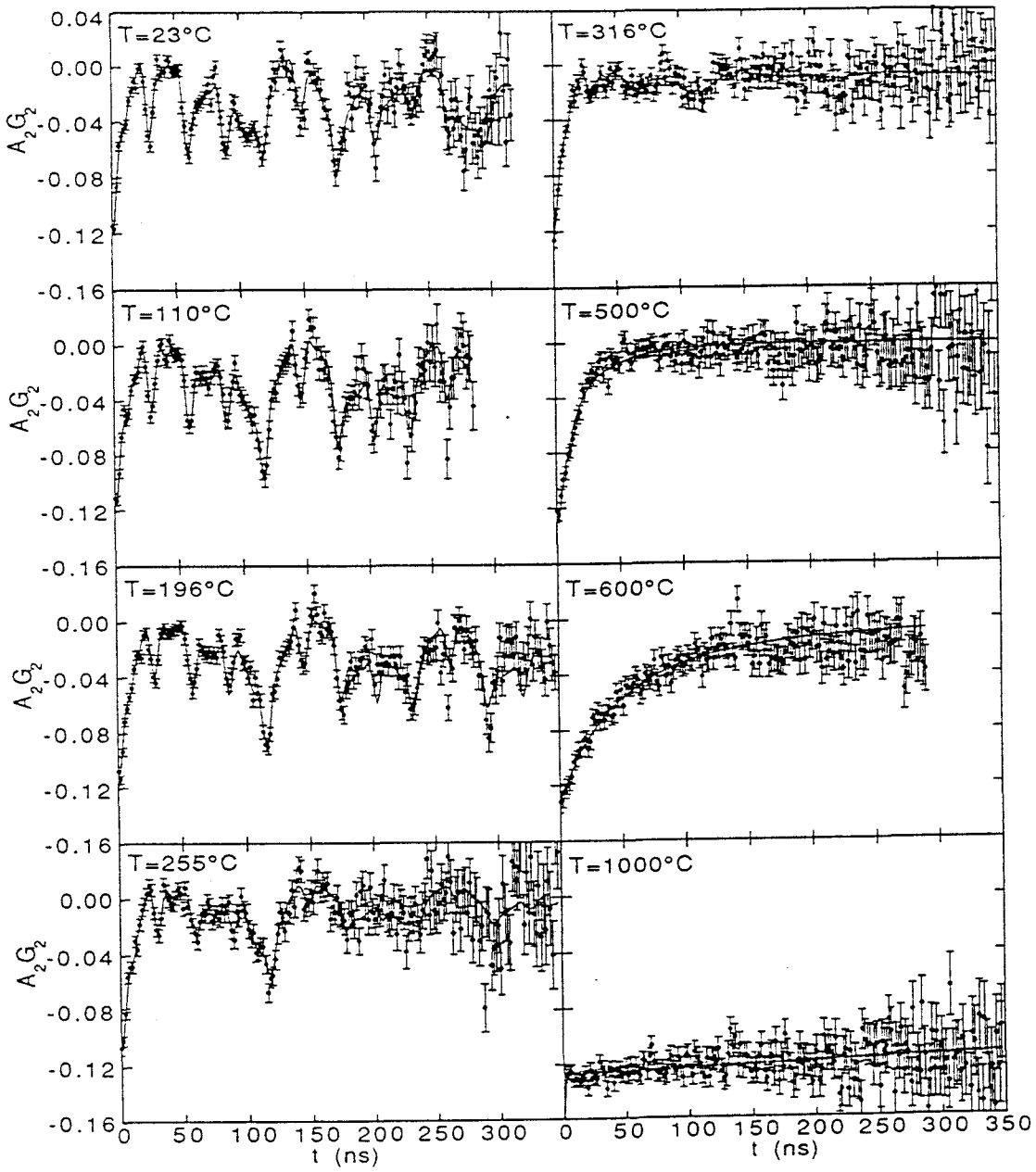

Fig. 4.9 Spectra of pumped (1000℃) ceria at elevated temperatures.

the spectra of a 800℃ pumped ceria sample. Fig. 4.10 shows the FFT of ceria samples that pumped at different temperatures. For pumping at 800℃, the sample shows silver color. For pumping at 900℃ or above the samples look light blue. The higher the pumping temperature, the darker the sample looks.

Besides the A and X sites we saw in undoped ceria, we have seen another two sites in Y-doped and pumped ceria samples. Since both Y-doping and pumping increase oxygen vacancy concentration, we think the B and C sites are caused by the oxygen vacancies introduced.

For all the Y-doped samples, the C site fraction was never as great as the pumped samples. In both cases, the C site seemed to saturate at some point, Y-doped samples at x=0.6% doping and pumped samples at 1000℃ pumping, but they did not saturate to the same fraction. Pumped samples saturated to a larger fraction.

4.4 Nb-doped ceria results

In previous sections, we have described the experiments on undoped, Y-doped and pumped ceria, which have oxygen deficiencies. What would happen if we remove these oxygen vacancies? Similar to the idea of Y-doping experiments, we could pentavalent-doping ceria, e.g. with Nb_2O_5. If we dope ceria with Nb_2O_5, and Nb^{+5} substitutes for Ce^{+4}, the cerium site will end up with a net charge +1 relative to the neutral lattice. A decreasing oxygen vacancy concentration is necessary to compensate for this charge. One doubly charged oxygen vacancy will be compensated for every two Nb^{+5} doped. The ionic size of Nb^{+5} is 0.69[3].

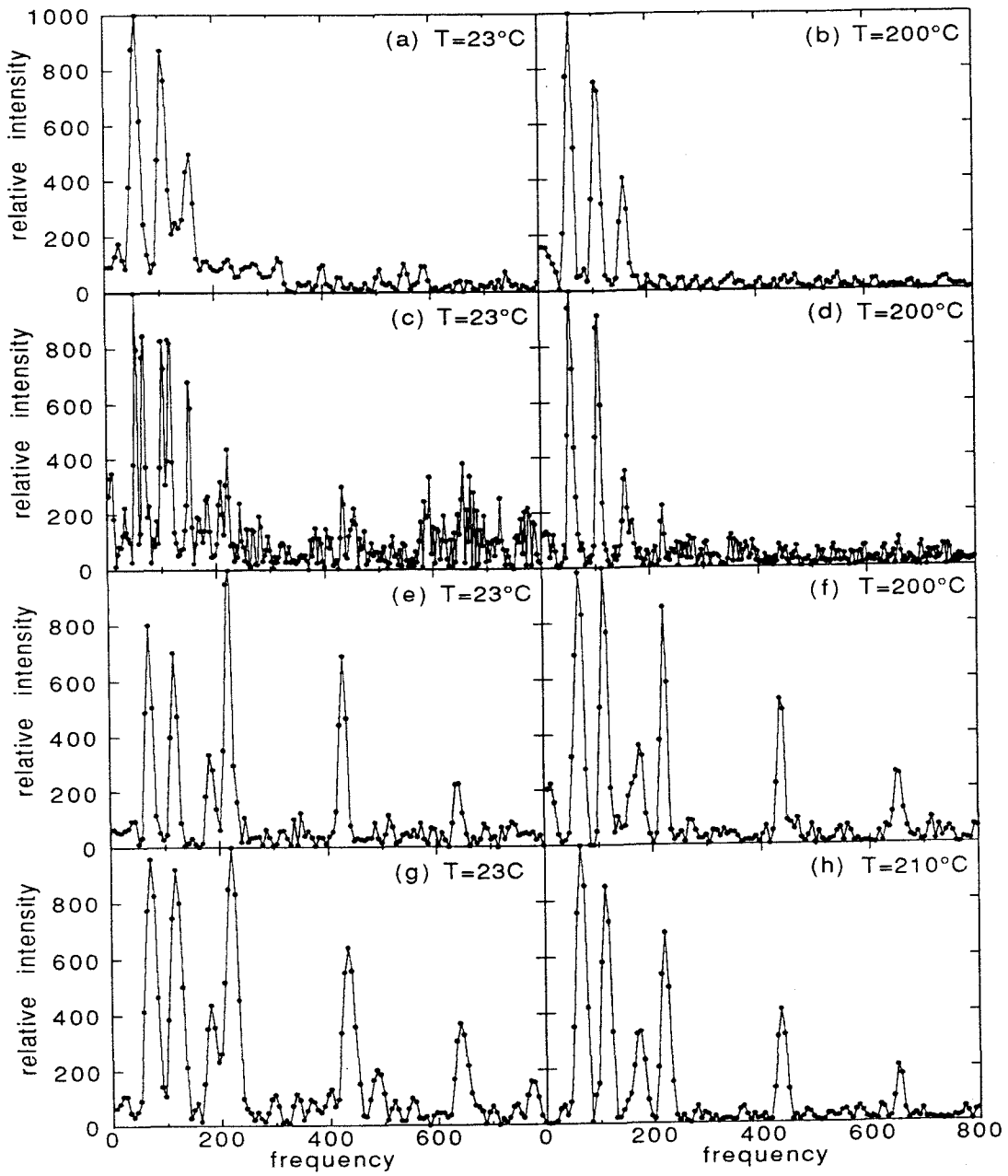

Fig. 4.10 FFT of ceria (a, b), 900℃ pumped ceria (c, d), 1000℃ pumped ceria (e, f) and 1200℃ pumped ceria (g, h).

If the A site in undoped ceria is caused by an oxygen vacancy, then by doping enough Nb, we should see this site disappear. By pumping on this Nb-doped sample, we hope to see the A, B and C sites appearing also in Nb-doped samples due to oxygen vacancies.

Figs. 4.11 and 4.12 show room temperature and about 200°C Nb-doped spectra at different Nb-doping levels. Fig. 4.13 shows the spectra of a 500 ppm Nb-doped ceria sample at elevated temperatures. The synthesized samples look grey or light blue for samples with 500 ppm or more Nb-doping.

Below y=300 ppm ($Ce_{1-y}Nb_y$), the spectra look more or less the same as for undoped ceria. The spectra changed completely to an X site, a cubic site, and a small fraction of a static asymmetric site (D site) in the range y=300-350 ppm. Above y=350 ppm Nb doping, the spectra continue to have these three sites. The fraction of the D site decreases with increased temperature or Nb doping.

We also performed some very interesting pumping experiments on Nb-doped ceria samples (Fig.4.14). For a 500 ppm Nb-doped sample, we first took a PAC spectrum at about 200°C (a). The spectrum is similar to that in Fig. 4.13. Then we pump on the sample at 800°C to about 30mtorr, and slowly cool the sample in vacuum to 200°C and took another PAC spectrum (b). We further took another PAC spectrum at 400°C (c). Now we can see the fraction of the D site is smaller than that in (a). We heated the sample up to about 1000°C, pumped for about half an hour and then cooled the sample to room temperature in the PAC furnace while still pumping on the sample. Then the 200°C spectrum (d) looked like that of undoped ceria, which has mainly A site. When we pumped at about

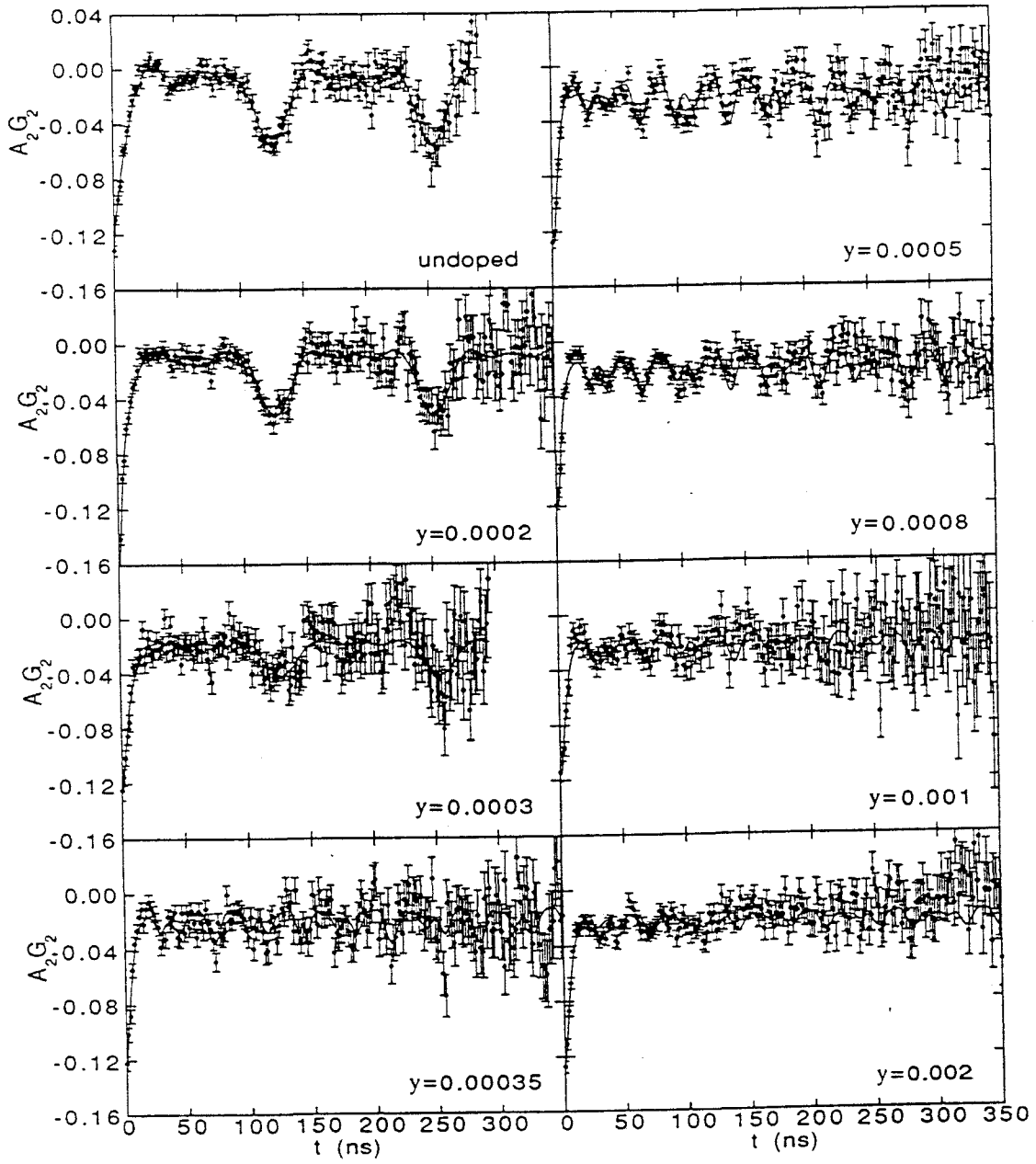

Fig. 4.11 Room temperature spectra of Nb-doped ceria ($Ce_{1-y}Nb_y$).

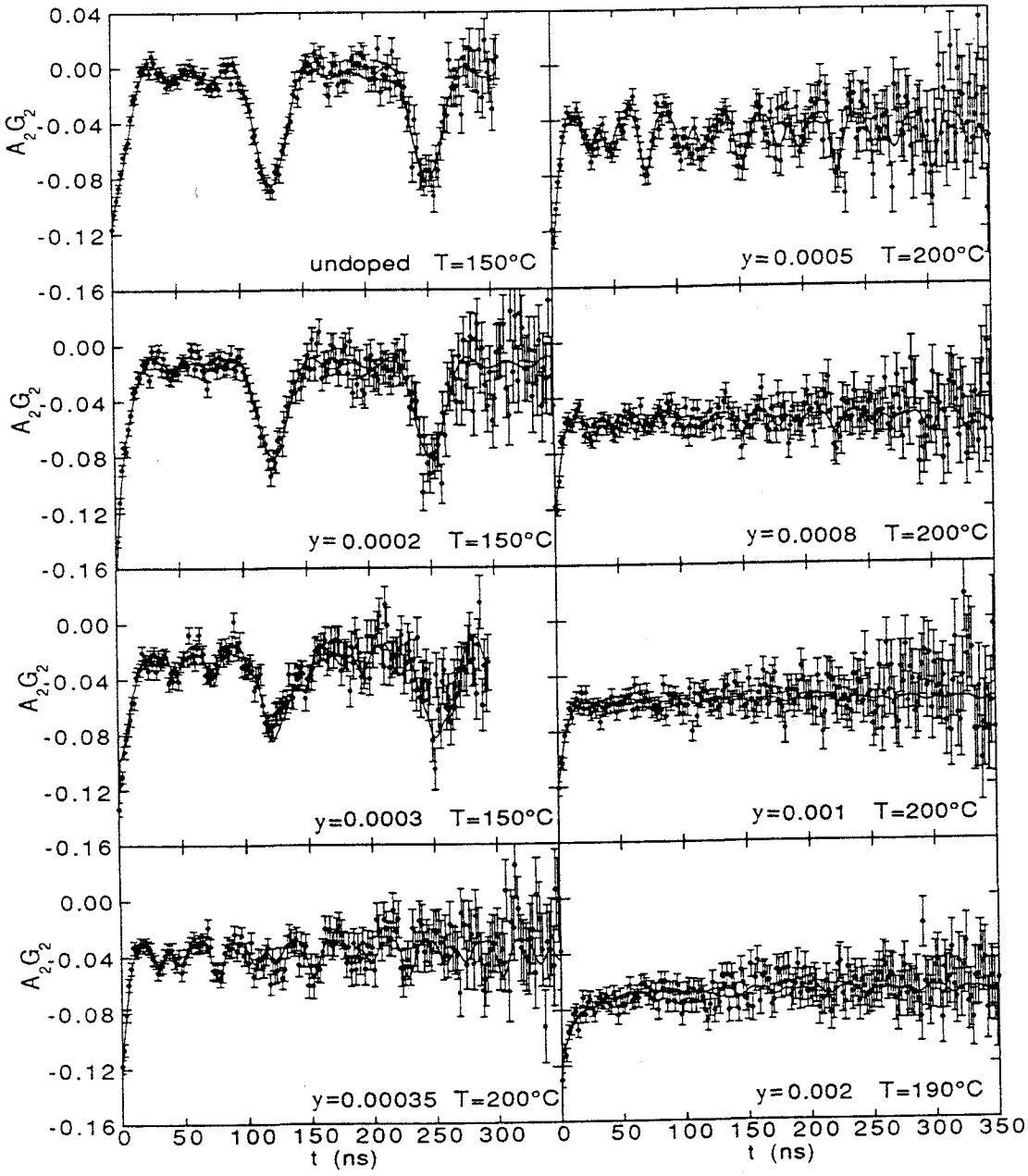

Fig. 4.12 Spectra of Nb-doped ceria ($Ce_{1-y}Nb_y$) at about 200°C.

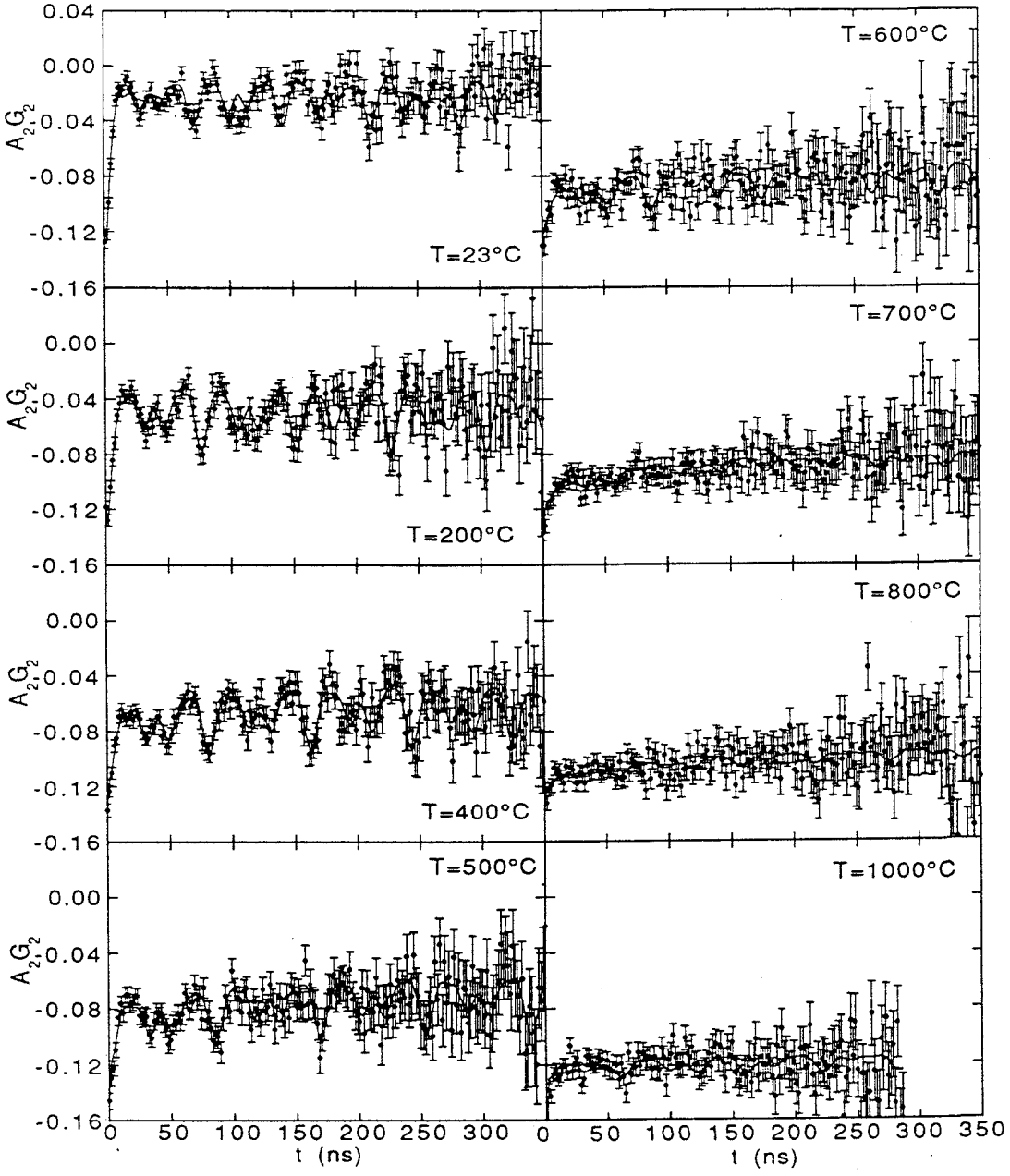

Fig. 4.13 Spectra of 0.05%Nb-doped ceria at elevated temperatures.

1100℃, we obtained spectrum, at room temperature (c), similar to 1000℃ pumped undoped ceria, with A, B, C, and X sites. If we exposed the sample to air at room temperature, the spectra for 200℃ or below was the same as those before exposure to air. But at 300℃, the spectra changed to that shown in Fig.4.13. This indicates that oxygen in air can diffuse into the sample at about 300℃.

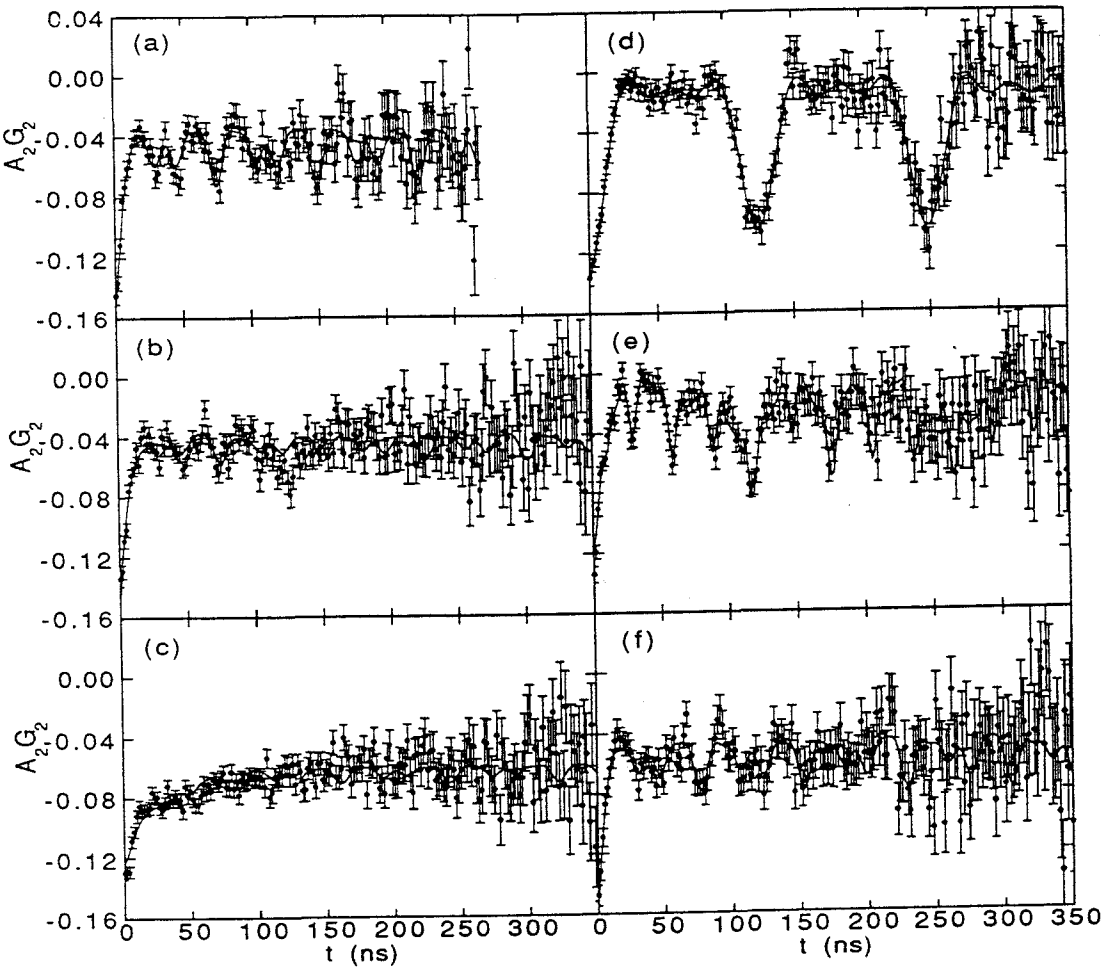

Fig. 4.14 Spectra of 0.05%Nb-doped ceria pumped at elevated temperatures.

These experiments tell us again that the A, B, C sites are related to the oxygen content. We only see the D site in Nb-doped ceria samples. It appears from y=350 ppm above; its fraction ranges from 5-25% of the site fraction. The site fraction becomes smaller at higher doping levels or higher temperatures, and it can persist to as a high temperature as 700°C. This D site might not be directly related to Nb-doping, since its fraction decreases when we increase doping.

In the literature, it has been shown that hydrogen can incorporate into bulk ceria. This could be a possible cause for the D site. Since the D site always has a small fraction, its fraction does not seem to be very systematic. When we pumped on the sample we could decrease the site fraction and when we exposed the sample to air at high enough temperature this site reappeared. In order to investigate the possibility of hydrogen or hydroxyl ion in Nb-doped ceria, we made the following two experiments.

One was an attempt to increase the water vapor near the sample by blowing steam onto the sample at T>100°C. If we could see any D site fraction change, we would have evidence for the hydroxyl ion incorporation idea. But no change was observed. This was not a very neat experiment; we are not sure exactly how much water vapor we actually applied to the sample. Nevertheless we applied more water vapor to the sample than if it had been done in air.

The second experiment was to run a 500 ppm Nb-doped sample at room temperature. We pumped the sample at about 800°C, and cooled it to 200°C and found that we lost about half of the D site. This sample was further raised to 1000°C, and we flowed only oxygen (not air!) over the

sample, then cooled to 200℃ and took a PAC measurement. We found the D site restored its original fraction. Therefore this site is not due to hydrogen in air or water vapor. It still seems to have something to do with oxygen content and Nb-doping.

4.5 Other results on ceria

We also made PAC measurements on In-doped (trivalent doping) ceria in addition to Y-doped ceria. Since we use ^{111}In as our nuclear probe, the nuclear probe should have the same physical environment as the doped indium. In this case, the nuclear probe "sees" the environment of doped impurities. This is unlike the case of Y-doped ceria in which the nuclear probe and the Y might have different environment.

Indium has a high vapor pressure. It is likely that the sample lose some indium during synthesis at high temperatures. We keep track of indium loss by keeping track of radioactive indium loss. We found we lost about 60% or 5% of indium if we synthesized the sample at 1550℃ or 1200℃ respectively.

We made PAC measurements on 0.2% In and 1% In-doped ceria samples. The spectra are the same as those of undoped ceria. We did not find the B and C sites even for 1% In-doped ceria synthesized at 1200℃. Fig. 4.15 shows the PAC spectra of undoped ((a), (b)), 1% In-doped ((c), (d)) and 0.8% Y-doped ((e), (f)) ceria.

For Nb-doped ceria, we saw the D site. We also made PAC measurements on a 500 ppm Ta-doped ceria sample. The Ta doping process is difficult. The solution is only stable for a day or so before it

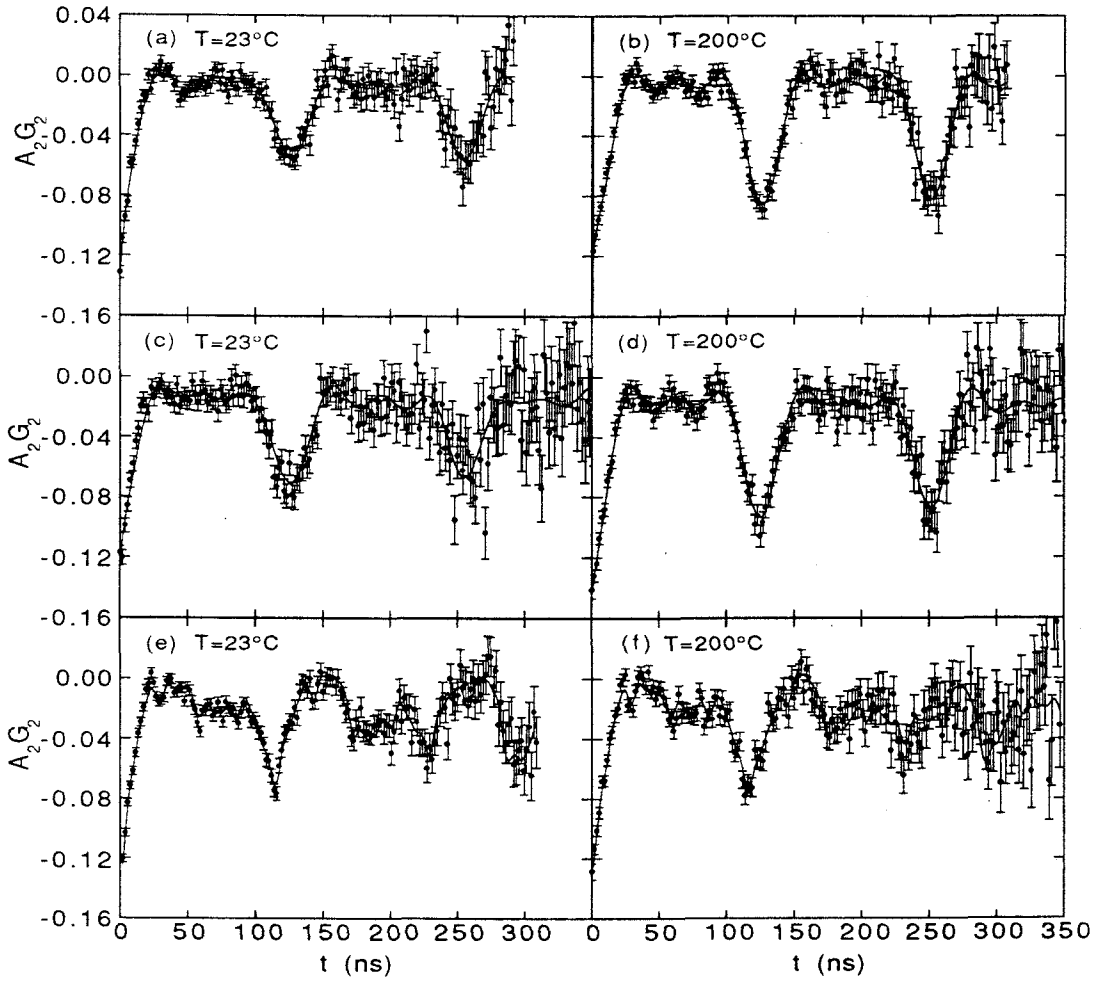

Fig. 4.15 Spectra of undoped(a,b), 1%In-doped (c,d) and 0.8%Y-doped (e,f) ceria.

precipates. The spectra look similar to those of Nb-doped ceria, except that the fraction of the D site is only about 5-10%. Because of its small fraction, this static site frequency cannot be determined very precisely. Even though this static site can be fitted well with the D site frequency of Nb-doped ceria, there still is a small possibility that they might be different. With the present information, we speculate they are the same

site, the D site. Fig. 4. 16 shows the spectra of 500 ppm Ta-doped ((a), (b)) and 500 ppm Nb-doped ((c), (d)) ceria.

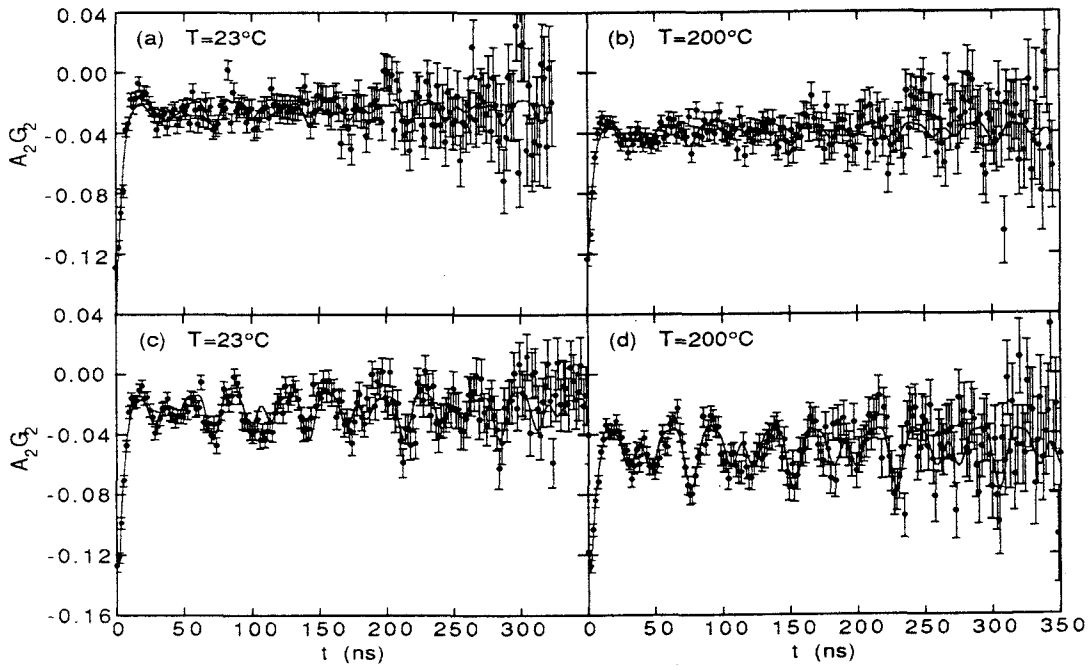

Fig. 4.16 Spectra of 0.05%Ta-doped (a,b) and 0.05%Nb-doped (c,d) ceria.

So far, all the experiments we have discussed are performed at room temperature or above. What would happen at low temperatures? Because of the restriction of the experimental equipment, we only made low temperature measurements at 77K. Fig. 4.17 shows the spectra of undoped ((a), (b)), pumped undoped (1000℃) ((c), (d)) and 500 ppm Nb-doped ((e), (f)) ceria at room temperature and 77K. For undoped ceria, the spectrum at 77K is essentially the same as the spectrum at 23℃. For the pumped (at 1000℃) ceria sample, the 77K spectrum has a larger C site fraction than that at room temperature. The 500 ppm Nb-doped ceria

sample has static D site at room temperature, but this D site disappears at low temperature!. Professor Robert Rasera (Department of Physics, University of Maryland, Baltimore County, Catonsville) made PAC measurements of a 500 ppm Nb-doped ceria sample for us at 10K and 176K. The spectra are essentially the same as that at 77K.

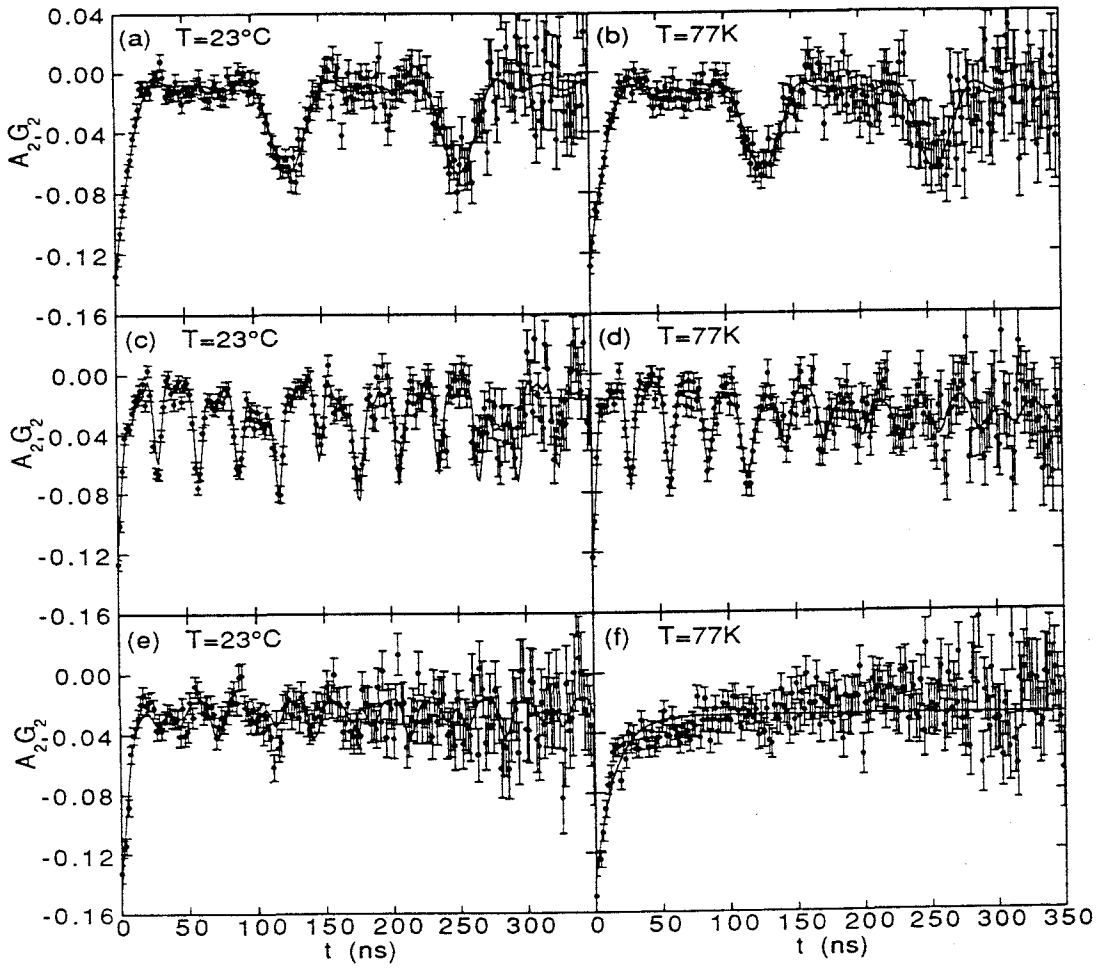

Fig. 4.17 Spectra of undoped(a,b), pumped undoped (c,d) and 500 ppm Nb-doped (e,f) ceria at 77K.

5. Analysis of the experimental results

A good experiment depends not only on good physical ideas and good equipment design, but also on good method to extract physical quantities from experimental data. Here we present in detail how we analyzed our ceria PAC data. There are some ambiguities in fitting these data since an equally good fit may be obtained under different physical assumptions. So it is very important to show the details of the fitting process before giving any explanations and making any conclusions.

In the final analysis, we have used the following models for fitting our data:

(1) static model:

$$G_2(t) = S_{20} + \sum_{n=1}^{3} S_{2n} \cos(\omega_n(\eta)t) \quad , \tag{5-1}$$

where S_{2n} are the same as in (2-58)-(2-61).

This is a perturbation to the angular correlation function caused by the static electric quadrupole interaction. This model fits the C and D sites.

(2) XYZ model:

This model describes a fluctuating efg field about a nuclear probe among different orientations. From Professor William Evenson's numerical calculation, we take the following expressions for the two limiting cases:

for small fluctuating rate w (XYZ(low)):

$$G_2(t) = S_{20}\exp(-\lambda_0 t) + S_{21}\exp(-\lambda_1 t)\cos(\omega_1 t) + S_{22}\exp(-\lambda_2 t)\cos(\omega_2 t) + S_{23}\exp(-\lambda_3 t)\cos(\omega_3 t) \quad , \tag{5-2}$$

where the S_{2n} and λ can be found in (2-58)-(2-61) and (2-69).

for large fluctuating rate w (XYZ(high)):

$$G_2(t) = 0.5714 \times \exp(-\lambda_0 t) + 0.3032 \times \exp(-\lambda_1 t) + 0.0968 \times \exp(-\lambda_2 t) + 0.0286 \times \exp(-\lambda_3 t), \quad (5\text{-}3)$$

where λ can be found in (2-70)

this XYZ model is used to fit the A and B sites.

(3) exponential model:

$$G_{22}(t) = \exp(-\lambda t), \quad (5\text{-}4)$$

This model is used for the X site. It generally describes a relaxation process[44].This function provides an adequate heuristic fit, although there is no physical basis for it.

(4) cubic model:

$$G_{22}(t)=1. \quad (5\text{-}5)$$

This is the case where the nuclear probe sits in a symmetric environment, i.e. no electric quadrupole perturbation at the probe site. This model can be used for a simple substitutional nuclear probe on cerium site.

A superposition of the above models is used to fit the data:

$$G_2(t) = \sum_i f_i (G_2(t))_i, \quad (5\text{-}6)$$

where f_i is the fraction of the ith site.

5.1 Undoped ceria

We found the A site and the X site in undoped (~300 ppm impurities) and high purity ceria (<20 ppm impurities). The PAC spectra are essentially the same in both cases. We used the stochastic XYZ model to fit the A site and an exponential function to fit the X site (Fit I). In order to get a better fit, a small fraction of a cubic site (5~10%) is needed for the low temperature region (<300°C) (Fit II) or for the entire temperature range, fixing the cubic site fraction to 6% (Fit III). (An equally good fit can be achieved with or without this cubic site at high temperatures (>300°C), resulting in a slightly different lambda values). The reason for fixing the cubic site in the latter case is that the cubic site tends to include some of the XYZ site at high temperatures where lambda is small.

In the fitting process, we used five sets of ceria data, from five different samples at elevated temperatures, as an ensemble to fit all the parameters that we will show below. This ensemble includes 136 spectra. To estimate the systematic error, both "normal" and "reverse" spectra (see **3.1** and **3.4**) are used in the ensemble. We have used three different methods (Fit I, II, III) to fit this ensemble. In Fit I, we used only the A site and the X site. In Fit II, we used the A site, the X site and a small fraction of the cubic site at temperatures below 300°C. In Fit III, we used the A site, the X site and a fixed fraction (6%) of cubic site, which we obtained by averaging the cubic fraction in Fit II at T<300°C. We think the small fraction of the cubic site is an experimental artifact. For example, internal absorption will cause 180° pair to have less counts than the 90° pair[57] which causes the spectrum to shift by a small constant, i.e. "add" a small "cubic site". We show the results both from all three fits

and from Fit III only with statistical errors. Our conclusions for ceria are based on Fit III.

Fig. 5.1-5.2 show the χ^2 of the least-squares fits at elevated temperatures. Fig. 5.3-5.4, Fig. 5.5-5.6 and Fig. 5.7-5.8 show the PAC frequencies, the fractions of the A and X sites at elevated temperatures respectively. The A site at low temperature (<200℃) is an axially symmetric site.with ω_1=50.0(2) Mrad/s. Fig. 5.9-5.10 and Fig. 5.11-5.12 show the XYZ lambda and the reorientation rate w vs. 1000/T(K). W was fitted to an Arrhenius form, with the result

$w=2.888*10^6*\exp(-7.130*1000/T(K))$ (10^6/s) (Fit I), (5-7)

$w=3.526*10^6*\exp(-7.219*1000/T(K))$ (10^6/s) (Fit II), (5-8)

$w=2.122*10^6*\exp(-6.878*1000/T(K))$ (10^6/s) (Fit III). (5-9)

From the slope of the fitted line of ln(w) vs. 1000/T(K), we find the energy barrier for the fluctuating field is 0.61 (Fit I), 0.62 (Fit II), and 0.59 eV (Fit III). We take 0.60(2) eV as the energy barrier deduced from the XYZ model. Fig. 5.13-5.14 show the damping lambda of the X site, which is about 0.2 ns^{-1}.

We have also examined the possibilities which there are 4 or 6 reorientation directions corresponding to a vacancy hopping among first or second neighbor oxygen sites, instead of 3 (XYZ directions). Fig.5.15 gives the reorientation rate w vs. 1000/T(K) assuming 3 (a), 4 (b), and 6(c) reorientation directions. These data are obtained by rescaling[48] the w from fit III. The fitted result from Fig. 5.15 (b) is

$w=7.07*10^5*\exp(-6.202*1000/T(K))$ (10^6/s), (5-10)

and the data in (c) can not be fit to an Arrhenius form. The energy barrier for case (b) is found to be 0.54(2) eV.

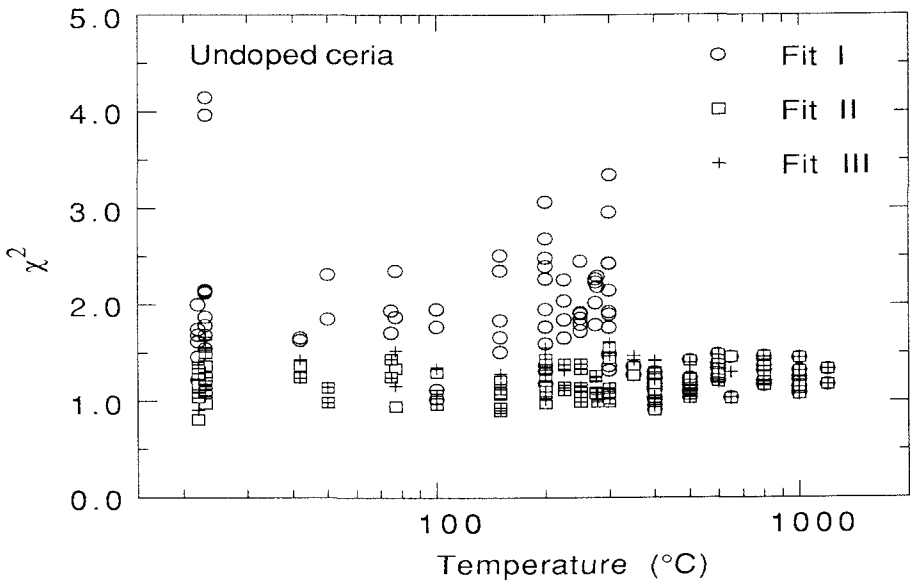

Fig. 5.1 χ^2 of the undoped ceria for Fit I, II, and III.

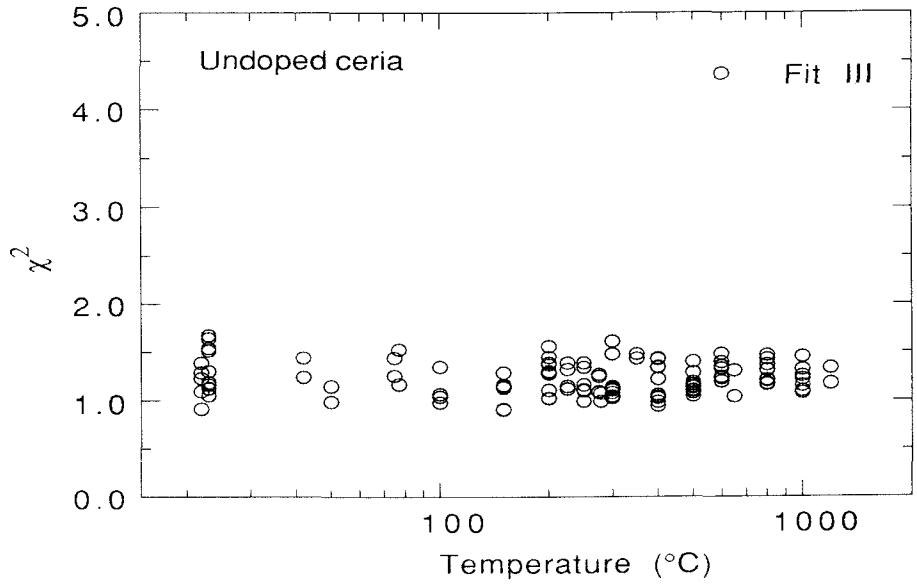

Fig. 5.2 χ^2 of the undoped ceria for Fit III.

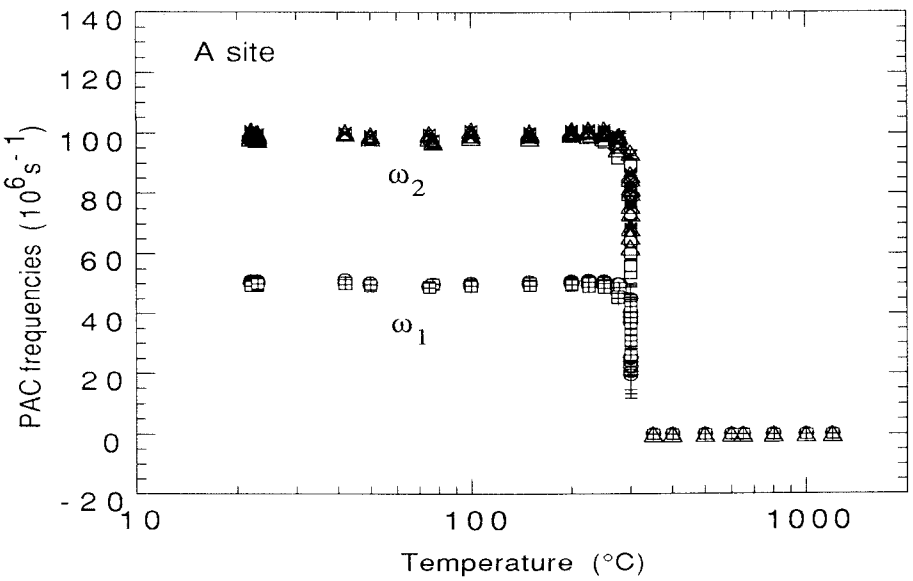

Fig. 5.3 The PAC frequencies of undoped ceria for Fit I, II, and III.

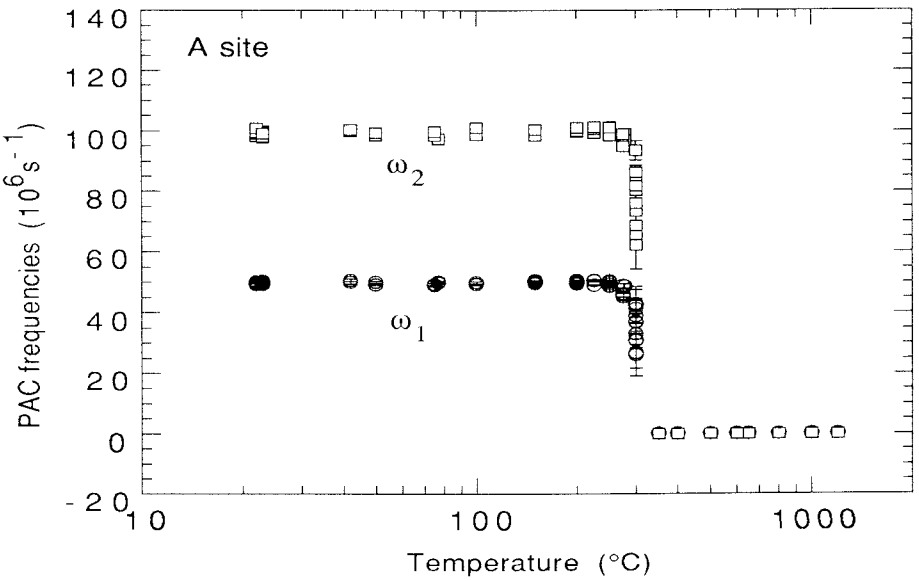

Fig. 5.4 The PAC frequencies of undoped ceria for Fit III.

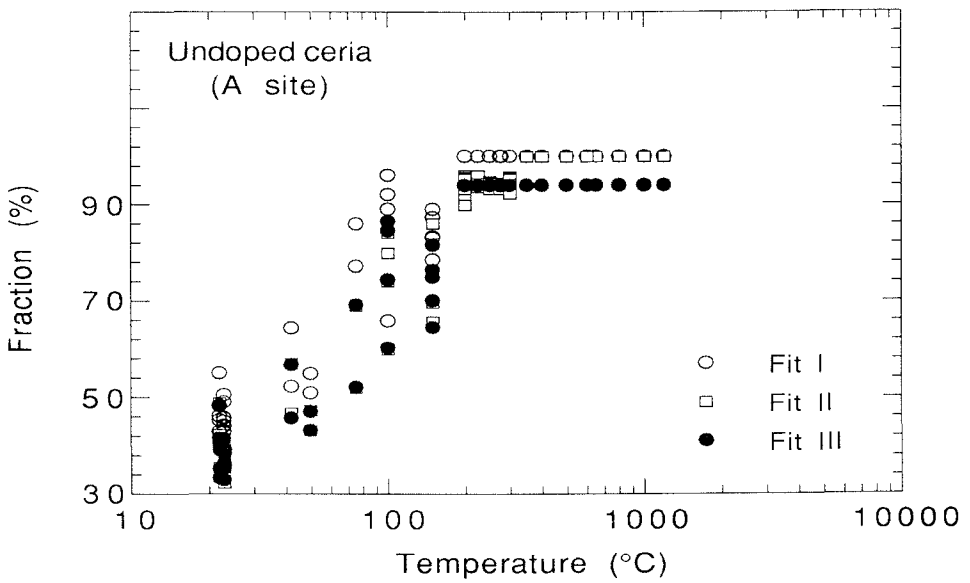

Fig. 5.5 The A site fraction of undoped ceria for Fit I, II, and III.

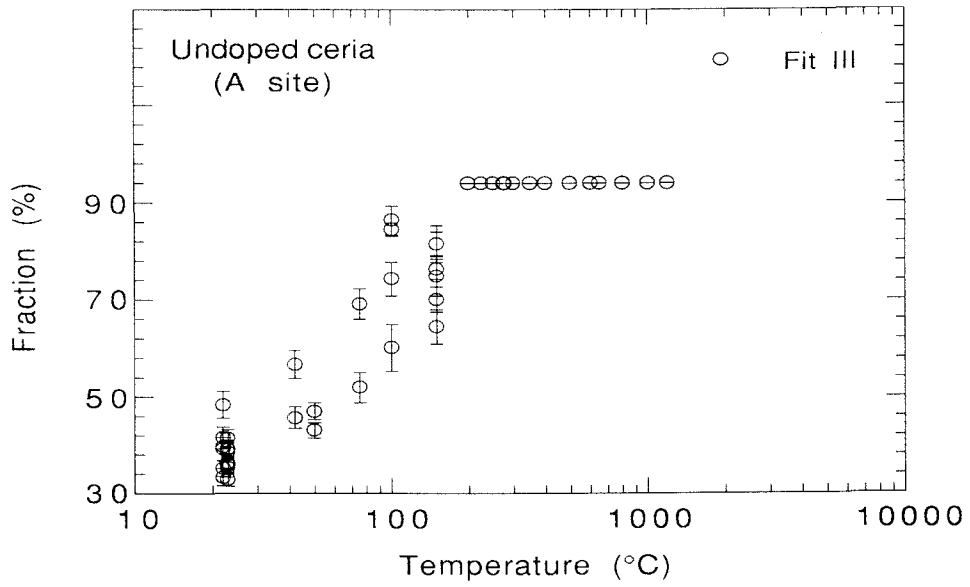

Fig. 5.6 The A site fraction of undoped ceria for Fit III.

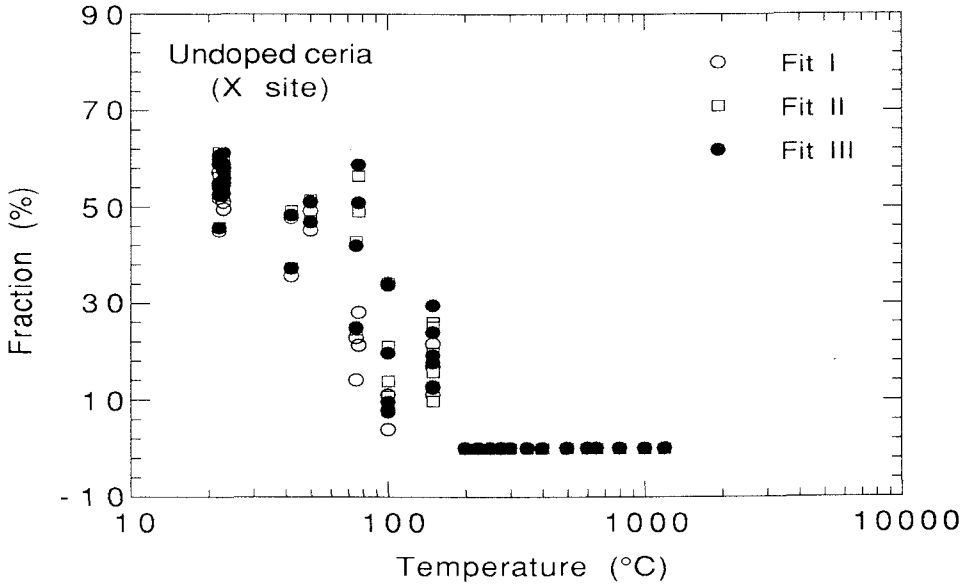

Fig. 5.7 The X site fraction of undoped ceria for Fit I, II, and III.

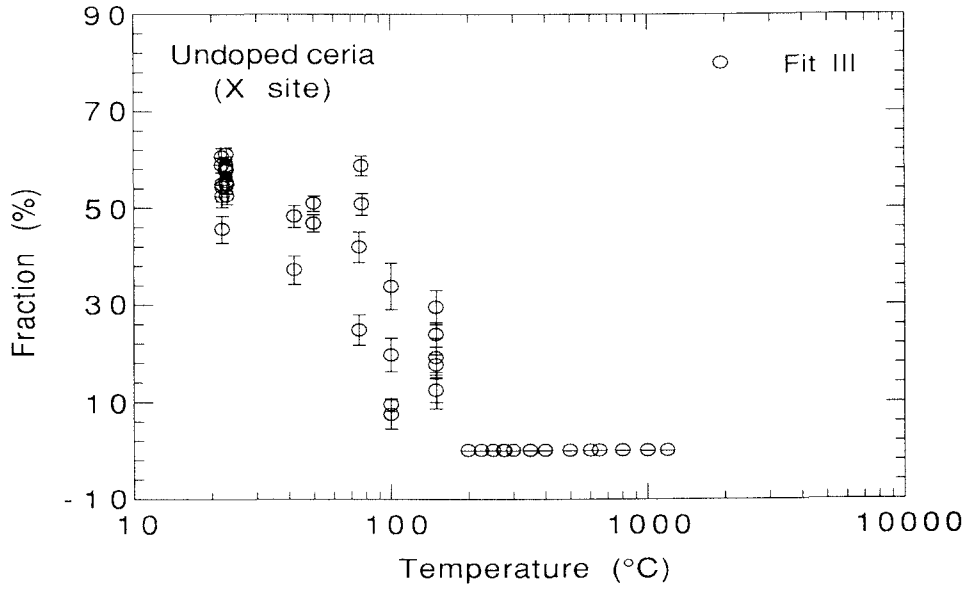

Fig. 5.8 The X site fraction of undoped ceria for Fit III.

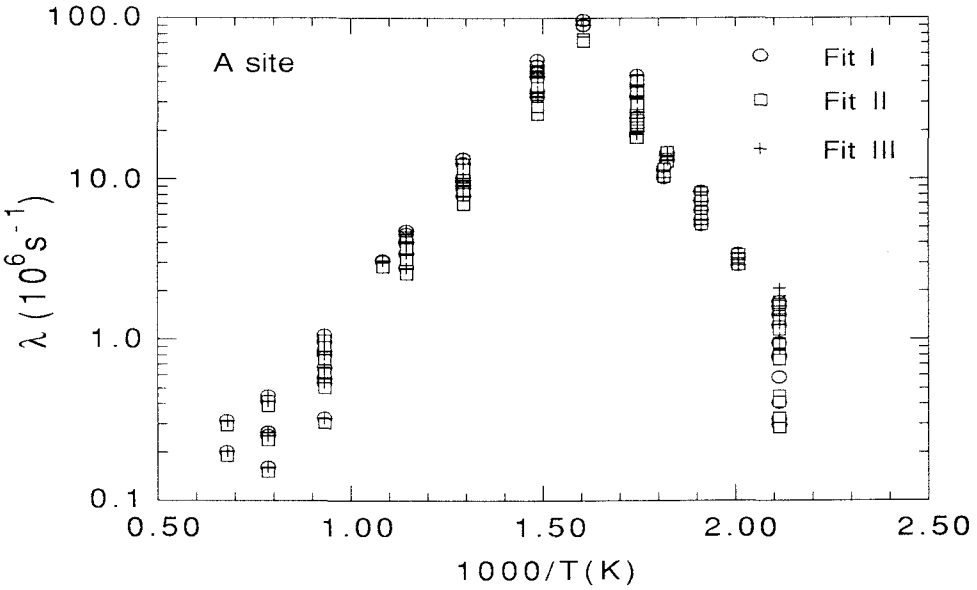

Fig. 5.9 The A site XYZ lambda of undoped ceria for Fit I, II, and III.

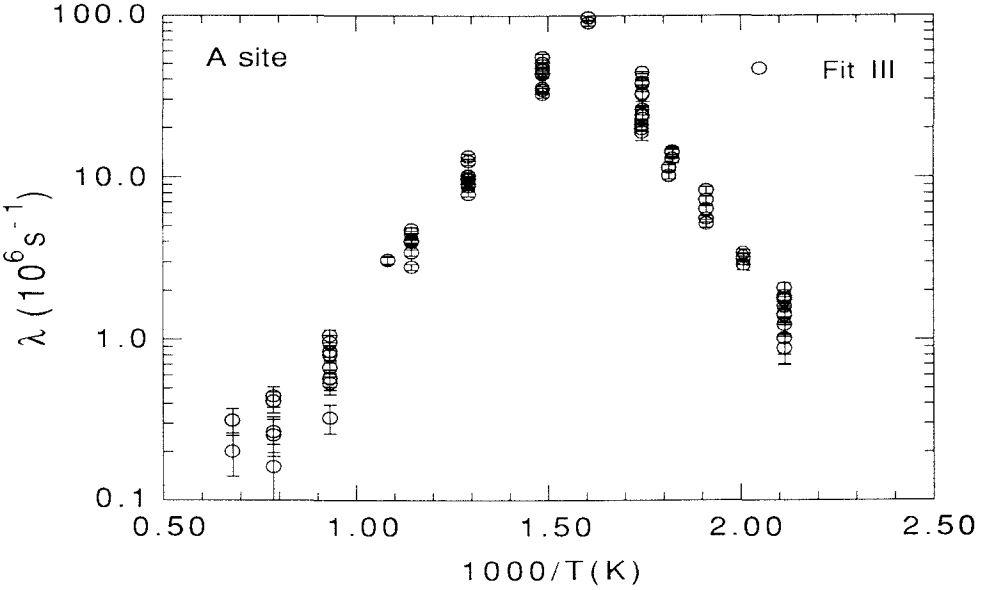

Fig. 5.10 The A site XYZ lambda of undoped ceria for Fit III.

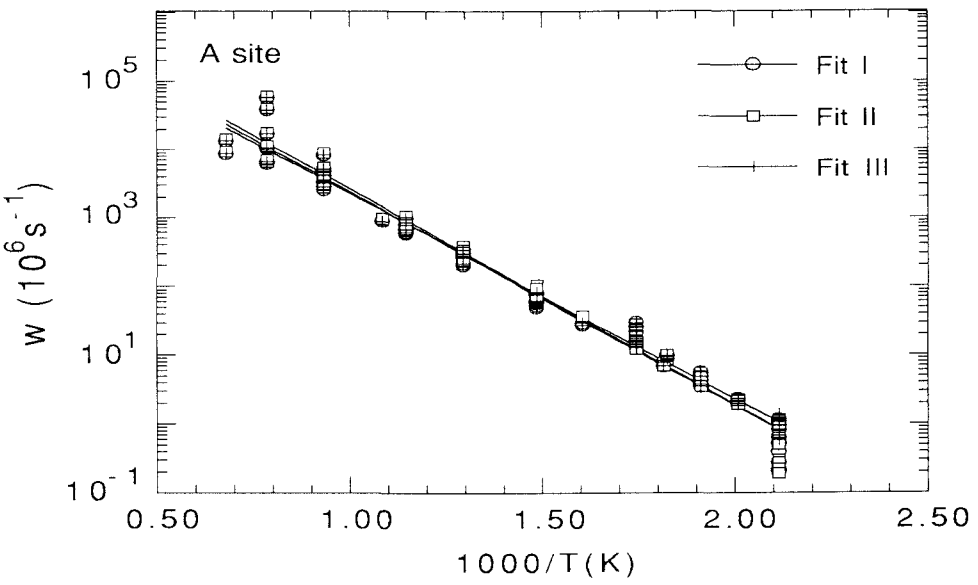

Fig. 5.11 The A site reorientation rate w of undoped ceria for Fit I, II, and III.

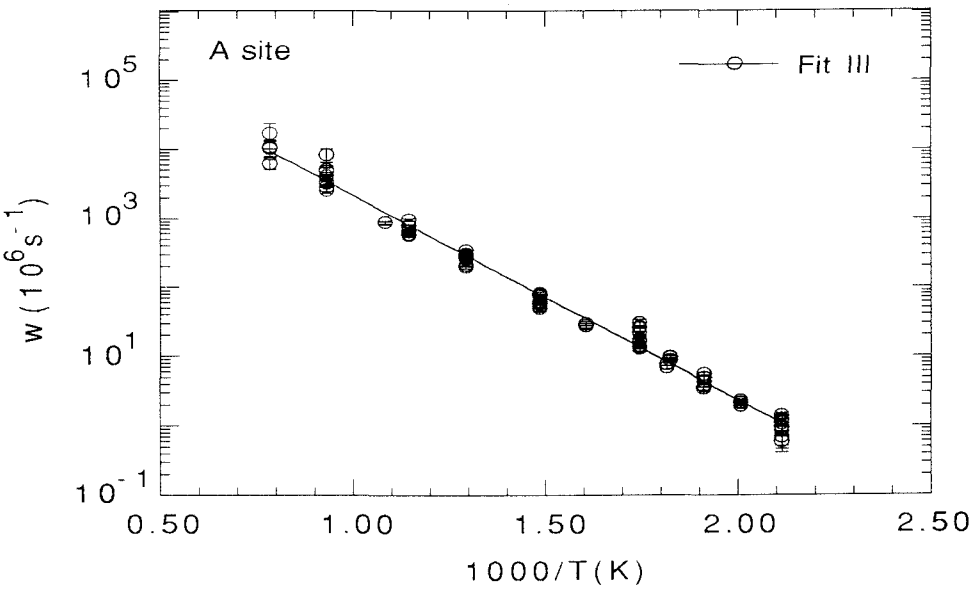

Fig. 5.12 The A site reorientation rate w of undoped ceria for Fit III.

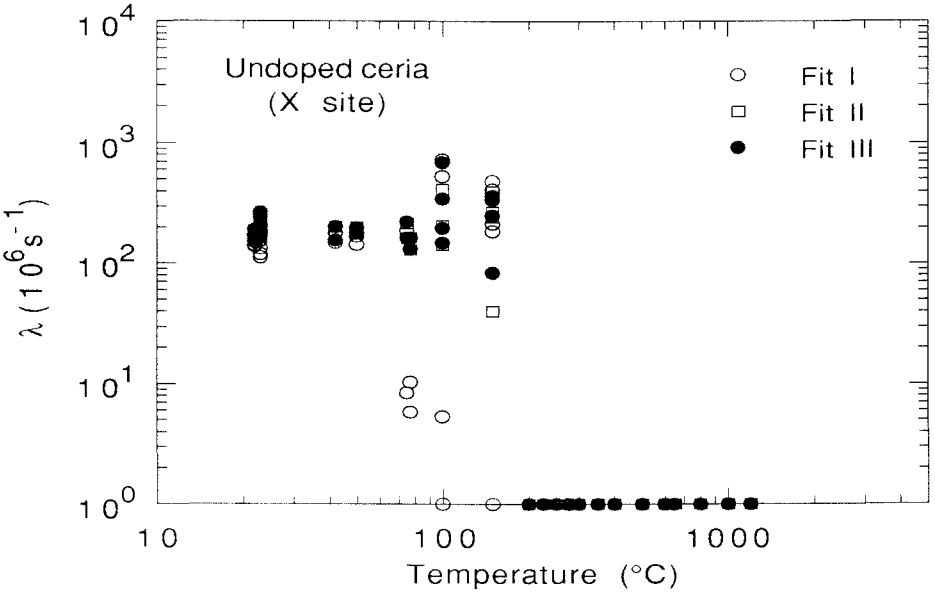

Fig. 5.13 The X site damping lambda of undoped ceria for Fit I, II, and III.

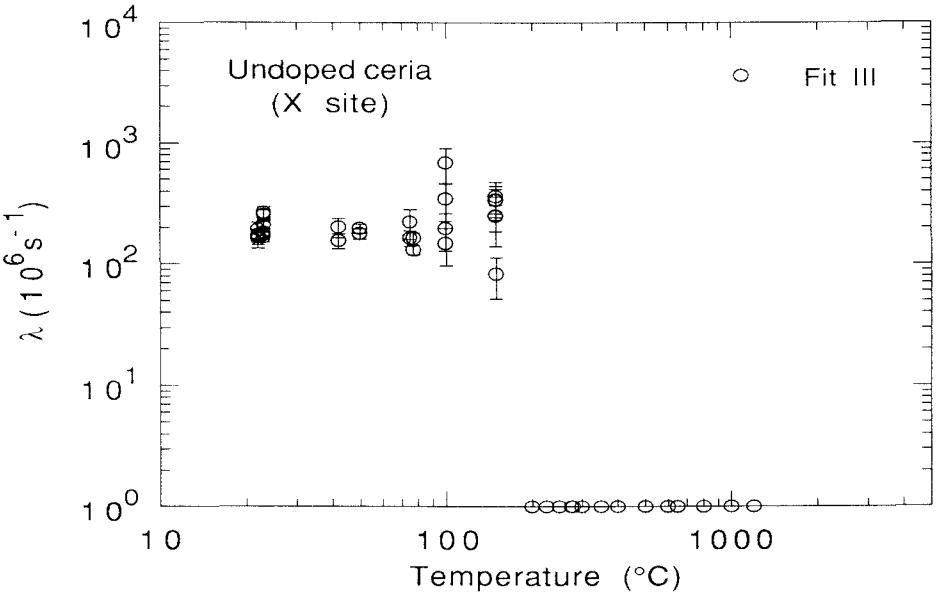

Fig. 5.14 The X site damping lambda of undoped ceria for Fit III.

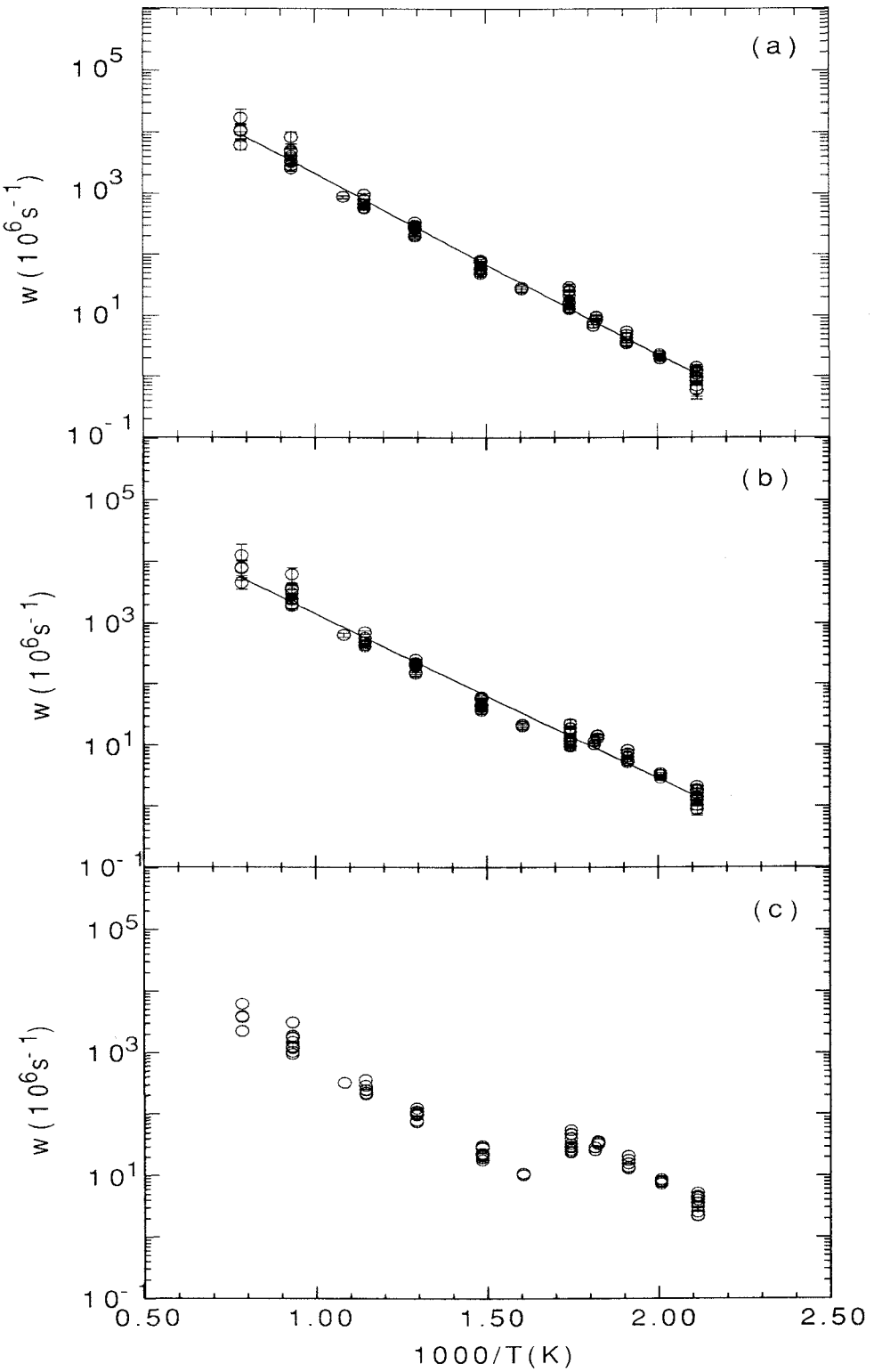

Fig. 5.15 The A site reorientation rate w of undoped ceria for different reorientation ((a) 3, (b) 4, (c) 6) directions.

5.2 Pumped and Y-doped ceria

In pumped and Y-doped ceria, we found the A, B, C, and X sites. The A, B and C sites are identified by their different frequencies at temperatures below 300°C. Above 300°C, the spectra follow the relaxation behavior. Since the pumped and the Y-doped ceria both have similar sites we made an ensemble of 150 spectra to fit the A, B, C sites.

The previous section dealt only with the A site. The presence in this case of the B and C sites makes things more complicated. It is difficult to determine which site is static and which site is XYZ like. To investigate the A, B and C sites we started with the low temperature spectra (<200°), where the XYZ damping lambda of the A site is negligible. We used three static sites and an X site to fit the ensemble. For Y-doped ceria, the B site fraction increases with temperature and the C site fraction is more or less a small constant (~10-15%). For pumped ceria, the B site fraction also increases with temperature and the C site fraction decreases with temperature. If we assume all the A, B, C sites are XYZ sites, we must know the fraction of each site in order to fit the XYZ damping lambda at high temperatures. Since all the spectra at high temperatures are relaxation like which can be fit to an exponential function or its superpositions, it is impossible for the fitting program to determine the fraction for each site. To simplify the problem, we assume the A site has the same XYZ lambda as in the undoped ceria and the C site is static since it either keeps a small fraction (in Y-doped ceria) or its fraction decreases with temperature (in pumped ceria). We fit the fraction of the B site below 200°C to a linear function and extrapolate this function to higher temperatures as fraction of

the B site and fit the XYZ lambda of the B site. The linear functions used as the fraction of the B site for each case are listed below:

0.2%Y-doped ceria: fraction=14+0.06*T(℃), (5-11)

0.4%Y-doped ceria: fraction=23+0.06*T(℃), (5-12)

(0.6-1.5)%Y-doped ceria: fraction=32+0.06*T(℃), (5-13)

900℃ pumped ceria: same as (5-12),

1000℃-1200℃ pumped ceria: same as (5-13).

The crossover from the low temperature limit to high temperature limit of the B site is found between ~500-700℃, whereas for the A site it is around ~300-400℃. The χ^2 of the least-squares fit of the room temperature spectra usually has larger values. We found we could obtain a better χ^2 by fitting the C site to a Lorentzian-broadened static site.

Fig. 5.16 shows the χ^2 of the least-squares fit for the whole ensemble without broadening. Fig. 5.17 shows the χ^2 of the room temperature spectra with or without broadening (the temperatures labelled for pumped samples are the pumping temperatures). Notice the χ^2 between 500-700℃ in Fig. 5.16 is not good and some of the data points cannot even be fitted. This is because we only used the two extreme limits of the XYZ model and they are not suitable for the crossover temperature range. Fig. 5.18 and Fig. 5.19 show the frequencies of the B site and C sites at elevated temperatures respectively. These frequencies are fitted from all the Y-doped and pumped ceria spectra where B or C sites exist. Both ω_1 and ω_2 of the B site can be fitted to a straight line.

ω_1=63.77-0.01425*T(℃) (Mrad/s), (5-14)

ω_2=110.22-0.01315*T(℃) (Mad/s). (5-15)

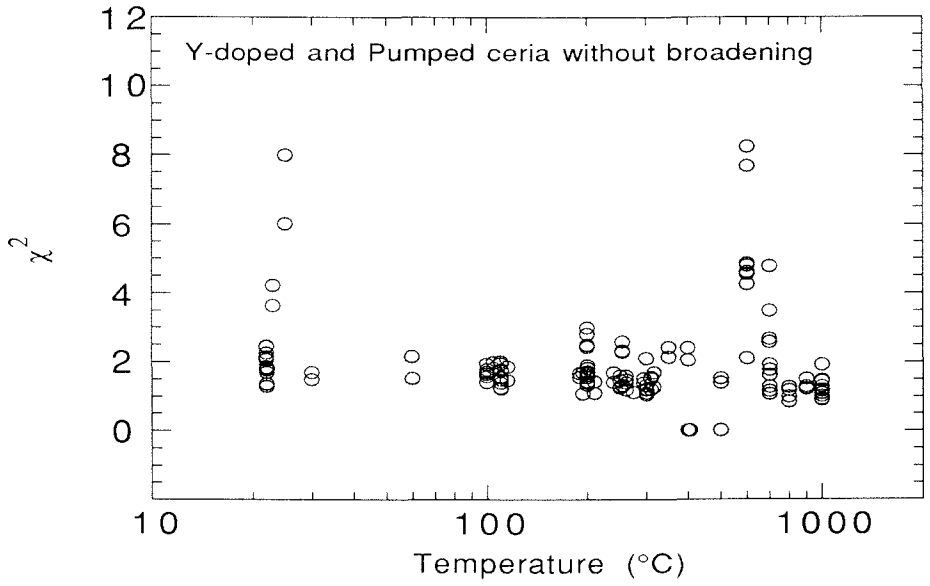

Fig. 5.16 χ^2 of the pumped and Y-doped ceria.

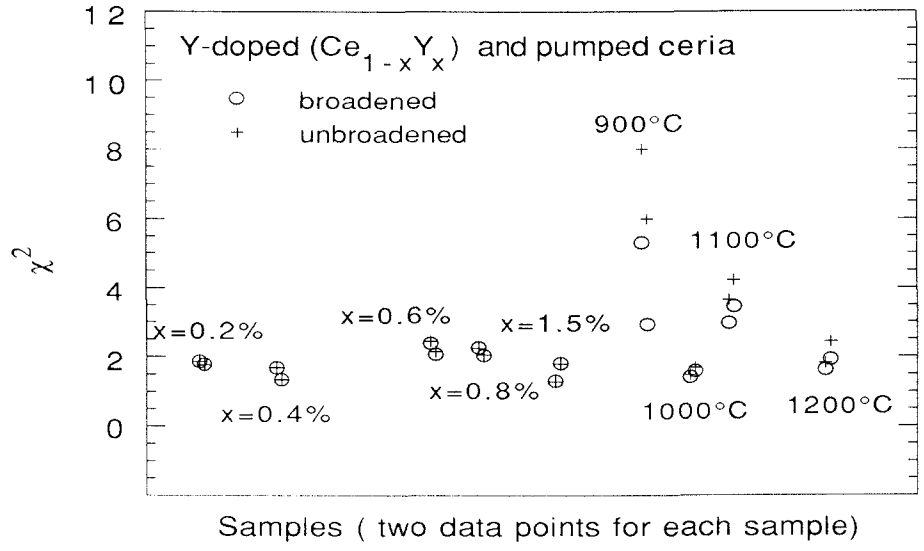

Fig. 5.17 χ^2 of the pumped and Y-doped ceria at room temperature with or without line broadening.

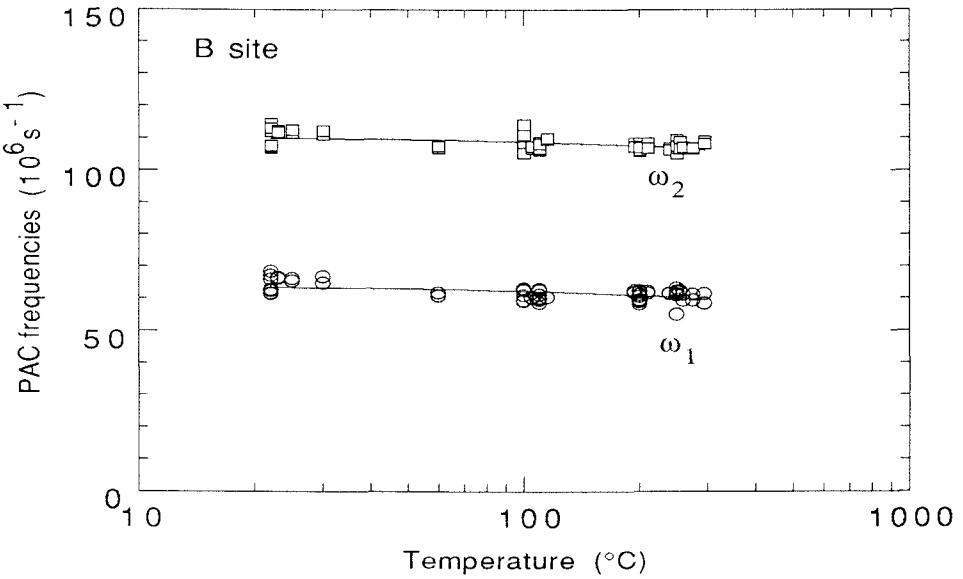

Fig. 5.18 The frequencies of the B site at elevated temperatures.

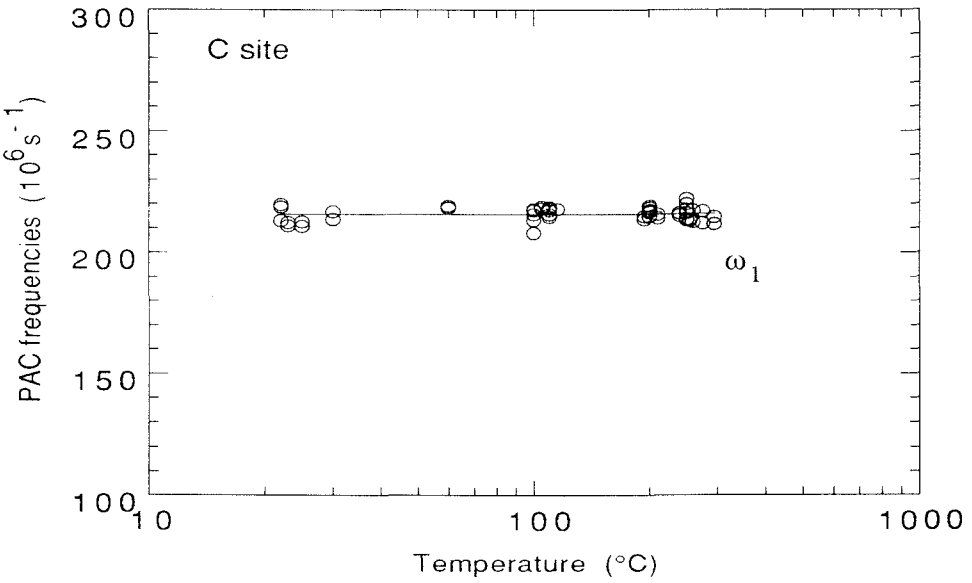

Fig. 5.19 The frequency ω_1 of the C site at elevated temperatures.

From this linear fit, we can derive the asymmetry parameter η for the B site. The result is shown in Fig. 5.20. The C site is axially symmetric with ω_1 being 216(1) Mrad/s and ω_2 being twice of the ω_1. Fig. 5.21 shows the line broadening of the C site at room temperature. Fig. 5.22 and Fig. 5.23 show the A site fraction of pumped and Y-doped ceria respectively. Fig. 5.24 and Fig. 5.25 show the C site fraction of pumped and Y-doped ceria respectively. Fig. 5.26 and Fig. 5.27 show the X site fraction of pumped and Y-doped ceria respectively. Fig. 5.28 show the XYZ damping lambda of the B site.

If we extrapolate the two lines in Fig. 5.20, we can see the frequencies of the B site gradually change to that of the A site. The efg of the B site is not a constant of the temperature, so the XYZ model is not the right one for the B site. We used this model only to get qualitative information about the B site. This also could be one of the reasons for these spectra not fitting well.

For the B site we have also tried to derive the reorientation rate w assuming there are 3, 4, or 6 reorientation directions. The results are given in Fig. 5.29. These data are fitted to an Arrhenius form and the fitted results are,

w=56715*exp(-5.30*1000/T(K)), 3 directions, E=0.46(3) eV, (5-16)

w=20819*exp(-4.55*1000/T(K)), 4 directions, E=0.39(3) eV, (5-17)

w=5397*exp(-3.56*1000/T(K)), 6 directions, E=0.31(3) eV. (5-18)

From Fig. 5.29 we can see that the best fit still comes from the XYZ model.

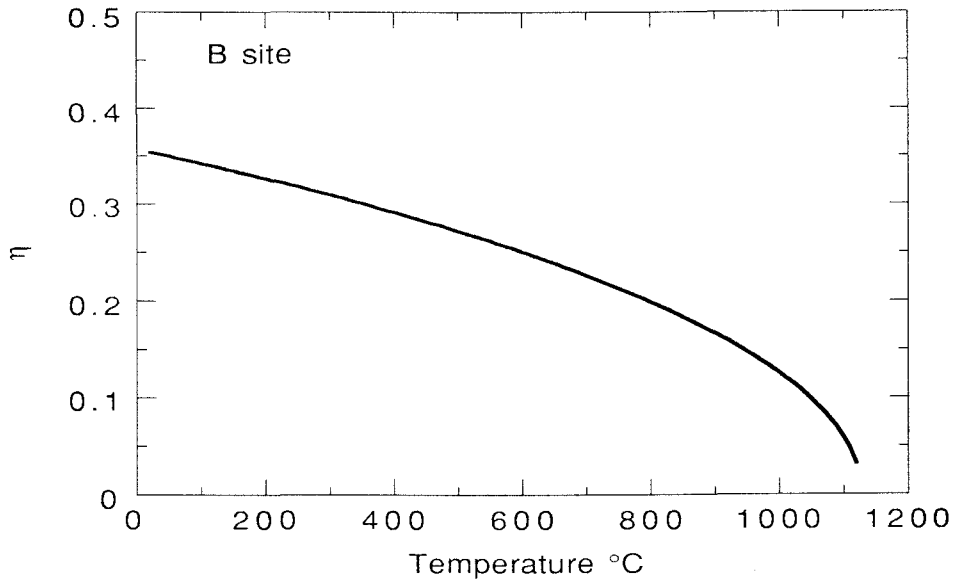

Fig. 5.20 The asymmetry parameter η of the B site.

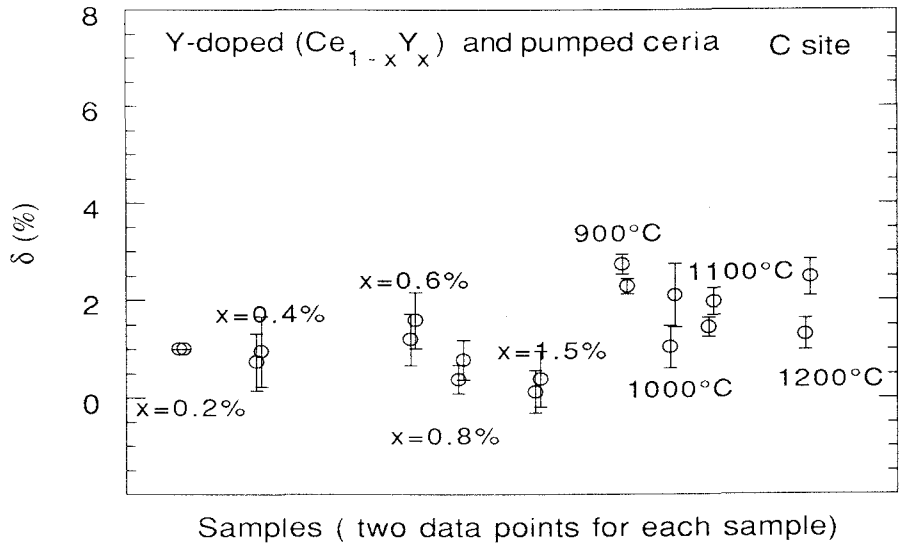

Fig. 5.21 The line broadening of the C site at room temperature.

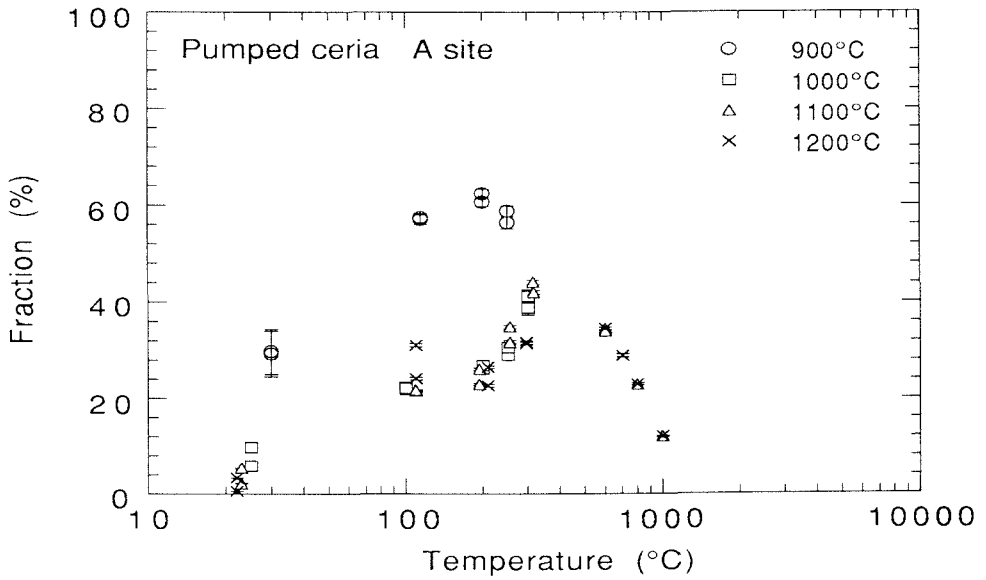

Fig. 5.22 The A site fraction of pumped ceria.

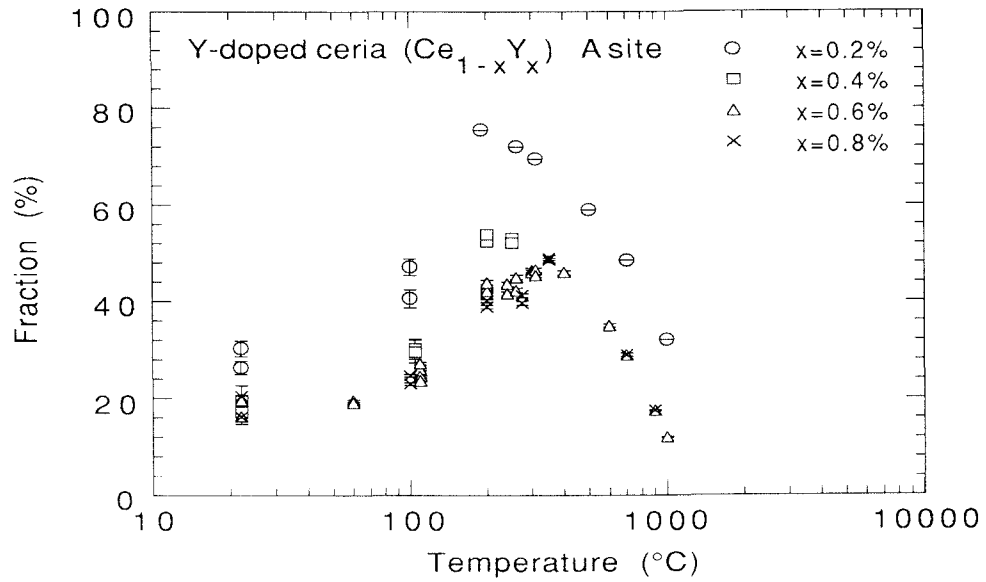

Fig. 5.23 The A site fraction of Y-doped ceria.

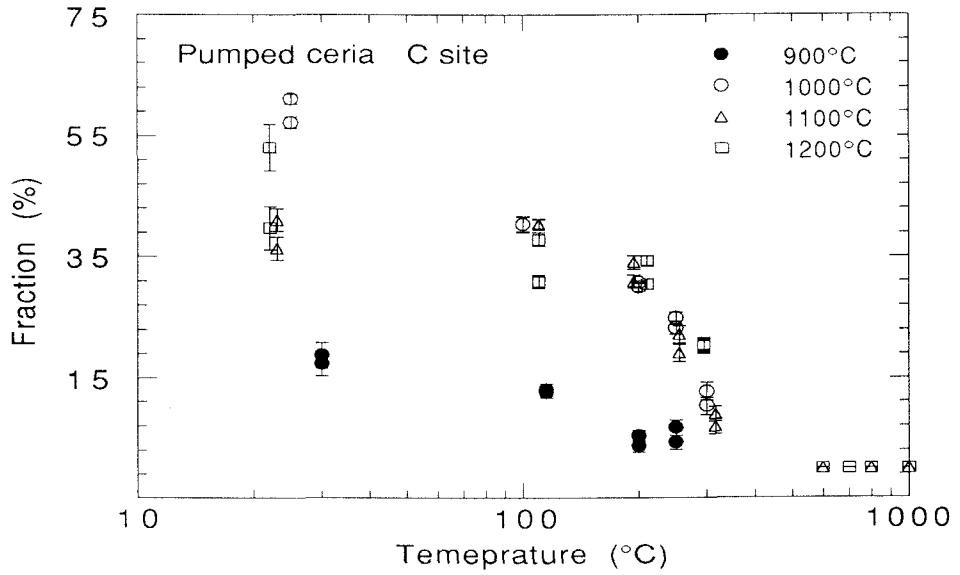

Fig. 5.24 The C site fraction of pumped ceria.

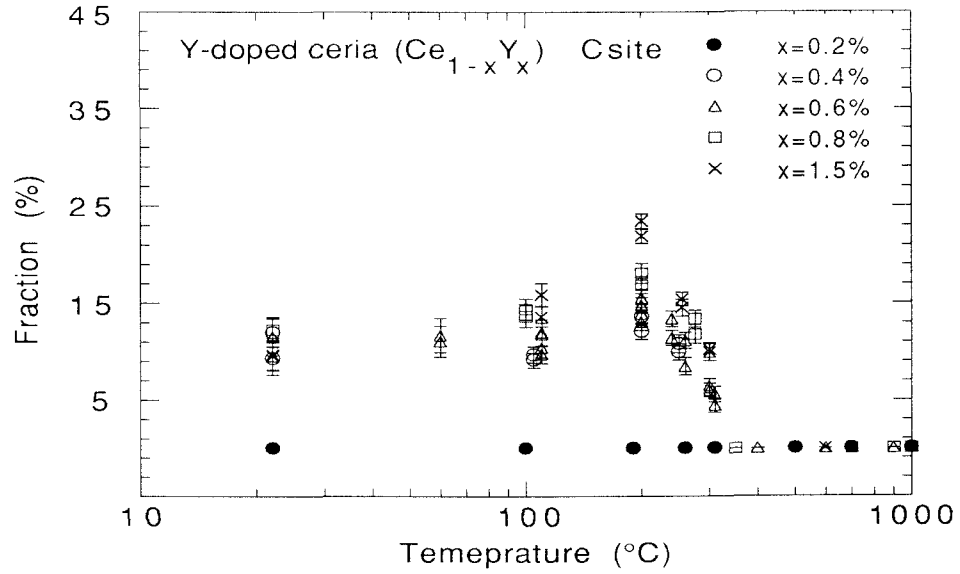

Fig. 5.25 The C site fraction of Y-doped ceria.

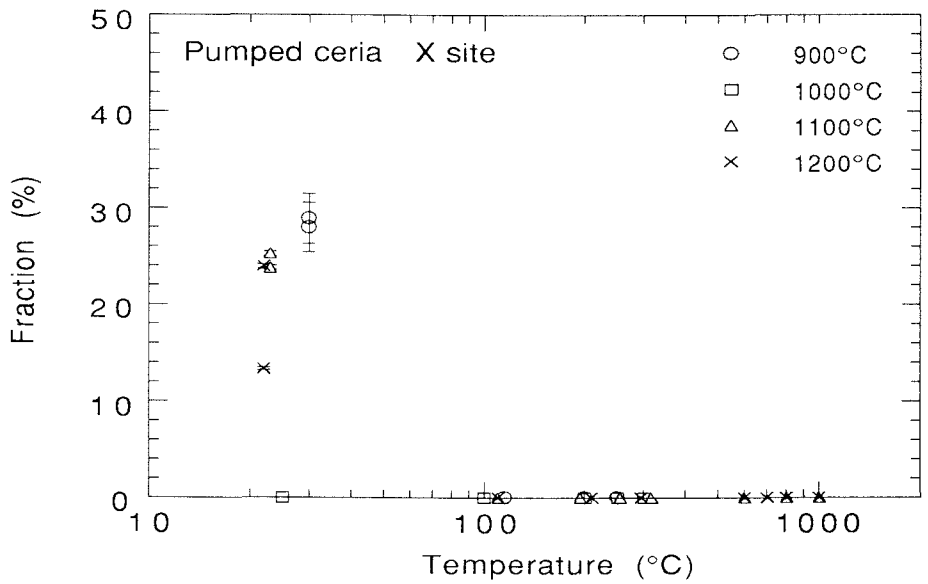

Fig. 5.26 The X site fraction of pumped ceria.

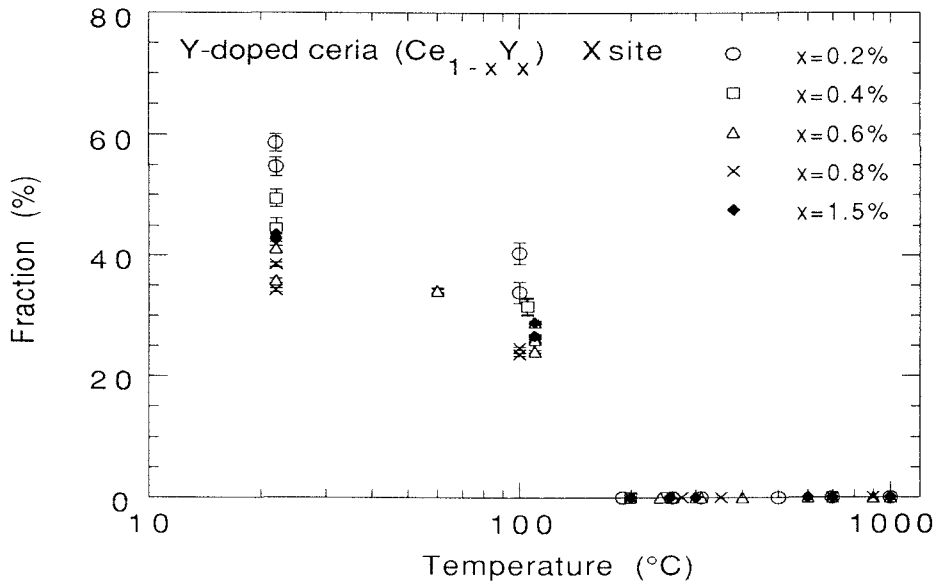

Fig. 5.27 The X site fraction of Y-doped ceria.

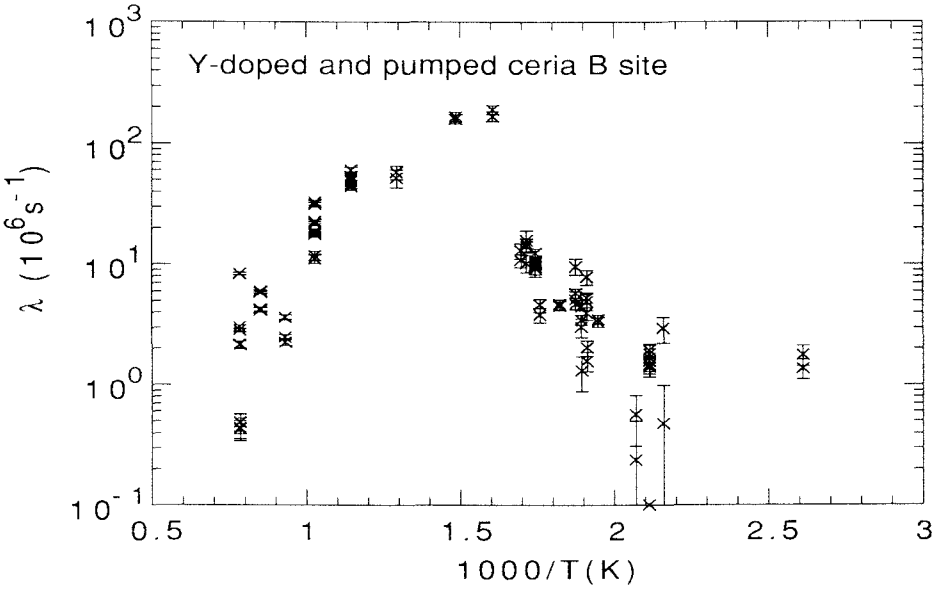

Fig. 5.28 The XYZ damping lambda of the B site

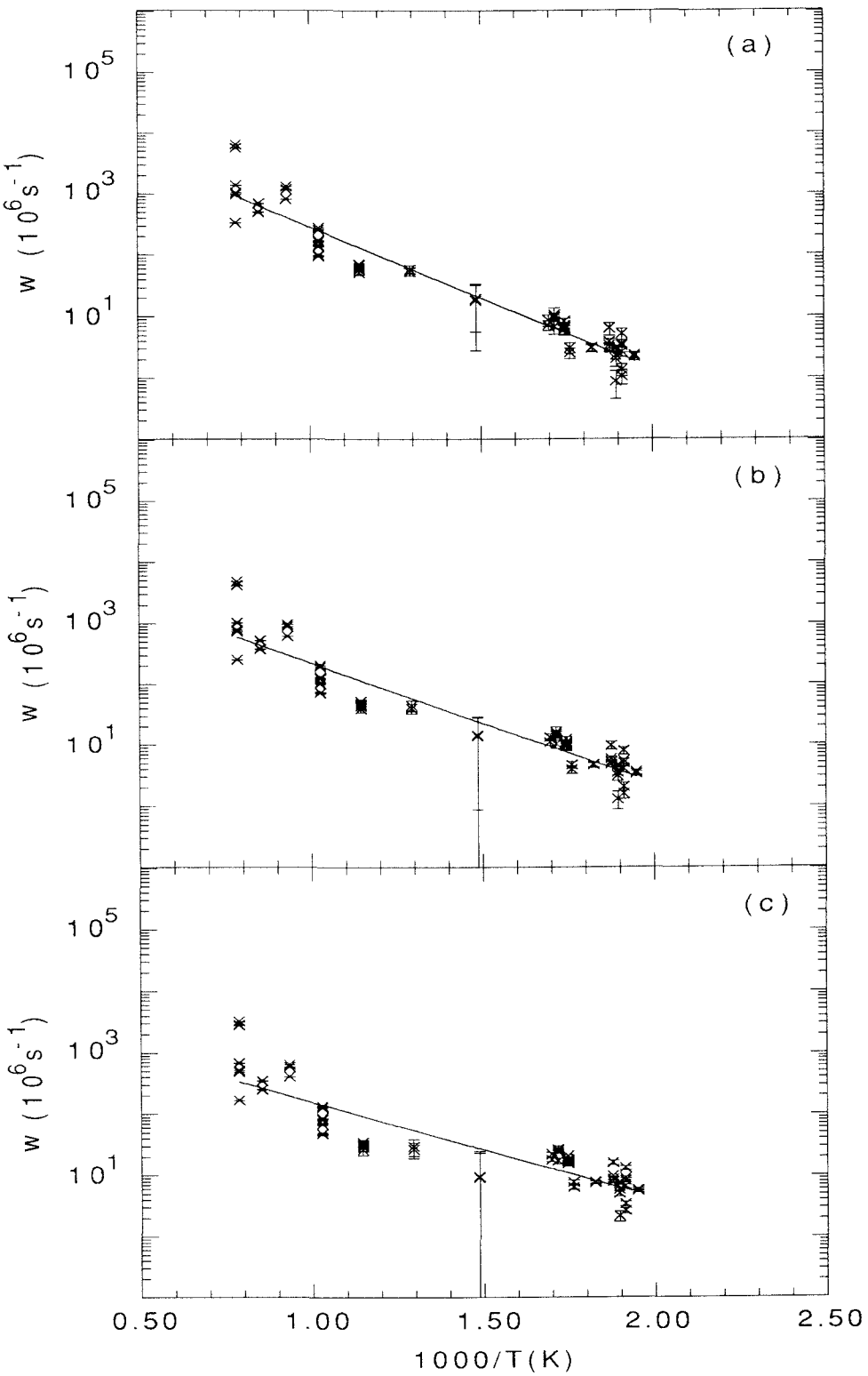

Fig. 5.29 The reorientation rate w of the B site for 3 (a), 4 (b), and 6 (c) reorientation directions

5.3 Nb-doped ceria

We found the D site, the cubic site and the X site in Nb-doped ceria. We include all the Nb-doped ceria (more than 300 ppm Nb doping) in an ensemble of 112 spectra at different doping levels and temperatures.

Fig. 5.30 shows the χ^2 of the fits. Fig. 5.31 shows the D site frequencies at elevated temperatures. In this plot, all the data points whose fraction of the D site is less than 5% or the temperature is higher than 600°C (above this temperature, usually the fraction of the D site is less than 10%) are not used. These frequencies are fitted to linear functions

$$\omega_1 = 179.57 - 0.0635 * T(°C), \quad (5\text{-}19)$$

$$\omega_2 = 267.57 - 0.0912 * T(°C). \quad (5\text{-}20)$$

Fig. 5.32 shows the asymmetry parameter η of the D site. Fig. 5.33, 5.34, and 5.35 show the fractions of the D site, cubic site and X site fraction at elevated temperatures.

We have tried to explain the PAC spectra of Nb-doped ceria by the I-J coupling model (see Appendix A), in which we assume the nuclear spin of probe nucleus couple with the spin of a trapped hole caused by the "aftereffect". But the model we derived is not applicable to the spectra that we observed.

We have also tried to use what we called "on-off" model (see appendix B) to describe both the X site and the cubic site by a single "on-off" site. We used the following function as the "on-off" model:

$$G_2(t) = \frac{r}{r+\lambda_a} + \frac{\lambda_a}{r+\lambda_a} \exp(-(\lambda_a + r)t), \quad (5\text{-}21)$$

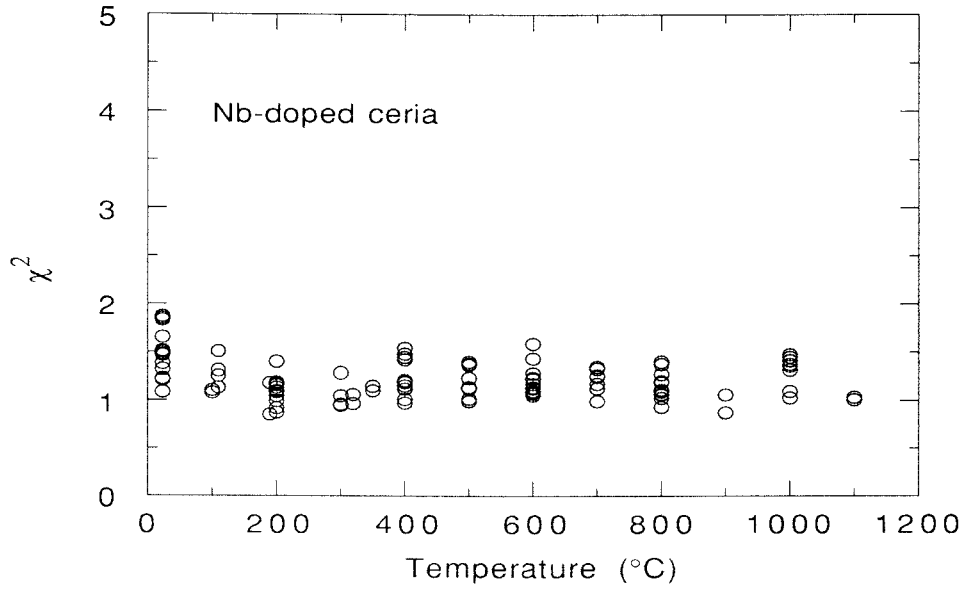

Fig. 5.30 χ^2 of the fits for Nb-doped ceria.

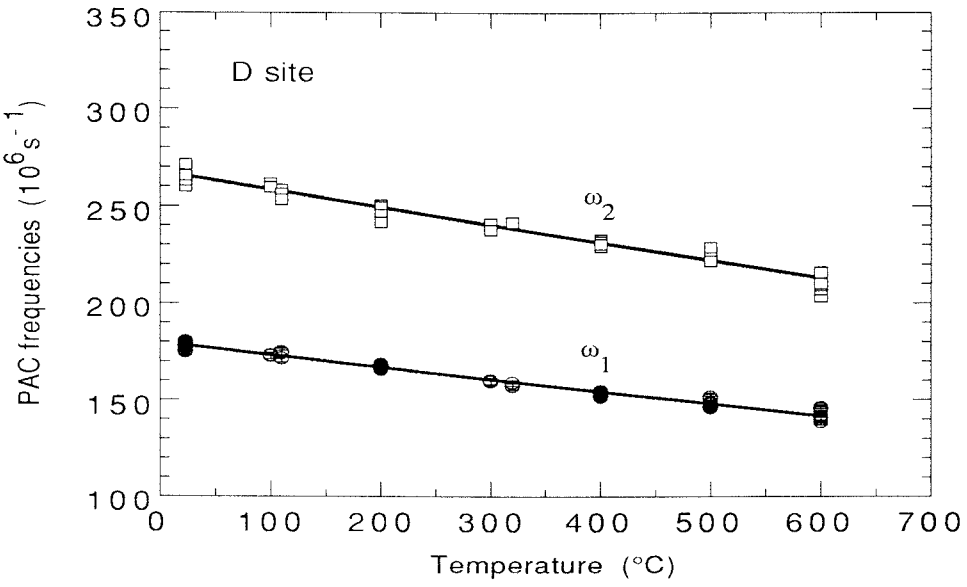

Fig. 5.31 The frequencies of the D site at elevated temperatures.

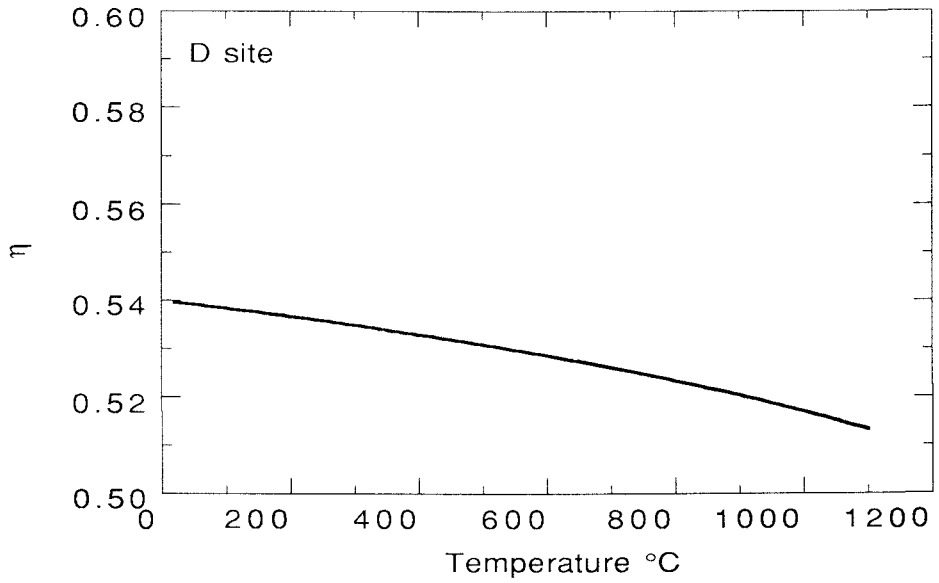

Fig. 5.32 The asymmetry parameter η of the D site.

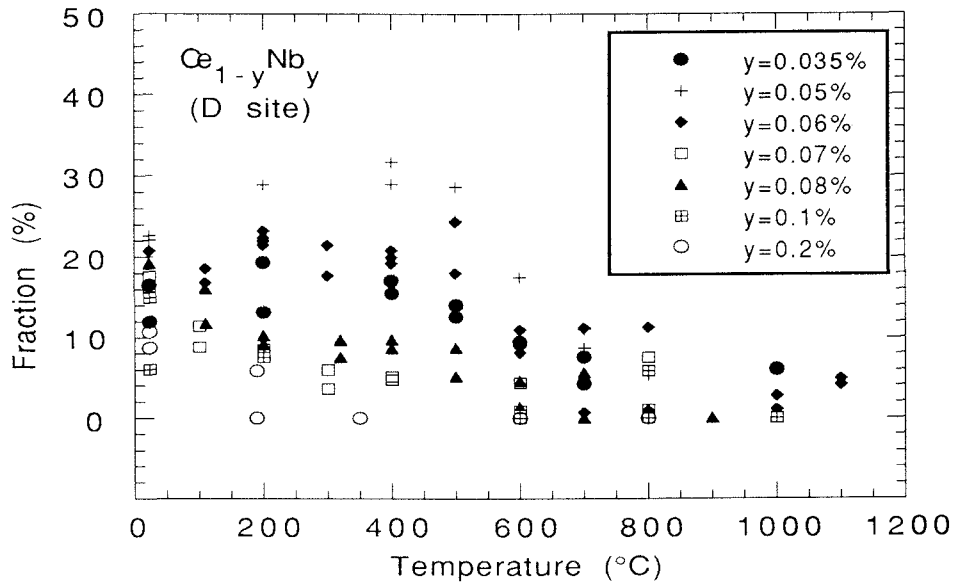

Fig. 5.33 The fraction of the D site at elevated temperatures.

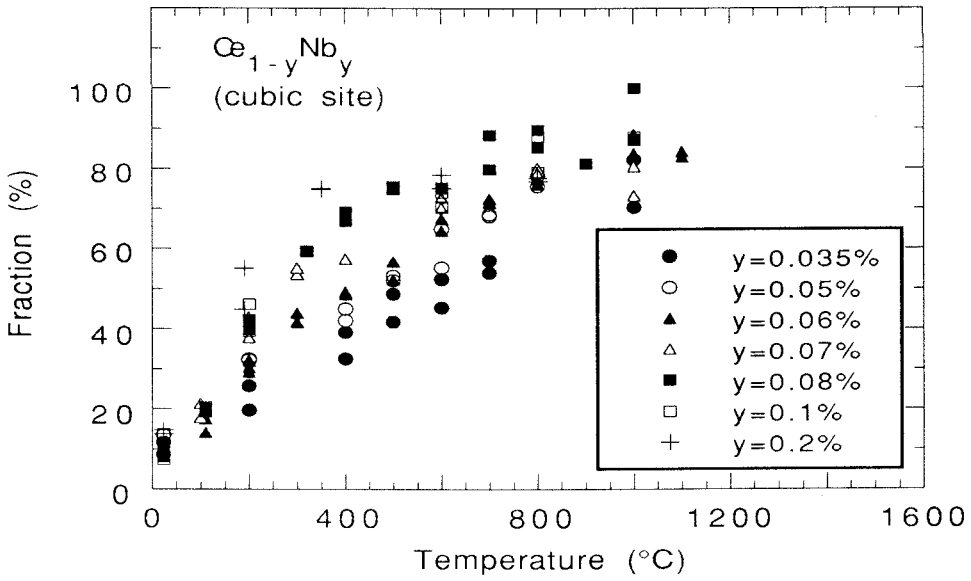

Fig. 5.34 The fraction of the cubic site at elevated temperatures.

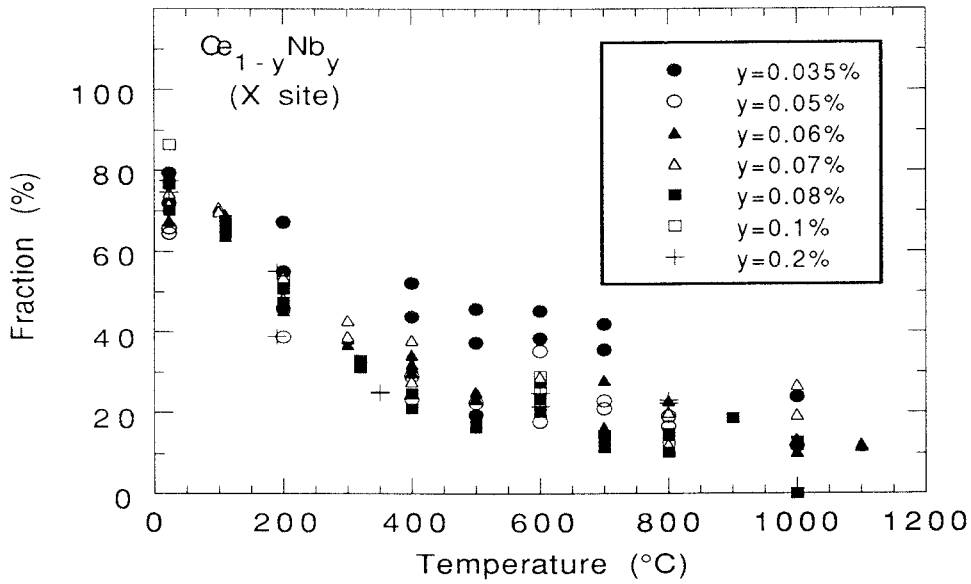

Fig. 5.35 The fraction of the X site at elevated temperatures.

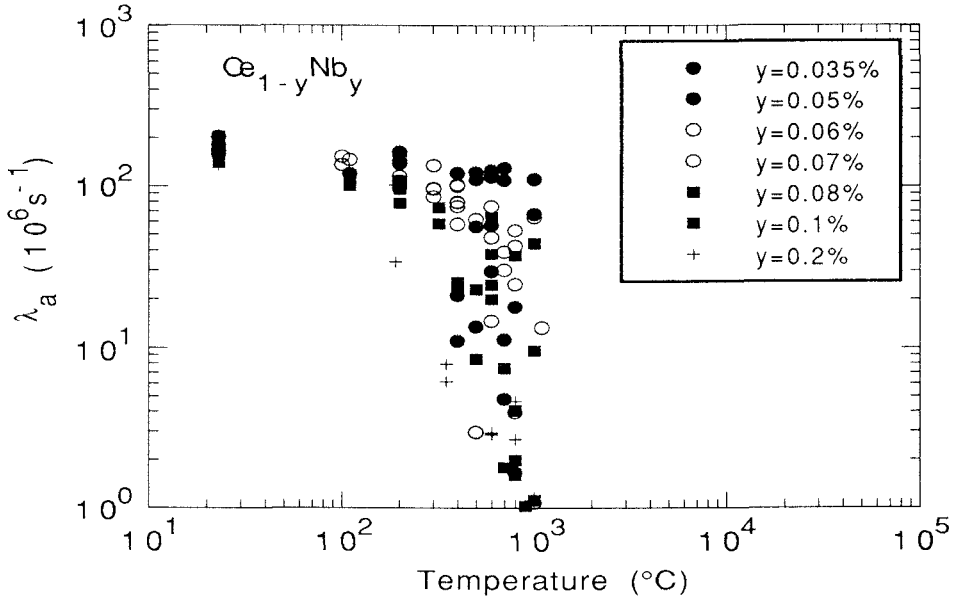

Fig. 5.36 The damping rate λ_a of the "on-off" model for Nb-doped ceria.

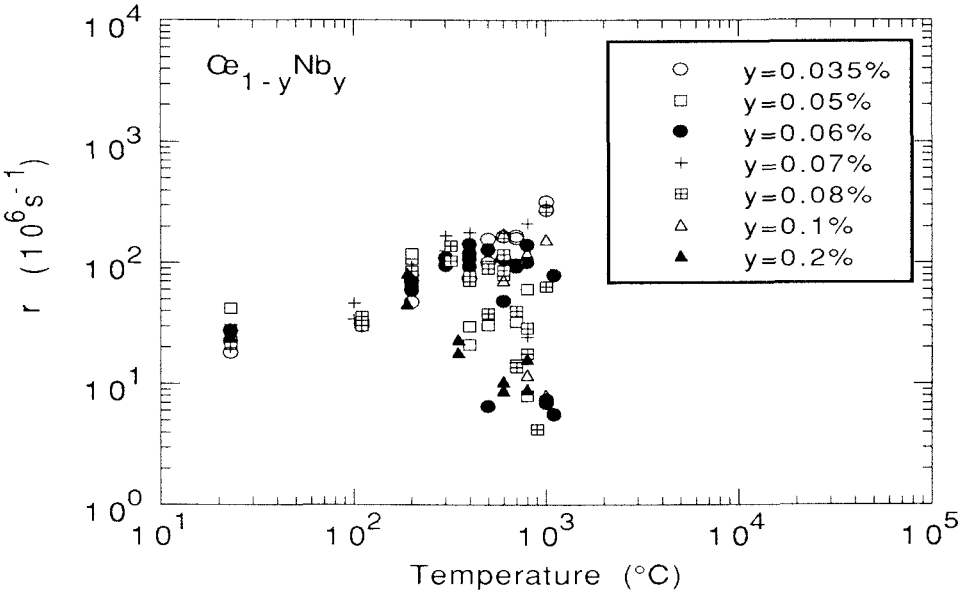

Fig. 5.37 The "off" rate r of the "on-off" model for Nb-doped ceria.

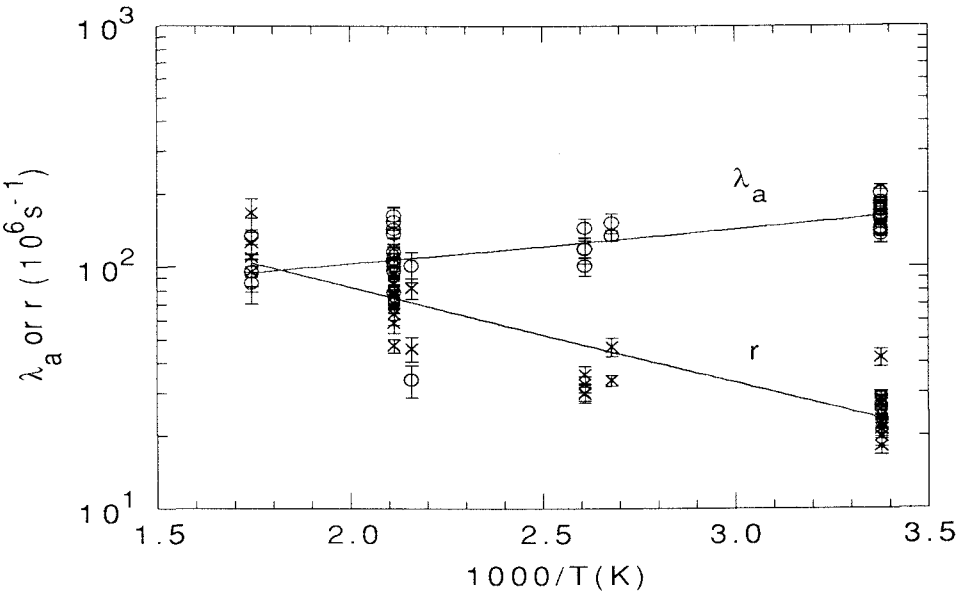

Fig. 5.38 The λ_a and r for Nb-doped ceria at 300°C or below.

where λ_a is the damping rate and the r is the "off" rate. Fig. 5.36 and 5.37 show the λ_a and r at elevated temperatures respectively. This model fits the data reasonable well at 300°C or below where the "off" rate r increases with temperature. If we fit the λ_a and r at 300°C of below to an Arrhenius form, the fitted functions are

$$\lambda_a=53.0*\exp(0.33*1000/T(K)), \qquad (5\text{-}22)$$

$$r=505.3*\exp(-0.91*1000/T(K)). \qquad (5\text{-}23)$$

The temperature dependence of the damping rate λ_a in Fig. 5.38 indicates there is a thermally activated process for the trapped hole. We estimate the activation energy is 0.03 eV from eq. (5-22). This could be the energy barrier for the trapped hole hopping around the nuclear probe in the crystal field. The trapping energy for the trapped hole is estimated as 0.09 eV from eq.(5-23).

6. Summary and conclusions

Perturbed Angular Correlation Spectroscopy studies have been performed on pure and lightly doped cerium oxides. Six different sites, (A, B, C, D, X and cubic), have been found.

In undoped and In-doped ceria we observed the A and X sites. In pumped and Y-doped ceria we observed B and C sites, besides the A and X sites, depending on the doping level and pumping temperature. When we dope ceria with more than 300 ppm Nb, we observed the D, X and cubic sites.

The A and B sites have been fitted by the stochastic XYZ model. This model deals with a case which the symmetry axis of the electric field gradient (efg) fluctuates among three perpendicular (XYZ) directions at rate w. This model assumes a constant axially symmetric efg and every direction of fluctuation is equally probable. The A site is fitted very well by the XYZ model. This is a defect complex of an indium nuclear probe trapped with an oxygen vacancy near by. The trapped oxygen vacancies can be thermally activated and hop among equivalent trap sites. The hopping energy barrier is estimated by the XYZ model as 0.60(2) eV. This defect complex is tightly bound and is not dissociated even up to ~1000°C. PAC measurements show that every indium probe traps an oxygen vacancy. Therefore we predict that indium doping will not increase the ionic conductivity of ceria since it does not introduce free oxygen vacancies. Since one doubly charged oxygen vacancy is produced for every two In dopants or one singly charged oxygen vacancy is produced for every In dopant, the average charge state of the trapped

oxygen vacancy by indium (the A site) is +1. Further experiments are needed in order to identify the charge state of the oxygen vacancies. For example, susceptibility experiments on In-doped ceria will provide information about the charge state of the oxygen vacancies.

The B site is only qualitatively fitted by the XYZ model. The B site appears when oxygen vacancy content is appreciable. The magnitude of the interaction is close to that of the A site and converges toward that of the A site at ~900°C. We speculate this is a complex of the A site with a distant oxygen vacancy. This complex may involve more complicated dynamic processes at high temperatures than what the XYZ model describes. Since we have too little information to justify another model, we used the XYZ model for this site also. The activation energy is estimated by the XYZ model as 0.46(3) eV.

The C and D sites are fitted by the static model. It seems to be a good description of the D site, but it clearly does not provide a truly correct description for the C site. The C site is apparently also a defect complex, like the A and B sites. Because of its small fraction and the temperature range where it exists, the C site can not be fitted to any other model. We use the static model only to simplify the problem while keeping a minimum influence on other parameters. The C site appears when the oxygen vacancy content is large and the C site has axially symmetric efg. We speculate this is a defect complex of the A site plus another oxygen vacancy on the opposite side of the indium atom from the first vacancy. This forms a defect complex of two oxygen vacancies in <111> direction.

The D site is found up to about 700°C. The fraction of the D site

decreases with temperature and Nb doping. We can make this site disappear by pumping at high temperatures and restore this site by flowing oxygen at temperatures above 300°C. This site also disappears when the temperature is reduced to 176K or less. This site can not be caused by a complex of indium with oxygen or Nb interstitials since its fraction decreases with Nb doping. This site can not be due to absorption by the sample of impurities from air, e.g. OH^-, since we could restore this site by flowing only oxygen over the sample above 300°C. Further experiments are needed to identify this site.

Physical considerations suggest that the X site comes from "aftereffects", a perturbation of a electronic hole metastably trapped after the electron capture decay of the ^{111}In parent. The X site in Nb-doped ceria is different from other ceria samples. We can use the "on-off" model to describe the Nb-doped ceria for temperatures at 300°C or below. The "on-off" model describes a perturbation by a hole trapped by the probe nucleus at t=0 ("on"), and then the trapped hole escapes at a constant rate r ("off"). The cubic site in Nb-doped ceria is a simple substitutional site, the "off" site. We speculate the X site in other ceria samples also comes from the "aftereffect" and can also be described by the "on-off" model. But this is a more complicated case than that in Nb-doped ceria because the "off" site is not cubic. We don't have the analytical form of the "on-off" model for this case to do any analysis. Further experiments are needed to prove the X site in the latter case does arise from "aftereffects" interaction. For example, if NMR experiments of In-doped ceria shows only one In site, then we can be sure the X site we saw indeed comes from the "aftereffect" interaction.

A summary of the parameters of the A, B, C, D sites is given in Table 6.1.

Table 6.1 Summary of the A, B, C, and D sites.

Site	ω_1 (10^6/s)	η	V_{zz}(lat)(10^{16}Volts/cm^2)
A	50.0(2)	0	0.87
B	64.1(5)	0.35 (at R.T.)	0.98 (at R.T.)
C	216.0(5)	0	3.76
D	180.0(5)	0.54 (at R.T.)	2.43 (at R.T)

References

1. *Advanced Ceramic Materials: Technological and Economic Assessment*, Noyes Publications, Park Ridge, N. J., U. S. A, 1985.

2. Eugene Ryshkewitch, *Oxide Ceramics*, Academic Press New York and London (1960).

3. *CRC Handbook of Chemistry and Physics*, 68/e, edited by R. C. Weast, CRC press, Boca Raton, (1987).

4 Ralph W. G. Wyckoff, *Crystal Structures*, 2/e, Vol. 1, John Wiley & Sons, Inc., 1963.

5 Y. Maki, M. Matsuda, and T, Kudo, U.S. Pat. 3,607,424 (1971).

6 E. M. Logothetis, Paper presented at the 12th State-of-the-Art Symposium on Ceramics in the Service of Men, Washington, D.C., June 7-9, 1976.

7 D. J. M. Bevan, J. Inorg. and Nucl. Chem., 1955, Vol. 1. pp. 49 to 59. Pergamon Press Ltd. London.

8 G. Brauer and K. A. Gingerich, J. Inorg. and Nucl. Chem., 1960, Vol. 16. pp. 87 to 99. Pergamon Press Ltd. London.

9 D. J. M. Bevan and J. Kordis, J. Inorg. and Nucl. Chem., 1964, Vol. 26, pp. 1509 to 1523. Pergamon Press Ltd. Printed in Northern Ireland.

10 S. P. Ray and A. S. Nowick, J. Solid State Chem. **15**, 344-351 (1975).

11 R. J. Panlener, R. N. Blumenthal and J. E. Garnier, J. Phys. Chem. Solids. 1975, Vol. 36. pp. 1213-1222. Pergamon Press. Printed in Great Britain.

12 O. Toft Sørensen, J. Solid State Chem. **18**, 217-233 (1976).

13 Peter Knappe and Leroy Eyring, J. Solid State Chem. **58**, 312-324 (1985).

14 J. von Rudolph, Z. Naturforsch. Teil A, **14**, 727 (1959).

15 E. M. Greener, J. M. Wimmer, and W. M. Hirthe, in Proceedings of the Conference of Rare Earths, Fourth Conference, Phoenix, Arizona, 1964, p. 538.

16 R. N. Blumenthal and J. E. Laubach, in *Anisotropy in Single-Crystal Refractory Compounds*, M. S. Seltzer and S. A. Mersol, Editors, p. 138, Plenum Press, New York (1968).

17 R. N. Blumenthal, P. W. Lee, and R. J. Panlener, J. Electochem. Soc., **118**, 123 (1971).

18 R. N. Blumenthal and J. E. Garnier, J. Solid State Chem. **16**, 21-34 (1976).

19 Edward K. Chang and R. N. Blumenthal, J. Solid State Chem. **72**, 330-337 (1988).

20 Julius R. Sims, Jr., and R. N. Blumenthal, High Temperature Science **8**, 121-128 (1976).

21 H. L. Tuller and A. S. Nowick, J. Phys. Chem. Solids. 1977, Vol. 38, pp. 859-867. Pergamon Press. Printed in Great Britain.

22 R. Gerhardt-Anderson and A. S. Nowick, *Transport in Nonstoichiometric Compounds*, ed. G. Simkovich, Plenum Press 1985.

23 B. C. H. Steele and J. M. Floyd, Proc. Br. Ceram. Soc., **19**, 55 (1971).

24 Y. Ban and A. S. Nowick, National Bureau of Standards Special Publications 364, Solid State Chemistry, Proceedings of 5th Material Research Symposium, July 1972, pp. 353.

25 E. Recknagel, G. Schatz, and Th. Wichert, in *Hyperfine Interactions of Radioactive Nuclei*, edited by J. Christiansen, Springer-Verlag, Berlin (1983), pp. 133-204.

26 G. S. Collins and R. B. Schuhmann, Phys. Rev. B **34**, 502 (1986).

27 H. Metzner, R. Sielemann, S. Klaumünzer, and E. Hunger, Phys. Rev. B **36**, 9535 (1987).

28 F. Raether, D. Wiarda, K. P. Lieb, J. Chevallier, and G. Weyer, Z. Phys. B **73**, 467 (1989).

29 W. Bolse, M. Uhrmacher, and K. P. Lieb, Phys. Rev. B **36**, 1818 (1987).

30 A. F. Pasquevich and R. Vianden, Phys. Rev. B 37, 10858 (1988).

31 K. Krusch and J. A. Gardner, phys. Rev. B **24**, 4587 (1981).

32 M. Brüssler, H. Metzner, K. D. Husemann, and H. J. Lewerenz, Phys. Rev. B **38**, 9268 (1988).

33 H. Jaeger, J. A. Gardner, J. C. Hayarth, and R. L. Rasera, J. Am. Ceram. Soc. **69** 458 (1986).

34 H. T. Su, R. P. Wang, H. Fuchs, J. A. Gardner, W. E. Evenson, and J. A. Sommers, J. Am. Ceram. Soc. **73** 3215 (1990).

35 B. Harmatz, Nuclear Data Sheets **27**, 453 (1979).

36 P. Herzog, K. Freitag, M. Reuschanbach, and H. Walitzki, Z. Phys, A **294**, 13 (1980).

37 H. Frauenfelder and R. M. Steffen, in *Alpha-beta-and Gamma-Ray Spectroscopy*, Vol. 2, edited by K. Siegbahn, North-Holland, Amsterdam (1965), Chap. XIXA, pp997-1198.

38 U. Bäverstam, R. Othaz, H. de Sousa, and B. Ringström, Nucl. Phys. A 186, 500 (1972).

39 A. G. Bibiloni, C. P. Massolo, J. Desimoni, L. A. Mendaza-Zélis, F. H. Sánchez, A. F. Pasquevich, L. Damonte, and A. R. López-Garcia, Phys. Rev. B **32**, 2393 (1985).

40 *Table of Isotopes*, 7/e, edited by C. M. Lederer and V. S. Shirley, Wiley-Interscience, New York (1978), pp. 521.

41 E. Matthias, W. Schneider and R. M. Steffen, Phys. Lett. 4 (1963) 141.

42 P. da R. Andrade and J. D. Rogers, Phys. Rev. B **3**, 1052 (1971).

43 A. Baudry and P. Boyer, Hyperfine Interactions **35**, 803 (1987).

44 A. Abragam and R. V. Pound, Phys. Rev. **92**, 943 (1953).

45 M. Blume, Phys. Rev. **174**, 351 (1968).

46 H. Winkler and E. Gerdau, Z. Physik **262**, 363 (1973).

47 H. Gabriel, J. Bosse, *Angular correlations in nuclear disintegration*, ed. by H. van Krugten, B. van Nooijen, pp. 394. Groningen, Rotterdam University Press 1971.

48 W. E. Evenson, J. A. Gardner, R. P. Wang, H. T. Su, and A. G. McKale, submitted to Hyperfine Interactions, July, 1990.

49 H. Jaeger, J. A. Gardner, H. T. Su and R. L. Rasera, Rev. Sci. Instrum. **58**, 1694 (1987).

50 H. Jaeger, J. A. Gardner, J. C. Haygarth, and R. L. Resera, J. Am. Ceram. Soc. **69**, 458 (1986).

51 A. Baudry, P. Boyer, and P. Vulliet, Hyperfine Interactions **13**, 263 (1983).

52 *Harshaw radiation detectors*, Harshaw/Filtrol Partnership, Solon (1984).

53 A. R. Arends, C. Hohennemser, F. Pleiter, H. De Waard, L. Chow, and R. M. Sutter, Hyperfine Interractions **8**, 191 (1980).

54 P. R. Bevington, *Data Reduction and Error Analysis for the Physical Sciences*, McGraw-Hill, New York, (1969).

55 H. Haas and D. A. Shirly, J. Chem. Phys. **58**, 3339 (1972).

56 F. K. Feiock and W. R. Johnson, Phys. Rev. **187**, 39 (1969).

57 P.C. Lopiparo and R. L. Rasera, in Angular Correlations in Muclear Disintegration, edited by H. V. Drugten and B. Van Nooijen, Rotterdam University Press, Rotterdam (1971).

58 Manuel Rotenberg, R. Bivins, N. Metropolis, and John K. Wooten, Jr., The 3-j and 6-J Symbols, The Technology Press, MIT, Cambridge, Massachusetts, 1959.

59 P. W. Martin, S. R. Dong, and J. G. Hooley, Chem. Phys. Lett. **105**, 343 (1984).

APPENDICES

A. Perturbation function for the I-J coupling interaction

In chapter 2, we give the theory for the perturbed angular correlation function.(eq. 2-18) and the perturbation factor eq. (2-19). We also discussed the case where we only have a static electric quadrupole interaction for a I=5/2 polycrystalline sample eq. (2-25). Here we will discuss the case where the interaction is caused only by the coupling of the nuclear spin I of probe nucleus to the angular momentum J of the electronic states of an atom or molecule.

The interaction Hamiltonian K for the I-J coupling interaction is[37]:

$$K_{IJ} = \alpha \mathbf{I} \bullet \mathbf{J} \qquad \text{(A-1)}$$

The eigenstates $|Ff>$ of K can be expressed by

$$|Ff> = \sum_{Mm} |JM>|Im><ImJM|Ff> \qquad \text{(A-2)}$$

where $\mathbf{F}=\mathbf{I}+\mathbf{J}$ is the total angular momentum of the system and m, M and f are the projection quantum numbers.

In the absence of an externally applied magnetic field the eigenvalues of K depend only on F

$$K|Ff> = E_F|Ff>, \qquad \text{(A-3)}$$

and the eigenvalues are given by

$$E_F = \frac{1}{2}\alpha[F(F+1) - I(I+1) - J(J+1)] \qquad \text{(A-4)}$$

The matrix of the evolution operator $\Lambda(t)$ is diagonal in the $|Ff>$ representation, and the matrix elements are given by

$$<Ff|\Lambda(t)|Ff> = \exp(-\frac{i}{\hbar}E_F t) \qquad \text{(A-5)}$$

We change the above equation to the m-representation by using the inverse of eq. (A-2):

$$< m_b|\Lambda(t)|m_a >= \sum_{Ff} < Im_b\, JM|Ff >< Im_a\, JM|Ff > \exp(-\frac{i}{\hbar}E_F t) \quad . \qquad (A\text{-}6)$$

This expression is now inserted into eq. (2-19) for the perturbation factor:

$$G_{k_1k_2}^{N_1N_2}(t) = \sum_{\substack{m_a m_b \\ Ff,F'f'}} (-1)^{2I+m_a+m_b}[(2k_1+1)(2k_2+1)]^{\frac{1}{2}}(2F+1)(2F'+1)\exp[-\frac{i}{\hbar}(E_F-E_{F'})t]$$

$$\times \begin{pmatrix} I & I & k_1 \\ m_{a'} & -m_a & N_1 \end{pmatrix}\begin{pmatrix} I & I & k_2 \\ m_{b'} & -m_b & N_2 \end{pmatrix}\begin{pmatrix} I & J & F \\ m_a & M & -f \end{pmatrix}\begin{pmatrix} I & J & F \\ m_b & M' & -f \end{pmatrix}\begin{pmatrix} I & J & F' \\ m_{b'} & M'' & -f' \end{pmatrix}\begin{pmatrix} I & J & F' \\ m_{a'} & M''' & -f' \end{pmatrix} . \qquad (A\text{-}7)$$

We perform the summation over m_a and m_b by using Racah algebra and obtain:

$$G_{kk}(t) = \frac{1}{2J+1}\sum_{F,F'}(2F+1)(2F'+1)\begin{Bmatrix} F & F' & k \\ I & I & J \end{Bmatrix}^2 \exp[-\frac{i}{\hbar}(E_F - E_{F'})t] \quad . \qquad (A\text{-}8)$$

For I=5/2 and J=1/2, F=2 or 3, $E_2=-\frac{7}{4}\alpha$ and $E_3=\frac{5}{4}\alpha$. For the case of k=2,

$$G_{22}(t) = \frac{1}{2}\{25\begin{Bmatrix} 2 & 2 & 2 \\ \frac{5}{2} & \frac{5}{2} & \frac{1}{2} \end{Bmatrix}^2 + 49\begin{Bmatrix} 3 & 3 & 2 \\ \frac{5}{2} & \frac{5}{2} & \frac{1}{2} \end{Bmatrix}^2 + 2\times 5\times 7\begin{Bmatrix} 2 & 3 & 2 \\ \frac{5}{2} & \frac{5}{2} & \frac{1}{2} \end{Bmatrix}^2 \cos[\frac{1}{\hbar}(E_2 - E_3)t]\} \quad , \qquad (A\text{-}9)$$

$$G_{22}(t) = \frac{1}{2}[25\times\frac{2}{75} + 49\times\frac{1}{49} + 70\times\frac{1}{210}\cos(3\alpha t/\hbar)] \quad . \qquad (A\text{-}10)$$

The 6-j coefficients are found in reference 58.

B. The on-off model

We have mentioned briefly in **1.3** that aftereffects is one of the challenging aspects of perturbed angular correlation spectroscopy. Many researchers have tried to model these effects[38, 39,44,59].

The so-called aftereffects are the electronic relaxation processes which follow the creation of an electron hole in the inner atomic shell after the radioactive decay of the parent nucleus, ^{111}In in this case. This inner shell hole is filled by electronic transitions from outer shells. The Auger processes take place during the transitions. This hole causing another hole in the outermost atomic shells. These electron rearrangements may affect the angular correlation. Because the mean life-time of the hole in the outermost atomic shell depends strongly on the atomic environment, the attenuation of the angular correlation will vary with the character of the probe surroundings. In insulating material, like ceria, this hole may remain trapped long enough to affect PAC spectra.

The on-off model assumes the perturbation factor is $G_{2af}(t)$ while this metastable electronic configuration persists, i.e. "on". The aftereffects are turned "off" when the metastably trapped hole escapes, assuming it turned off at rate r. Then the probability of the "on" is exp(-rt) and that of the "off" at time t in dt time is r*exp(-rt)*dt. For the simple case for which the "off" environment does not produce any electric field gradient (efg) at the nuclear probe site, i.e. $G_2(t)=1$, we can derive the perturbation factor of the on-off model as follows

$$G_2(t)=G_{2af}(t)*\exp(-rt)+\int_0^t dt'\, r*\exp(-rt')*G_{2af}(t). \qquad \text{(C-1)}$$

If we assume $G_{2af}(t)=\exp(-\lambda_a t)$, then the perturbation function becomes

$$G_2(t)=\exp(-\lambda_a t)*\exp(-rt)+\int_0^t dt'\ r*\exp(-rt')*\exp(-\lambda_a t')$$

$$=\{r+\lambda_a*\exp[-(\lambda_a+r)t]\}/(r+\lambda_a). \qquad \text{(C-2)}$$

When the "off" environment has a non-zero efg at the probe nucleus, the perturbation factor is more complicated.